UC Berkeley
UC Berkeley Electronic Theses and Dissertations

Title

Atomic-Scale Cryogenic Electron Microscopy Imaging of Synthetic Polymers

Permalink

https://escholarship.org/uc/item/8nj3r6tt

Author

Seidler, Morgan

Publication Date

2024

Peer reviewed|Thesis/dissertation

Atomic-scale Cryogenic Electron Microscopy Imaging of Synthetic Polymers

By

Morgan Elizabeth Seidler

A dissertation submitted in partial satisfaction of the

requirements for the degree of

Doctor of Philosophy

in

Chemical Engineering

in the

Graduate Division

of the

University of California, Berkeley

Committee in charge:

Professor Nitash Balsara, Chair
Professor Rui Wang
Professor Mary Scott

Summer 2024

Atomic-scale Cryogenic Electron Microscopy Imaging of Synthetic Polymers

Abstract

Atomic-scale Cryogenic Electron Microscopy Imaging of Synthetic Polymers

by

Morgan Elizabeth Seidler

Doctor of Philosophy in Chemical Engineering

University of California, Berkeley

Professor Nitash Balsara, Chair

Materials engineering depends on a thorough understanding of the structure-property relationships in order to rationally design better materials. In polymer science, information about the structure of the material generally comes from scattering techniques, such as wide angle X-ray scattering or neutron scattering. These scattering experiments produce information about the material's structure in reciprocal space, so there can at times be ambiguity in the results when transitioning to real space. Transmission electron microscopy (TEM) is widely used in the materials science community to produce direct, atomic-scale images of hard materials. However, special techniques are needed to image polymeric materials with TEM due to the inherent radiation sensitivity in these soft materials. A series of techniques termed cryo-EM have been developed by the structural biology community to produce atomic-resolution images of proteins. Cryo-EM has only sparingly been applied to synthetic polymers, yet it is a promising tool to advance polymer science.

This dissertation focuses on the application of cryo-EM techniques to study the atomic structure of synthetic polymers. The atomic-scale images of the polymers are combined with other material characterization data, molecular dynamics simulations, and TEM image simulations in order to understand the governing interactions that control self-assembly at the atomic level. The direct, atomic-scale imaging of synthetic polymer materials serves to advance material engineering by uncovering the structure-property relationships starting at the atomic scale.

Chapters 2, 3, and 4 provide detailed studies in using polypeptoids, which are synthetic polymers with a monomer unit similar to peptides, to uncover the effect of single atom substitutions, ionic interactions, and fixed charges on the self-assembly of these materials. Polypeptoids are a great model system to study self-assembly because their unique submonomer synthesis method grants the ability to precisely vary single atoms within the polymer structure. Chapter 2 starts with using this ability to study the effect of halogen substitutions on the self-assembly and crystal motifs of polypeptoid nanosheets. Chapter 3

investigates the effect of fixed charges and condensed counterions in polypeptoid nanofibers. Chapter 4 details an investigation into the effect of fixed charges and charge density on polypeptoid self-assembly.

Chapter 5 applies the same cryo-EM techniques to a conventional diblock copolymer in poly(ethylene oxide)-b-polystyrene (SEO). New synthetic routes were established to create single crystals of SEO with a lithium salt whereby the lithium salt was fully incorporated in the crystal. The single crystals of SEO were imaged with atomic-scale resolution to study how the arrangement of polymer chains changes in response to different amounts of lithium salt. Image simulation based on known crystal structures was used to bring greater understanding to the atomic-scale images.

If I am occasionally a little over-dressed, I make up for it by being always immensely
over-educated.
- Oscar Wilde, The Importance of Being Earnest

Contents

List of Figures

List of Tables

Acknowledgments

I was blessed to have two brilliant advisors to guide me through my PhD: Dr. Xi Jiang and Dr. Nitash Balsara. In my first years of graduate school, Xi spend hundreds of hours training me on the instrumentation and lab procedures and single-handedly taught me the entire workflow of cryo-EM. His infinite patience and kindness as I stumbled through my early time as a graduate student will forever stay with me. Once I became more independent in lab, I was grateful to have him as my closest collaborator, brainstorming partner, and emotional support when my experiments weren't working. Xi set the standard for me in how to be a good mentor, and I can only hope to emulate his style as I become a mentor in my future career.

Throughout my five years of graduate school, Nitash guided me with a steady hand as I grew from a young, inexperienced student into an independent, confident scientist and researcher. Throughout our individual meetings, lengthy paper writing sessions, and group bonding activities, Nitash remained steady in cultivating both my love for science and my development as a leader. Nitash has established a wonderful group culture built on open collaboration, excellent science, and lifting each other up. I am proud to have been a Nitash student and contribute to the legacy of the Balsara lab.

The other members of the Balsara lab have been fundamental to making my time in the lab an enjoyable experience. In particular, the postdocs have a special role in guiding the lab. I am eternally grateful to Saheli for her gentle guidance, scientific expertise, and emotional support as I have navigated the trials of graduate school and life. Saheli is an excellent scientist, friend, and mentor and I am endlessly thankful that I was able to spend four years learning from her. I only hope I can be like her when I grow up. David truly leads by example and always volunteers his time to lift others up. He has an absolute wealth of scientific knowledge and his adventurous and kind spirit has been inspiring throughout my time in graduate school. Louise's enthusiasm for science, happy hour, and friendship has made her an essential part of the group culture and her presence is deeply missed. Jaeyong has the strongest work ethic for science and social time of anyone I have met and has been an integral part of promoting a great lab culture. I am grateful for all of the lunchtime chats I have had with Rounak - it is always great to have a friend to chat with and pick me up when the day is not going as I planned. Thank you for being a steady, joyful presence in Tan Hall. Keisuke is a great member of our lab and softball team - good thing Nitash finally considered baseball skills in his recruitment! Xiaopeng worked so hard during his time in our lab and made incredible scientific advancements. Youngwoo brought in amazing collaborations and is a great model of team work in science. Tianyi and Yen were an absolutely vital part of my graduate school experience and I truly could not have done any of the work in this dissertation without their synthesis expertise. Thank you for being such kind and enthusiastic collaborators throughout my PhD.

Whitney, Jackie, and Deep were so kind when I first joined the Balsara lab. I instantly felt welcomed at group social events and they truly made an effort to get to know me even though we had a short time together. Mike and Gumi accepted me into the lab and worked

hard to maintain an uplifting lab culture even though most of our interactions were virtual. They are always willing to help me out even long after they graduated.

Lorena has truly been my role model throughout graduate school. She is an excellent example of how to work hard, have fun, and lift others up. She taught me both how to stand up for myself and how to always advocate for positive change. Lorena had such a strong presence in our lab and her contributions to improving our group culture have stayed around for much longer than her time at Berkeley. Kevin always worked hard and maintained lab equipment to allow others to flourish.

It was such a pleasure to be lab mates, coworkers, and friends with Zach, Alec, and Neel. Zach - you were always such a positive, uplifting, and fun presence throughout graduate school. Your tenacity to take on new projects is admirable and I am so grateful for your leadership in organizing lab social outings. Alec - thank you for being my skiing companion and introducing me to Japanese whiskey. Your scientific achievements will guide the lab for years to come and I am so grateful for our continued friendship. Neel - I am so thankful that we were able to overlap for four years in the lab. Your resilience and strength is so admirable and your guidance during graduate school was invaluable to me.

To my cohort of 2019 - thank you for being the best classmates and friends to go through the PhD journey with me. I am especially grateful for my cohort member and lab mate Darby for being such a steadfast leader in our lab and so willing to give her time to help others. From taking such good care of our lab as the safety coordinator to always RSVP'ing yes to my social plans, I am so thankful to have done graduate school with you. I want to thank the fellow members of Loud House for continuing our annual cohort bonding trips, taking me on my first tent camping trips ever, and always being there during the numerous trials of graduate school.

Vivaan is an incredible scientist and has managed to become an expert in every experimental technique that our lab does. He is also an amazing friend, an aspiring graphic designer who gives the best feedback ever on PowerPoint slide design, and my fellow secret Swiftie. I am so excited to see everything you continue to accomplish. Karim brings a great light-hearted energy to our lab and to life. He is the biggest supporter of our PBR softball team that I have ever seen and has an incredible music taste.

The lab is being left in good hands with Emily, Michael, and Lily. Emily is perhaps the most capable person I have ever met. She continues to take on the most difficult scientific problems I can think of and excels at them, she is constantly planning community-building events, and somehow she never misses a Bad Bunny night at Crybaby (in fact, she's the one who sends reminders to reserve tickets). Michael perseveres through challenges so bravely and always gives great feedback on scientific problems. He has been our PBRs champion and leader for two years now and I know he will continue to guide our team onto more winning seasons. Lily has great scientific intuition and I am so happy to see her growing more confident in her scientific career. She also has built the most impressive collection of Yerba Mate cans that 62 has ever seen and she brings a great energy to our lab events. Zirong is so talented and is so full of positive energy. She always has a smile on her face despite how difficult the first year of graduate school can be. I wish her success in all of her

future endeavors.

I had the pleasure to mentor an amazing undergraduate student in Ashley. She was so eager to learn more about my work and contribute in any way she could. I am so proud of her achievements at Berkeley and I know she has a bright future ahead.

To my family - thank you for your unwavering support. It is not at all easy to be on the other side of the country from you, but your constant phone calls, Facetimes, and visits make it bearable. Mom and Dad - you may not understand my science too well, but you always understand when I need emotional and parental support. Your unending love has gotten me through my PhD and you guide our family so expertly through the trials of life. You both set an exemplary example of how to give back to your community, work hard, and still have some fun along the way. Please continue taking good care of my favorite brown furry animal and long distance emotional support animal (Finnegan). To my siblings - I am so proud of you all and it is the blessing of a lifetime to be your older sister. Kristin - you are such an inspiration to me with your dedication to medicine and improving the lives of everyone around you. Lauren - you are so resilient and selfless with your time to lift up others around you. AJ - you work so hard to achieve your goals and I am beyond happy that you have followed me to California. My heart is so full with the love and admiration for my whole extended family and I am forever grateful to be blessed with such an amazing support network.

Chapter 1

Introduction

The core principle of materials science is to study how a material's structure and processing impact its properties and function [1]. To this end, it is vital to determine the structure of a material across length scales in order to understand the structure-property relationships, and therefore engineer better materials. In the field of polymer science, it can be difficult to directly determine the structure of these materials at the atomic-level due to inherent disorder and sensitivity to radiation damage. The most common method to gain atomic-scale information about polymers is through scattering techniques [2–5]. Scattering techniques produce incredibly valuable information about the structure of polymers in reciprocal space, yet the lack of direct information in position space can lead to ambiguities in deciphering the true atomic structure. Additionally, scattering techniques produce information about the material's bulk structure and heterogeneous structures may be averaged together. Transmission electron microscopy is an imaging technique that is widely and regularly used to produce direct, atomic-scale images of hard materials, yet it is rarely applied to study polymers due to the high radiation sensitivity of soft materials [1, 6–8]. A set of techniques called cryo-EM (or cryogenic transmission electron microscopy) has been developed by the structural biology community to primarily produce high resolution images of proteins [9]. It was only in 2017 that this set of techniques was first applied to image the atomic structure of synthetic polymers [10]. The purpose of this dissertation is to further develop the application of cryo-EM to a variety of synthetic polymers in order to study polymer self-assembly and ion-polymer interactions via direct atomic-scale images.

1.1   Cryogenic Transmission Electron Microscopy

Transmission electron microscopy (TEM) is an imaging technique where an electron beam is transmitted through a material to produce high resolution images of the material [1]. The nominal magnification is directly related to the energy of the electron beam. Therefore, very high energy electrons are needed to produce high resolution images [11]; yet when a polymer or other soft material is exposed to the high energy beam it is damaged very quickly by the

radiation from the beam [12, 13]. There are two main types of beam damage: knock on damage and ionization damage [14]. Imaging soft matter with electrons at 300 keV provides the best trade-off between these types of damage and is the standard operating conditions for high resolution imaging of soft materials [12, 13, 15, 16].

In order to minimize beam damage, a few techniques have been adopted. First, the sample to be imaged is cooled to around -170 °C to increase the radiation resistance of the sample and limit ionization damage [17, 18]. Then specialized instrumentation and data collection protocols are used in order to minimize the exposure of the sample to the electron beam [19]. Direct electron detectors are capable of capturing single electron events with millisecond time precision. The data that is collected is in the form of multiframe movies, where each frame of the movie typically has a total electron beam exposure of $1\ e^-/Å^2$. The advantage of collecting movies is that small motions can be corrected for, such as stage drift due to thermal gradients or sample movement from exposure to the electron beam [20, 21].

In the first step of data analysis, each frame in the movie is aligned to correct for the small spatial movement between frames, thereby improving the resolution [20]. It is common practice to use dose-weighting in this alignment process so that the initial frames where the sample has been exposed to a lower number of electrons are weighted higher than later frames which may have more radiation damage [20, 22]. The first step in analysis of the aligned images is to correct for the contrast transfer function (CTF) [1]. CTF correction accounts for image distortions caused by defocus and the spherical aberrations in the TEM and corrects for these distortions so that they don't affect the final image [23, 24]. Next, a machine learning algorithm is used to identify the locations of the particles and differentiate between the sample and the rest of the image. Oftentimes the user first manually determines the positions of the particles, or sample, in order to train the algorithm. Then, small boxes are extracted from the images at the position of the particles. These boxes are then entered into the 2D classification algorithm [22, 25, 26]. This algorithm uses an iterative optimization technique to average the boxes together and divide them in to classes based on shared features, thereby producing images in much higher resolution than what is seen in the input boxes. Additionally, this averaging and classification procedure can identify heterogeneity in the input boxes and separate them into different classes [10, 27]. The 2D images reported in this dissertation are the result of this 2D classification procedure.

1.2   Crystalline Diblock Copolymers

1.2.1   Polypeptoids

Peptoids are a class of synthetic molecules that have a structure similar to peptides, but the side chain is appended to the amide nitrogen rather than the α-carbon [28, 29]. Peptoids lack hydrogen bond donors on the backbone; therefore, interactions between the side chains are the dominant intermolecular interaction [30]. Peptoids also are not chiral, which makes it easier to design peptoids with targeted crystal structures.

Diblock amphiphilic polypeptoids can self-assemble into highly ordered nanostructures, such as two-dimensional nanosheets and one-dimensional nanofibers. The nanosheet structure has been widely studied for applications in self-repairing membranes [31], serving as a scaffold for protein recognition [32], and sensing toxic chemicals in live cells [33]. The nanofiber structure has been studied previously for applications in templating silica filaments [34]. It is of great interest to learn more about the self-assembly of polypeptoids so that molecules can be designed to target specific nanostructures a priori.

1.2.2 Poly(ethylene oxide)-*b*-polystyrene

Poly(ethylene oxide) (PEO) has been widely studied for applications as an electrolyte in lithium battery systems [35–37]. PEO has good electrochemical properties, is nonflammable, and is stable against lithium metal [35, 38]. Conventional liquid electrolytes are not stable against lithium metal; therefore, using PEO as an electrolyte could enable higher energy density batteries by substituting lithium metal for a graphite anode.

Previous work has been done on using a diblock poly(ethylene oxide)-b-polystyrene (PEO-PS or SEO) copolymer as both an electrolyte and separator in a lithium battery [39–41]. The PEO block is ionically conductive, while the PS block is mechanically rigid and blocks dendrite growth. Previous studies have used X-ray scattering to connect the morphology in a bulk sample to the transport properties and electrochemical performance [38, 42]. Other work has used computer simulations to study the atomic-scale structure and connect it to transport properties [43]. In order to continue improving polymer electrolytes for battery applications, a more thorough understanding of the structure-transport relationships for these materials is needed.

1.3 Structure of the Dissertation

This dissertation presents atomic-scale cryo-TEM images and characterization data of a variety of synthetic polymers.

Chapter 2 starts by investigating the effect of halogen atoms and halogen bonding in the self-assembly of diblock copolypeptoid nanosheets. The unique ability of covalently bonded halogen atoms to participate in halogen bonds can significantly change the crystal motifs in polypeptoid nanosheets. The effect of bound charges is further explored in Chapters 3 and 4. Chapter 3 uses a model polypeptoid nanofiber to study counterion condensation, a phenomena that is unique to highly charged polymers. The images in Chapter 3 are the first images ever produced (to my knowledge) of a cloud of unbound counterions near a charged polymeric surface. Further analysis on the images reveal the experimentally determined counterion distribution and a measurement of the population of condensed counterions. Chapter 4 uses a model system to systematically vary the relative amount of charges in a polypeptoid system to investigate precisely how bound charges affect self-assembly. Finally, Chapter 5 is devoted to a conventional diblock copolymer - SEO. In this chapter, SEO single crystals with and

without a lithium salt are synthesized and imaged at the atomic scale. The images are compared to known crystal structures of PEO to investigate how the polymer chains rearrange themselves with different concentrations of lithium salt.

Chapter 2

Halogen Bond Effects in Polypeptoid Nanosheets [1]

2.1 Introduction

Crystal engineering depends on control over interactions such as hydrogen bonding, dipolar interactions, $\pi - \pi$ interactions, and van der Waals interactions to name a few [44–47]. In spite of significant progress, it is not yet possible to design molecules that would yield a targeted crystal structure due to uncertainties in our knowledge of the relative importance of the multitude of relevant nonbonded interactions. It has long been known that crystals containing halogen atoms in close proximity pack differently from crystals devoid of them [44–46]. The most prominent feature of halogen atoms is their high electronegativity [48]. Following the pioneering work of Hassel [45] and others, there is, however, a growing recognition of the importance of halogen bonding in crystal engineering. Covalently bonded halogen atoms (chlorine, bromine, and iodine) tend to polarize and form an area of positive electrostatic potential on their surface along the direction of the covalent bond—this region of positive potential is called a σ -hole [49]. The σ-hole was recently imaged experimentally with Kelvin probe force microscopy to see the spatial distribution of positive and negative potentials on a covalently bonded bromine atom[50]. This anisotropic charge distribution allows halogen atoms to interact favorably with other electron-dense species. The strength of these interactions can be easily tuned by varying the neighboring atoms near the halogen [48], resulting in typical halogen bond strengths of approximately 1 - 5 kcal/mol [49]. In spite of this, many crystals compromising halogen atoms in close proximity do not contain halogen bonds [51–53].

Two halogen atoms dressed with σ-holes and in close proximity can interact attractively with two dominant motifs, labeled in the literature as type I or type II [44]. The type I motif

---

is symmetric, and the line segments connecting the carbon and halogen atoms in adjacent nonbonded halogen atoms are parallel. The type II motif is not symmetric, and the line segments connecting carbon and halogen atoms in adjacent nonbonded halogen atoms are at an angle greater than 30°; they are often orthogonal to each other. The term "halogen bond" only applies to the type II motif [44]. In their authoritative review, Mukherjee, et al. write "Type I is a geometry-based contact that arises from close packing and is found for all halogens. It is not a halogen bond" [44]. Establishing the underlying driving forces underlying the motifs is, however, non-trivial. Some models suggest that the motifs are driven by specific attractive forces along specified directions while others suggest the importance of nonspherical shapes arising from polar flattening [44]. It is thus not clear if the observed motifs arise due to increased attraction or reduced repulsion.

Peptoids are synthetic molecules similar to peptides with side chains appended to the amide nitrogens rather than the alpha carbons [27, 54]. They lack hydrogen bond donors on the backbone, making it easier to engineer peptoids with tunable properties since the intermolecular interactions between the side chains are of primary importance [55]. In this study, we present the crystal structures from three different peptoids in which the para-substituent on the aromatic side chain varies from hydrogen, to chlorine, and to bromine. In the crystalline state, adjacent polypeptoid molecules adopt V-shaped configurations, but adjacent V-shaped configurations can be either parallel or antiparallel, depending on chemical composition [56]. They are excellent model systems for studying halogen-halogen interactions as in the parallel configuration, the halogens adopt the type II motif, while in the antiparallel configuration, the halogens are in the type I motif. We determine the geometry of the halogen-halogen interactions in our system from atomic-scale images obtained by cryogenic transmission electron microscopy (cryo-TEM).

Molecular dynamics (MD) simulations were employed to study the relationship between intermolecular interactions and crystalline motifs. In the study of large, complex systems, the computational cost of molecular dynamics often dictates the use of empirical force fields which are not polarizable and, therefore, cannot account for the anisotropic charge distribution on a covalently bonded halogen atom [57]. One compromise employs force fields wherein the σ-hole is represented as a static, positive point charge attached to the halogen atom at a defined distance from the center of the halogen atom along the carbon-halogen covalent bond axis [58]. This is a common approach for studying the halogen bond [59–62], one that we use in this study. The importance of the σ-hole was assessed by comparing the simulation results with experimentally determined crystal structures. Our simulations show that the stability of both parallel and antiparallel crystals of the halogenated peptoids is similar if standard force fields that only account for the electronegativity of the halogens are used. Including the σ-hole, however, destabilizes the type II motif.

2.2 Experimental

2.2.1 Cryo-TEM

The TEM imaging was done at 300 KeV with a 20 eV energy filter on a Titan Krios G2 (FEI company) for Nte_4-Npe_6 and Nte_4-$N4Brpe_6$, and a JEOL-3200FSC (JEOL Ltd.) TEM for the Nte_4-$N4Clpe_6$ sample. To prepare the aqueous samples for imaging, they were drop cast on a molybdenum TEM grid with a holey gold film and continuous carbon film, then blotted using a Vitrobot, before being plunge frozen in liquid ethane and transferred to liquid nitrogen as is standard for preparing frozen hydrated samples [15]. Then, the vitrified grids were transferred to the TEM and a low-dose imaging procedure was employed [21]. The accumulated electron dose was limited to 20 e$^-$/Å^2 in order to minimize beam damage and the dose fractionated movies were recorded using Gatan K2 direct electron detectors.

The movies that were collected during the low-dose procedure were first aligned using MotionCor2 [20]. In order to reconstruct the atomic-scale images from the series of raw micrographs, first a crystal unbending procedure implemented in 2dx was used to correct for the contrast transfer function (CTF) and distortions within the lattice and also determine the locations of the unit cells [63]. Next, Relion, a single particle analysis software, was used to extract squares from the unbent micrograph at the locations of the unit cells [24, 25]. Finally, Relion's 2D reference-free class averaging algorithm was used to classify the unit cells into a series of classes based on the similarities between the boxes. More than 33,000 boxes (where one box contains approximately ten unit cells along the a direction) were averaged to reconstruct each atomic-scale image.

2.2.2 Polypeptoid synthesis

The synthesis method for the diblock peptoids is the same as has been described previously [56]. Briefly, a solid-phase submonomer synthesis method was employed to synthesize the diblock peptoids, allowing for a highly monodispersed polymer. The resulting polymer was dissolved at a concentration of 2 mg/mL in a THF/water mixture (50/50 vol%). The THF was slowly evaporated at 4 °C, and free-floating nanosheets were obtained after a few days.

2.2.3 X-ray diffraction

The nanosheet solutions were deposited on a Kapton window (25-μm thickness) and a rubber gasket spacer (0.75 cm thickness) with a hole in the center ($d = 0.25$ inch) was put on top. Then, the assembly was dried under vacuum and this process was repeated several times until enough nanosheets were placed on the Kapton window. Then, another Kapton window (25-μm thickness) was placed on top of the rubber spacer before placing it in the WAXS holder. WAXS measurements on the nanosheets were performed at Advanced Light Source (ALS) beamline 7.3.3 located at Lawrence Berkeley National Laboratory.
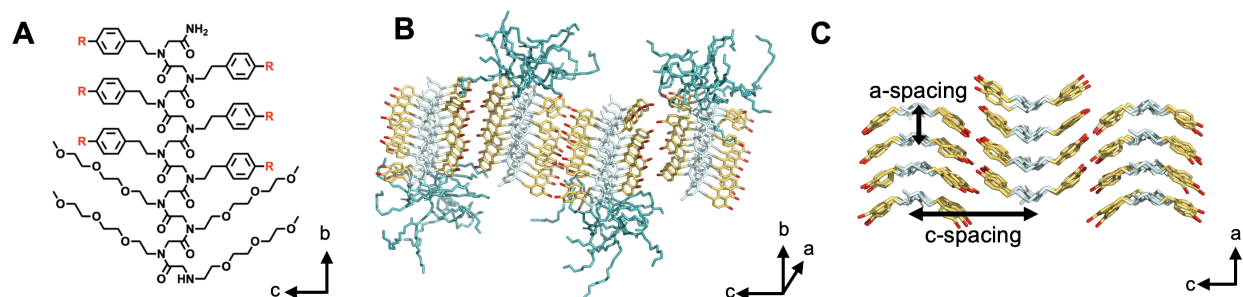
Figure 2.1: The chemical structure of the Nte_4-Npe_6 polypeptoids, with the variable X group in red (A). A 3-D atomic model of the Nte_4-Npe_6 nanosheets in solution is shown in (B), where the amorphous, hydrophilic blocks are teal, the backbone of the aromatic blocks is white, the phenyl group on the aromatic block is yellow, and the bromine atom is red. The projection through the *a-c* plane of this atomic model is shown in (C). The hydrogen atoms are omitted from these views for clarity.

2.3 Results and Discussion

2.3.1 Chlorine and Bromine Effects

Diblock polypeptoids consisting of a hydrophilic (*N*-2-(2-(2-methoxyethoxy)ethoxy) ethyl-glycine) (Nte) monomer and a hydrophobic *N*-(2- phenylethyl)glycine (Npe) monomer were synthesized via a solid-phase synthesis method [56]. A block ratio of 4 Nte: 6 Npe was chosen for this study. The chemical structure of the polypeptoids is shown in Figure 2.1(A), where the X group (shown in red) at the *para* position of the phenyl ring in the Npe block is either hydrogen, chlorine, or bromine. The three polypeptoid block copolymers are referred to as Nte_4-Npe_6, Nte_4-$N4Clpe_6$ and Nte_4-$N4Brpe_6$. Figure 2.1(B) is a 3-D atomic model of the Nte_4-Npe_6 nanosheets in solution [56]. The hydrophobic Npe blocks make up the well-ordered crystalline core of the nanosheets, which consists of the glycine backbone (in white) and the phenyl side chains (in yellow) with the bromine atom in the para position (in red). The hydrophilic Nte blocks remain amorphous in aqueous solution, and they are represented by teal in Figure 2.1(B). Figure 2.1(C) shows the projection through the *a-c* plane of the nanosheets, with the *a* spacing and *c* spacing denoted. As seen in Figure 2.1(C), the phenyl side chains adopt a V-shaped formation emanating from the glycine backbone. As the neighboring columns of V-shaped molecules are flipped relative to each other in Figure 2.1(C), this is referred to as the antiparallel packing configuration. The view through the *a-c* plane is what is observed in both high and low magnification TEM images, as shown in reference [56].

Table 2.1 contains characterization data of the crystalline nanosheets. We begin by discussing the unit cell dimensions of the crystals at room temperature obtained from wide an-

Peptoid sheet nomenclature	X group	a spacing, Å (WAXS)	a spacing, Å (cryo-TEM)	c spacing, Å (WAXS)	c spacing, Å (cryo-TEM)	T_m (°C)
Nte_4-Npe_6	H	4.5	4.6	16.2	16.1	93
Nte_4-$N4Clpe_6$	Cl	4.5	4.7	17.7	18.9	118
Nte_4-$N4Brpe_6$	Br	4.5	4.5	18.2	18.5	145

Table 2.1: Characterization data of polypeptoid nanosheets

gle X-ray scattering (WAXS), and melting temperatures determined by differential scanning calorimetry (DSC). These data were obtained from dry polypeptoid samples and reported previously in Xuan, et al. [56]. As seen in Table 1, the a spacing is constant at 4.5 Å for all sheets, but the c spacing increases when the X group is changed from hydrogen to chlorine to bromine. For reference, the van der Waals radius of hydrogen is 1.20 Å, that of chlorine is 1.75 Å, and that of bromine is 1.85 Å. Therefore, the increasing c spacing may be attributed to the increasing van der Waals radius of the atom in the para-position. The melting temperature also increases when the X group is changed from hydrogen to chlorine to bromine. The higher melting temperature of the different sheets may be explained by greater van der Waals interactions between the heavier atoms. However, additional effects, such as nonbonded halogen-halogen interactions, may also play a role.

Figure 2.2(A-C) shows bright field TEM images of the dry polypeptoid nanosheets. These low magnification images indicate that all three polypeptoid nanosheets adopt planar, rectangular morphologies. However, more sophisticated TEM imaging techniques are necessary to determine the molecular packing details of the nanosheet lattice. Frozen hydrated nanosheets were imaged using a low-dose cryo-TEM procedure to preserve their natural state and to minimize beam damage. The polypeptoid nanosheets, as with most soft matter, are sensitive to radiation damage when exposed to the high energy electron beam in a TEM. However, the signal-to-noise ratio is directly dependent on the amount of signal (the number of electrons)[17]. Using fewer electrons results in noisier images, but limiting the electron dose is necessary to prevent damage to the structure in materials and preserve high spatial frequency signals from the crystal lattice. In order to reconstruct an image with atomic resolution, thousands of raw, noisy images are averaged to recover the high-resolution information; this is a standard and widely-used practice in the structural biology community [9]. To briefly describe this technique, first distortions in the crystal lattice are corrected with 2dx [63], an electron crystallography program. Then Relion [64], a standard single particle analysis software package, is used to sort and average small sections of the corrected micrographs, resulting in a final, averaged image. The detailed protocol can be found in our previous work [10].

The final averaged cryo-TEM images of the nanosheets are shown in Figure 2.2(D-F). These images show the projection through the a-c plane of the nanosheets (as illustrated
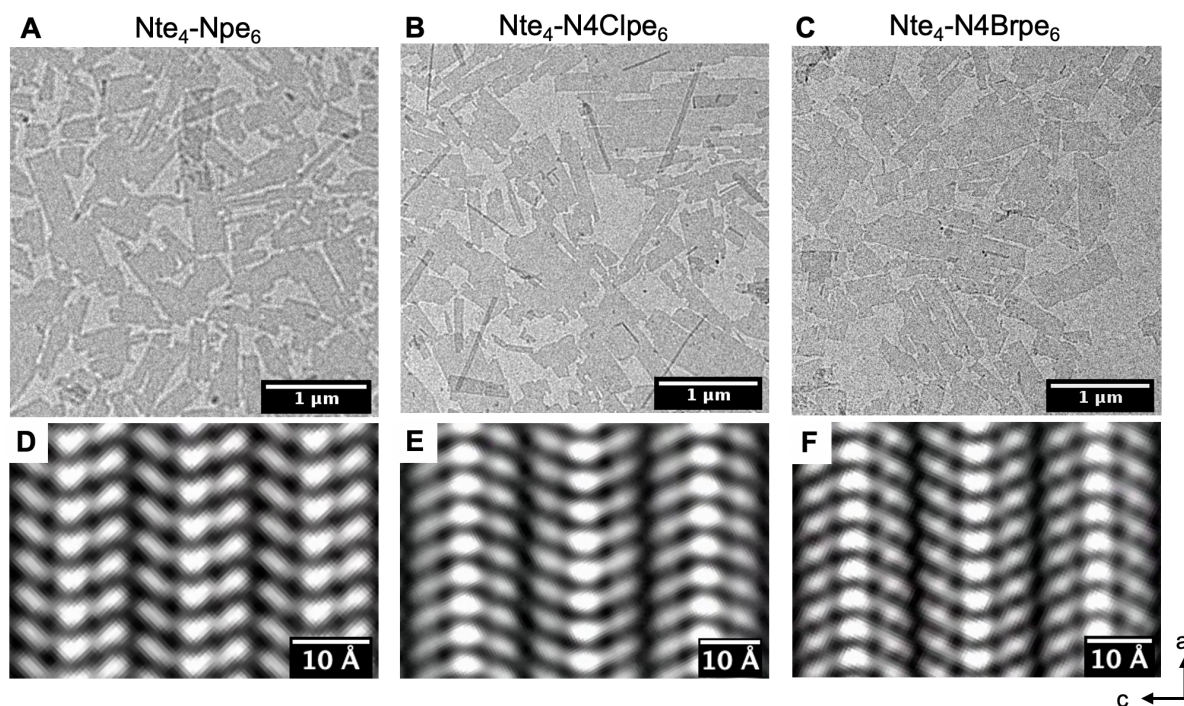
Figure 2.2: Bright field TEM images of the dry nanosheets formed by Nte_4-Npe_6 (A), Nte_4-$N4Clpe_6$ (B) and Nte_4-$N4Brpe_6$ (C), where the dark areas are the electron dense nanosheets. Shown below are the averaged experimental cryo-TEM images of the nanosheets formed by Nte_4-Npe_6 (D), Nte_4-$N4Clpe_6$ (E) and Nte_4-$N4Brpe_6$ (F). The light areas correspond to electron dense regions, where the brightest white spots are the peptoid backbone and the phenyl groups form the V-shaped structures out to the sides.

in Figure 2.1(C)). The light areas correspond to electron dense regions, where the brightest white spots are the peptoid backbone and the phenyl groups form V-shaped structures emanating from the backbone. Figure 2.2(D), the image of the Nte_4-Npe_6 nanosheets in which the X group is a hydrogen, shows all of the V-shaped structures pointing in the same direction. We call this the parallel V-shaped configuration. Figures 2.2(B) and 2.2(C) are the images of the Nte_4-$N4Clpe_6$ and Nte_4-$N4Brpe_6$ nanosheets, in which the X group is a chlorine and bromine atom respectively. In these images, the adjacent V-shaped structures point in opposite directions. We call this the antiparallel V-shaped configuration. The difference between the parallel and antiparallel configurations could not be revealed by conventional X-ray scattering or diffraction techniques due to the lack of direct phase information in position space. The a and c spacings determined by cryo-TEM are also given in Table 2.1. The cryo-TEM and WAXS data in Table 2.1 are consistent with each other; minor differences

are attributed to the differences in sample preparation and environment (wet versus dry and cryogenic temperature versus room temperature).

We use computer simulations to explore the underpinnings of the crystals shown in Figure 2.2. Quantum mechanical calculations show that the σ-hole occurs at an angle of 180° from the direction of the halogen – carbon covalent bond, imparting a high directionality to the resulting intermolecular interactions [49, 65, 66]. Typical force fields used in MD simulations cannot account for the anisotropic charge distribution of a covalently bonded halogen atom [60]. One strategy to model the σ-hole is to attach a massless, positive point charge to the end of the halogen atom. This construct accounts for both the strength and directionality of the σ-hole [58, 65, 66]. In our simulations, a point charge of +0.05 is used to represent both chlorine and bromine.

Figure 2.3(A) shows a model of a single diblock polypeptoid chain. The hydrogen atoms are omitted from Figure 2.3(A) for clarity. The black square in Figure 2.3(A) indicates the part of this molecule that is enlarged in Figures 2.3(B), 2.3(C), and 2.3(D). Figure 2.3(B) shows the configuration of the phenyl group with the para-substituted bromine in the Npe block without the extra point. Figure 2.3(C) shows the same phenyl group with the extra positive charge in gray attached to the end of the red bromine atom. The line segment connecting the carbon and bromine atoms is shown explicitly in Figure 2.3(D) as it relates directly to the geometry of nonbonded halogen-halogen interactions.

Our discussion of simulations focuses on bromine-containing peptoids. Similar results were obtained with chlorine-containing peptoids as shown in the supporting information. Two simulations were run for each bromine-containing system: one in which neighboring polypeptoids were initially arranged in a parallel configuration and a second in an antiparallel configuration. The constant area constraint was applied to the a-c plane during MD production simulations; the a spacing and c spacing were kept the same as the WAXS measurements. For both parallel and antiparallel configurations, the simulation started with sixteen polypeptoid molecules arranged into four molecules across (the c direction) and four molecules deep (the a direction). Then, the simulation was started and the molecules were allowed to relax. Prior studies on non-halogenated peptoids have shown that the internal energy of the parallel and antiparallel configuration are similar [10, 56].

Figure 2.4(A) displays the arrangement of Nte$_4$-N4Brpe$_6$ polypeptoids placed in the parallel configuration before the simulation is started. The box in 2.4(A) designates the side chains that are enlarged and flipped to show the projection through the a-c plane. The line segments connecting the carbon and bromine atoms on adjacent peptoid side chains are orthogonal to each other as is the case with the type II motif (see Figure 2.4(B)). Figure 2.4(C) indicates the nonbonded internal energy (defined as the sum of electrostatic and van der Waals contributions) versus time in the MD simulation of the polypeptoids initially placed in the parallel configuration. As seen in this graph, the parallel configuration is unstable and the nonbonded energy increases to +400 kcal/mol after 7 nanoseconds, which is when the simulation was stopped. Figure 2.4(D) shows a snapshot of the simulation at 7 nanoseconds, demonstrating that the peptoid nanosheet disassembles when placed initially in the parallel configuration.
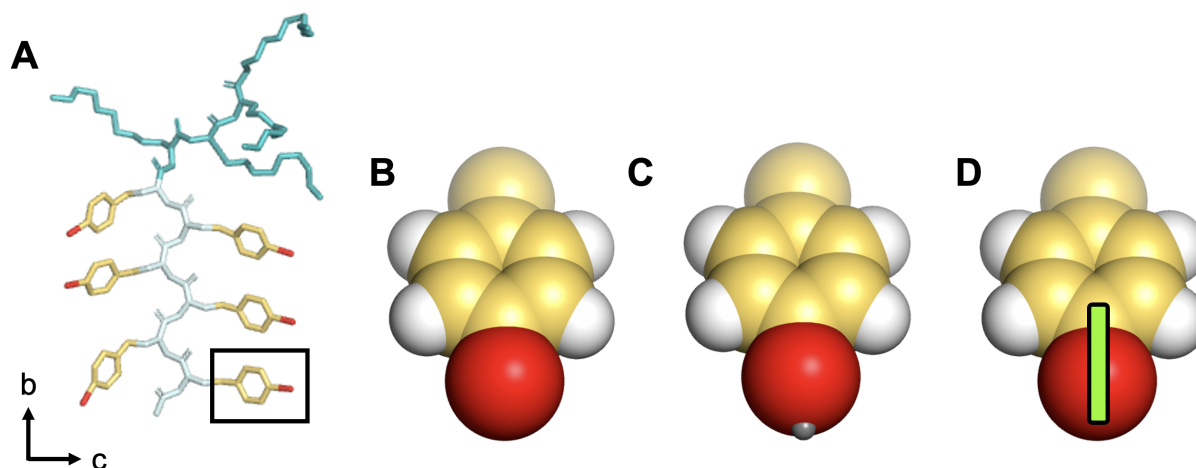
Figure 2.3: An atomic model of a Nte_4-$N4Brpe_6$ diblock polypeptoid is shown in (A) where the amorphous Nte groups are teal, the backbone of the aromatic Npe blocks is white, the phenyl group on the Npe blocks is yellow, and the bromine atom is red (hydrogen atoms are omitted for clarity). The black square in (A) indicates the part of the molecule that is enlarged in panels (B), (C), and (D). Panel (B) shows the phenyl sidechain on the Npe block without the positively charged extra point. Panel (C) shows the same model except with the extra point in gray on the end of the bromine atom, indicating the location of the σ-hole. Panel (D) is the same as (B) with a green line segment collinear with the carbon-bromine covalent bond.

Figure 2.4(E) displays the arrangement of Nte_4-$N4Brpe_6$ polypeptoids initially placed in the antiparallel configuration. The line segments connecting the carbon and bromine atoms on adjacent peptoid side chains are parallel to each other as is the case with the type I motif (see Figure 2.4(F)). Figure 2.4(G) plots the nonbonded internal energy of the simulation box versus simulation time. When the neighboring polypeptoids are initially placed in the antiparallel configuration, the nanosheet is stable and the nonbonded internal energy fluctuates in the range between -200 and -400 kcal/mol. Figure 2.4(H) shows the final arrangement of the relaxed polypeptoids that were initially placed in the antiparallel configuration obtained after 50 nanoseconds of the simulation. We use a statistical analysis of the simulation results to quantify the geometry of the nonbonded bromine-bromine interactions. Each simulation snapshot presents a wide variety of structures that do not neatly fall into the simple categories shown in Figures 2.4(B) and 2.4(F). We determine the geometry of the nonbonded bromine-bromine interactions in two steps:

In step one, we identify "interconnected structures" in our simulations. A cutoff distance, R_{cut}, was defined as 3 Å to search for the neighboring σ-holes for each halogen atom. This distance was chosen such that only the nearest neighboring σ-hole was included in the
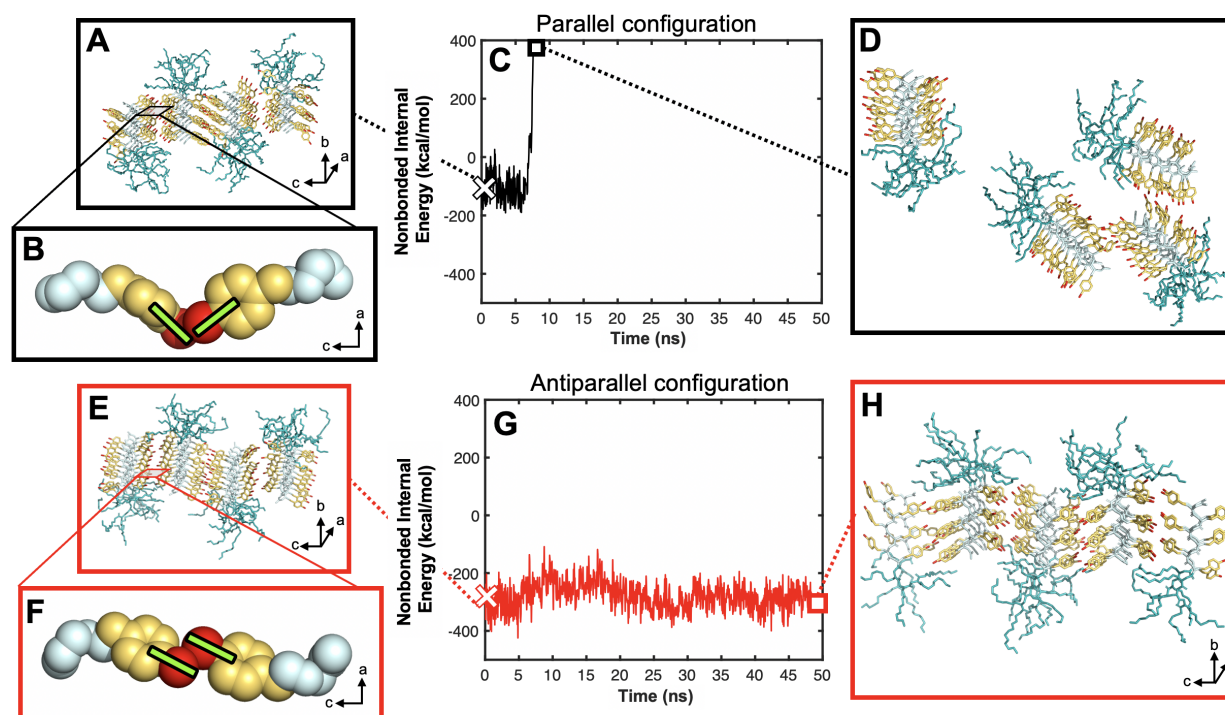
Figure 2.4: Results from MD simulations showing the nonbonded internal energy of the simulation versus time for the Nte_4-$N4Brpe_6$ nanosheets. Panel (A) shows the initial conformation of the polypeptoids when they are placed in the parallel configuration, and the black box indicates the region that is enlarged in panel (B). Panel (C) is the nonbonded internal energy over time for the polypeptoids initially placed in the parallel configuration. The nanosheet structure disorders after 7 nanoseconds of simulation time, and a snapshot of the polypeptoids at that time is shown in panel (D). Panel (E) shows the initial position of the polypeptoids when they are placed in the antiparallel configuration. The red box indicates the region that is enlarged in panel (F) to demonstrate how the C-Br bonds of adjacent bromine atoms are parallel to each other in the antiparallel configuration. Panel (G) shows the nonbonded internal energy over time for the polypeptoids initially placed in the antiparallel configuration, and this configuration remains stable throughout the 50 nanosecond simulation. Panel (H) is a snapshot of the simulation at 50 nanoseconds.

statistical analysis. An interconnected structure is one where the σ-hole of bromine atom 1 is within a sphere of radius R_{cut} emanating from the center of bromine atom 2, and the σ-hole of the bromine atom 2 is within a sphere of radius R_{cut} emanating from the center of bromine atom 1. Figure 2.5(A) shows an example of an interconnected structure. Since the parallel packing configuration disassembles in the simulation timeframe, only the trajectory

before the nanosheets disassembled was analyzed. The results of our analysis are shown in Table 2.2. In both parallel and antiparallel configurations, the fraction of bromine atoms that have at least one nonbonded σ-hole within the radius R_{cut} is similar (0.509 for parallel and 0.543 for antiparallel). However, as indicated in Table 2.2, the fraction of bromine atoms in interconnected structures is different for the two configurations: the interconnected structures obtained in the antiparallel configuration is a factor of three higher than that obtained in the parallel configuration. Our analysis suggests that the stability of fluctuating crystals is related to the concentration of interconnected structures.
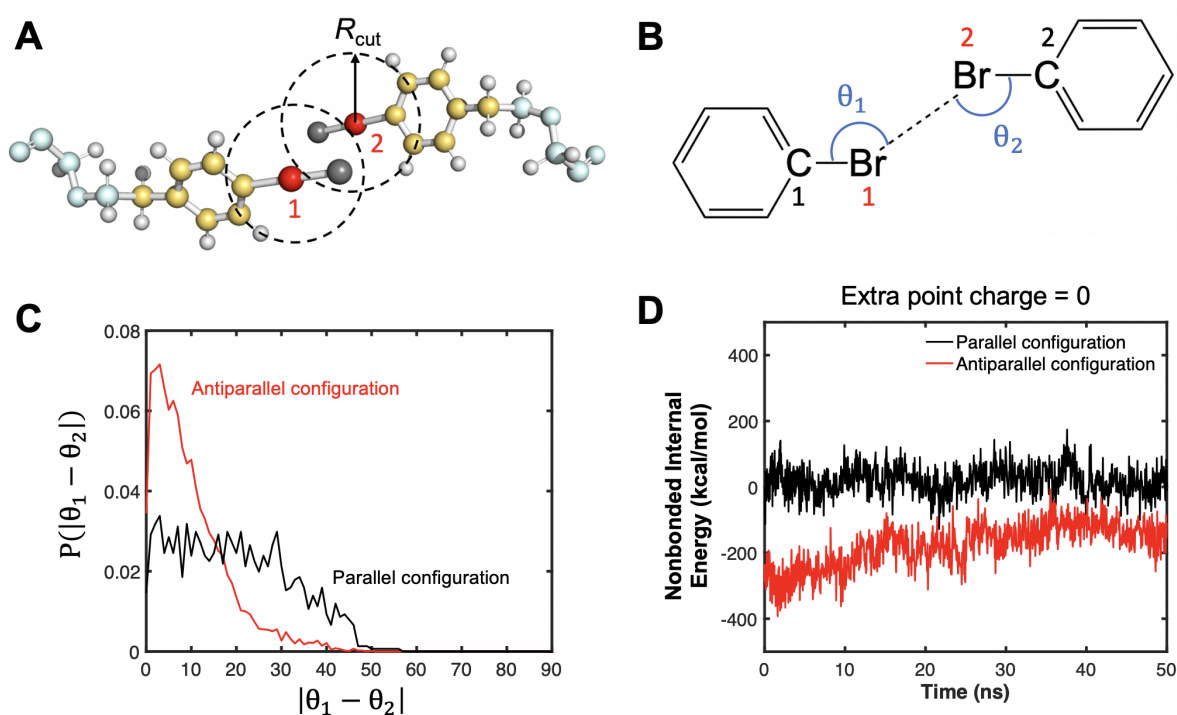
Figure 2.5: Analysis of the interconnected structures and additional simulation results. Panel A is an example of an interconnected structure between the bromine atoms and σ-holes on neighboring peptoids. Panel B shows the definition of θ_1 and θ_2 angles. Panel C shows the distribution of $|\theta_1 - \theta_2|$ in the antiparallel and parallel configurations. The system exhibits a type I motif when $|\theta_1 - \theta_2|$ is less than 15°, is quasi type I/type II when $15° < |\theta_1 - \theta_2| < 30°$ and is type II (a halogen bond) when $|\theta_1 - \theta_2| > 30°$ [44] The stable antiparallel configuration shows a type I motif while the unstable parallel configuration shows a quasi type I/type II motif. Panel D is results from MD simulations of Nte_4-$N4Brpe_6$ nanosheets without the σ-hole (the charge on the extra point was set to zero). The graph shows the nonbonded internal energy versus time. Both configurations appear stable but the antiparallel configuration exhibits a lower nonbonded internal energy.

Packing configuration	Fraction of bromines having at least one nonbonded σ-hole within R_{cut}	Fraction of bromines in interconnected structures
Parallel	0.509	0.139
Antiparallel	0.543	0.442

Table 2.2: Results of a statistical analysis on the bromine atoms in simulations of Nte_4-$N4Brpe_6$ nanosheets

In step 2, we analyze the interconnected structures to determine if the system contains type I or type II motifs. Angle θ_1 is defined between the carbon atom 1, bromine atom 1, and bromine atom 2; angle θ_2 is defined as the angle between the carbon atom 2, bromine atom 2, and bromine atom 1 (see Figure 2.5(B)). The absolute value of the difference between these angles (the value of $|\theta_1 - \theta_2|$) can be used to differentiate between type I and type II motifs. According to the definition set forth by Mukherjee, et al [44], a type I motif occurs when $|\theta_1 - \theta_2|$ is less than or equal to 15°. A type II motif occurs when $|\theta_1 - \theta_2|$ is greater than or equal to 30°. Intermediate values of $|\theta_1 - \theta_2|$ are described as being quasi type I/type II. In Figure 2.5(C), we show simulation results for the probability of obtaining a particular value of $|\theta_1 - \theta_2|$ as a function of $|\theta_1 - \theta_2|$ for both parallel and antiparallel configurations. For the parallel configuration simulation, the probability of obtaining values of $|\theta_1 - \theta_2|$ is nearly constant between 0° and 30° and it falls off to zero between 30° and 50°. If this configuration were stable, then the nature of nonbonded bromine atoms in peptoids would be classified as a quasi type I/type II motif. For the antiparallel configuration simulation, the probability of obtaining $|\theta_1 - \theta_2|$ is sharply peaked at 3° and tapers rapidly as $|\theta_1 - \theta_2|$ approaches 30°. We conclude that the brominated peptoids exhibit a type I motif.

In order to examine the effect of other driving forces on nanosheet packing geometry, additional simulations were run for the Nte_4-$N4Brpe_6$ nanosheets. For these simulations, the charge value for the extra point was changed from +0.05 to 0, thereby removing the effect of the σ-hole. Again, two simulations were run with the neighboring polypeptoids initially placed in the antiparallel or parallel configuration, and the nonbonded internal energy over simulation time is shown in Figure 2.5(D). While the internal energy was lower for the antiparallel configuration, both the antiparallel and parallel configurations remained stable over the whole simulation trajectory. The clear distinction in the stability of antiparallel and parallel configurations is lost when the σ-hole is absent. In addition, the equilibrium internal energy for the polypeptoids in the antiparallel configuration is much lower when the σ-hole is present, indicating the interconnected structures have a significant stabilizing effect (compare Figures 2.5(D) and 2.4(G)).

2.3.2 Iodine Effects

It has been established through MD simulations that the antiparallel packing configuration is commensurate with the type I motif and the parallel configuration is so with the type II [44] (see Figure 2.5). When the Nte_4-$N4Xpe_6$ nanosheets have chlorine or bromine as the X, they exhibit the antiparallel packing and type I motif. When the X is an iodine, the packing configuration changes to be a parallel packing configuration. In Figure 2.6, panel A shows the chemical structure of the Nte_4-$N4Ipe_6$ nanosheets. The low magnification TEM image of the nanosheet morphology is in panel B. These nanosheets adopt a similar rectangular morphology as the nanosheets seen in Figure 2.2. The averaged, high resolution cryo-TEM image of the Nte_4-$N4Ipe_6$ is shown in Figure 2.6(C). When the substituent in the *para*-position of the phenyl group is an iodine, the polypeptoids adopt a parallel packing configuration, indicating that a type II halogen bond is formed between the iodine atoms in neighboring rows of polypeptoids.

Figure 2.6: Panel A is the chemical structure of the Nte_4-$N4Ipe_6$ polypeptoid. Panel B shows a low magnification TEM image of the Nte_4-$N4Ipe_6$ polypeptoid nanosheets. Panel C is the averaged, high resolution cryo-TEM image of these polypeptoids. When the *para*-substituent on the phenyl group is an iodine, the polypeptoids adopt a parallel packing configuration, commensurate with a type II halogen bonding motif [44].

We used MD simulations to study the effect of halogen bonding in the Nte_4-$N4Ipe_6$ nanosheets. In the simulations, we used the same small positively charged extra point to model the σ-hole on the covalently bound iodine atom. Without the positive point charge, both parallel and antiparallel configurations were stable. However, when this small positive point charge was added, only the antiparallel packing configuration was stable; the addition of the positive charge actually *destabilized* the parallel packing configuration. This indicates that the simple model with a fixed point charge is not sufficient to model the iodine halogen bond in our nanosheets. Further work is needed to elucidate the root cause of the prevalence of the parallel packing configuration.

2.3.3 Fluorine Effects

To complete the series of halogens, we also studied Nte_4-$N4Fpe_6$ polypeptoids. The chemical structure is shown in Figure 2.7(A) and is the same structure as the other polypeptoids in this chapter except the *para*-substitutent on the phenyl is a fluorine atom. The Nte_4-$N4Fpe_6$ polypeptoid nanosheets adopt similar rectangular morphologies as the other polypeptoids studied (see Figure 2.7(B)). The high magnification image of the crystal structure of these polypeptoids, displayed in Figure 2.7(C), shows an antiparallel packing configuration. It has been well-established in this chapter that the antiparallel configuration is related to the type I halogen-halogen interaction motif. However, since fluorine is the smallest and least polarizable halogen, fluorine generally does not adopt the anisotropic charge distribution that gives rise to a σ-hole and therefore usually will not form halogen bonds [48, 67–69]. There are limited situations in which fluorine will participate in halogen bonding, but it is uncertain whether this is the case in the Nte_4-$N4Fpe_6$ polypeptoids or if the antiparallel configuration arises from other effects.
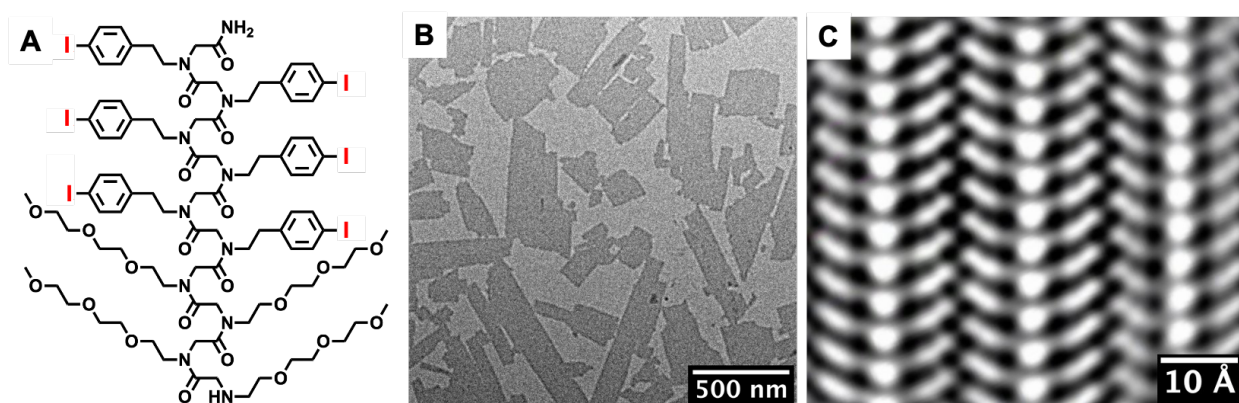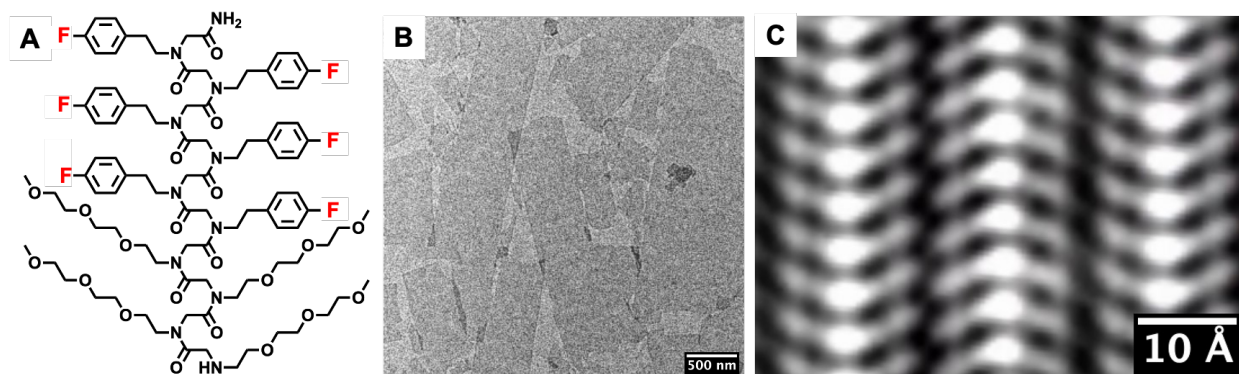

Figure 2.7: Panel A is the chemical structure of the Nte_4-$N4Fpe_6$ polypeptoid. Panel B shows a low magnification TEM image of the Nte_4-$N4Fpe_6$ polypeptoid nanosheets. Panel C is the averaged, high resolution cryo-TEM image of the atomic structure of these polypeptoids.

2.4 Conclusions

Nonbonded interactions between neighboring halogen atoms in molecular crystals are generally classified into two types: type I wherein the carbon-halogen bonds of adjacent peptoids in a crystal are parallel to each other and type II wherein these bonds are at an angle greater than 30°; they are often perpendicular to each other. Adjacent chains in polypeptoid crystals are generally found in either parallel or antiparallel configurations [56, 70]. The difference between parallel and antiparallel cannot be revealed by traditional techniques such as X-ray scattering. Crystalline nanosheets formed by a series of amphiphilic block copolypeptoids

were therefore imaged at the atomic-scale using cryo-TEM. The hydrophobic block of these molecules, which contain bromine atoms at the para-position on the phenyl ring, crystallize in the antiparallel configuration, which is commensurate with the type I motif. The presence of the halogen atoms is important as peptoids with hydrogen atoms in the para-position on the phenyl ring crystallize in the parallel configuration. MD simulations showed that σ-holes play an important role in determining crystal geometry in the halogenated samples. The stability of both parallel and antiparallel crystals of halogenated peptoids is similar if standard force fields that only account for the electronegativity of halogen atoms are used. In contrast, the parallel crystals are destabilized in simulations when the σ-holes are included. This indicates that additional factors beyond close packing may be responsible for the emergence of type I motifs. Further investigations are needed to understand the relative importance of the nonbonded interactions that dictate the crystal motifs when the atom in the para-position is a fluorine or iodine. Nevertheless, this work is a step toward to enabling crystal engineering of halogenated polypeptoids.

2.5   Acknowledgements

2.6   Supplementary Information

Figure 2.8 shows the Fourier transforms of the averaged cryo-TEM images shown in Figure 2.2 in the main text.
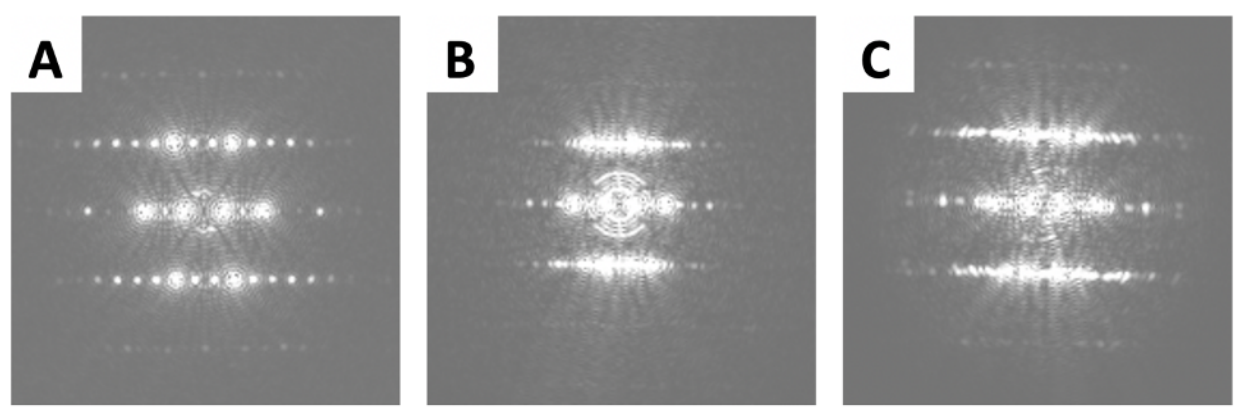
Figure 2.8: Fourier transforms of the high resolution TEM images shown in Figure 2.2. Panel A is the Fourier transform of the Nte_4-Npe_6 image (Figure 2.2(D)), Panel B is that of the Nte_4-$N4Clpe_6$ image (Figure 2.2(E)), and panel C is that of the Nte_4-$N4Brpe_6$ image (Figure 2.2(F)).

Figure 2.9: Projected potentials of the Nte_4-Npe_6 (A), the Nte_4-$N4Clpe_6$ (B), and Nte_4-$N4Brpe_6$ (C) polypeptoid nanosheets.
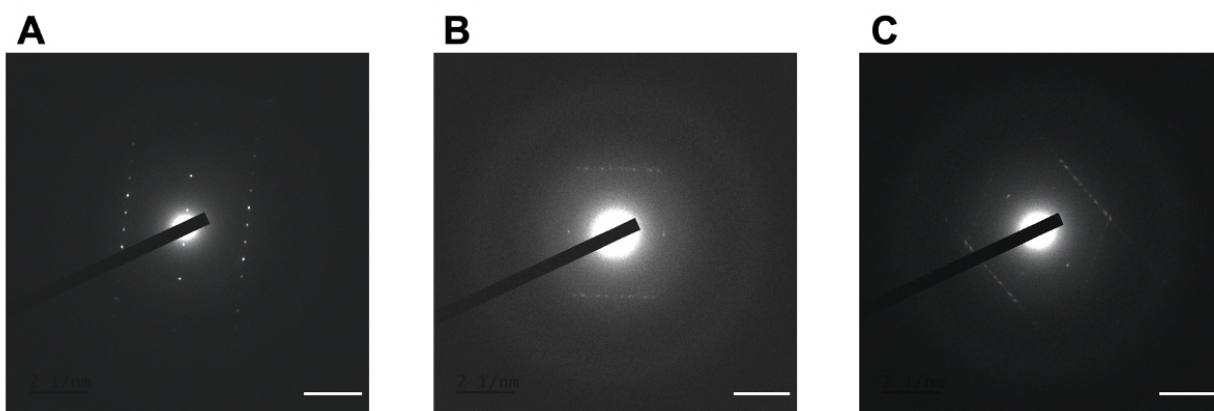
Figure 2.10: Cryo-electron diffraction patterns of the nanosheets formed by Nte_4-Npe_6 (A), the Nte_4-$N4Clpe_6$ (B), and Nte_4-$N4Brpe_6$ (C). The scale bar on each image is 2 nm^{-1}.

Chapter 3

Condensed Counterions Next to Polypeptoid Nanofibers

3.1 Introduction

There has been a long standing interest in the properties of aqueous solutions of charged macromolecules due to their importance in both natural and synthetic systems [71–74]. The properties of these solutions are significantly impacted by the locations of counterions relative to the fixed charges that are covalently bonded to the macromolecules [73–76]. In a pioneering study, Manning recognized that the coulombic repulsion between fixed charges can be reduced by the formation of ion pairs comprising the fixed charges and a fraction of the counterions [71, 77, 78]; these counterions are referred to as condensed counterions. The remainder of the counterions are dissociated, i.e. they are located at distances larger than the Bjerrum length from the charged macromolecule, and they diffuse freely. In the Manning theory, the equilibrium between condensed and dissociated counterions is governed by the dimensionless distance between the fixed ions normalized by the Bjerrum length of water [71, 77]. Counterion condensation is expected when this distance is less than unity. Figure 3.1 shows a diagram of the nanofiber with fixed charges, condensed counterions in the vicinity of the nanofiber, and dissociated counterions further away from the nanofiber. Explicit calculations of the counterion concentration as a function of position indicate that the concentration is highest next to the surface of the cylinder and decays with increasing distance. In fact, in the context of counterion condensation the molecular structure of the solvent is rarely discussed [79–81]. The implicit assumption is that the condensed counterions next to the nanofiber form contact ion pairs. In principle, however, ion pairs can be either contact ion pairs or solvent-separated ion pairs [82, 83]. Even in aqueous solutions of relatively simple salts, it is difficult to predict a priori if specific counterions will adopt contact or solvent-separated ion pairs [75, 84, 85]. In a theoretical study, Buckner and Jorgenson used two models to study ion pairing in aqueous tetramethylammonium chloride solutions. When a primitive model was used, the most stable configuration (lowest free
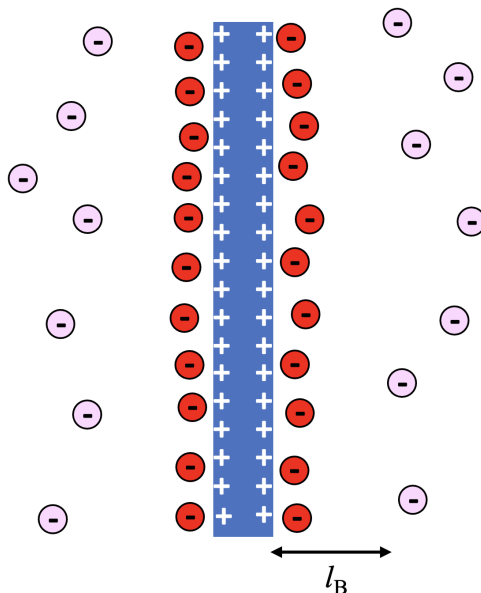
Figure 3.1: Diagram of a highly charged nanofiber with fixed positive charges, a layer of condensed counterions near the nanofiber (red), and dissociated counterions far away (pink). On average, the dissociated counterions are located at a distance greater than the Bjerrum length (l_B) away from the fixed positive charge.

energy) was determined to be contact ion pairs. However, Monte Carlo simulations indicated that the solvent-separated ion pair was more stable than the contact ion pair [86]. The phenomenon of counterion condensation has been studied by a variety of traditional experimental techniques, including osmometry [87], potentiometry [88], scattering [2, 89], and NMR [90, 91]. Our purpose is to present atomic-scale cryo-EM images of condensed counterions in a synthetic macromolecular system.

Cryo-EM has been used to image counterions in the vicinity of charged proteins. In particular, there have been significant efforts to use cryo-EM to image the 3D structure of protein ion channels [16, 92], as the transport of ions through these channels is vital to create potential differences across the cell membrane [93]. Previous studies have successfully used cryo-EM to determine the position of bound calcium and chloride ions in the ion cavity [92, 94–96]. In these studies, the locations of specific counterions in well-defined pockets are determined experimentally. In contrast, we seek to determine the locations of a large collection of counterions. We use cryo-EM to image a charged crystalline nanofiber composed of polypeptoids. Polypeptoids are a class of synthetic polymers with a structure similar to peptides but the side chain is appended to the amide nitrogen instead of the alpha carbon [10, 29, 54, 55, 97]. Amphiphilic diblock copolypeptoids comprising hydrophilic and hydrophobic blocks of equal length were dissolved in water. The ionic groups were located at the ends of

the side chains of the hydrophobic block to facilitate the imaging of condensed counterions. The block copolypeptoids self-assemble into nanofibers. This enables imaging of both the nanofiber with the fixed charge and condensed counterions in the vicinity of the fiber.

3.2 Experimental

3.2.1 Polypeptoid synthesis

3.2.1.1 Synthesis of aniline-based submonomer

Synthesis of Compound 1 (inset in Figure 3.14) was adapted from a published procedurem [98]. Di-tert-butyl decarbonate (5.0 g, 22.9 mmol) was dissolved in 1,4-dioxane (100 mL), followed by mixing with 4-(2-amioethyl)aniline (3.0 g, 22.1 mmol) acetic acid aqueous solution (100 mL, water/acetic acid = 90/10 % v/v). After stirring at room temperature for 18 hours, the reaction mixture was diluted with 300 mL deionized (DI) water, which was further extracted with diethyl ether (Et_2O) (3×150 mL). The aqueous phase was tuned to pH = 14 using 2 M NaOH aqueous solution, and the reaction mixture was then extracted with Et_2O (3×75 mL). The organic phase was washed with DI water (3×75 mL) before dried over anhydrous $MgSO_4$. After filtration, the volatiles were removed under vacuum to afford the product (Compound 1) as white solid (3.1 g, 59.3 %). ^{1}H NMR (δ in CD3OD, 400 MHz, ppm): 7.36-7.14 (m, 4H, Ar), 3.53-3.49 (m, H, -NH-), 2.92-2.90 (t, 2H, - CH_2-NH-), 2.77-2.74 (t, 2H, -CH_2-Ar), 1.53 (s, 9H, (-CH_3)$_3$), 1.19 (m, -NH_2).

3.2.1.2 Solid-phase submonomer synthesis of peptoid.

The polypeptoids were synthesized by a solid-phase submonomer synthesis method using Symphony X peptide synthesizer on 100 mg Rink amide resin (0.64 mmol/g; Novabiochem) by adapting reported procedures [99]. In brief, after de-protecting the FMOC group in the resin using 4-methylpiperidine (1 mL, 20 % v/v in DMF), each monomer synthesis includes two steps: bromoacylation and displacement. The bromoacylation was first performed by mixing bromoacetic acid (0.8 M) and N,N'-diisopropylcarbodiimide (DIC, 0.8 M) in DMF for 20 min at room temperature. Next, a nucleophilic displacement reaction was conducted by adding corresponding amine submonomer (1 M) in DMF for 30 min at room temperature. This bromoacylation-displacement cycle was repeated for each peptoid monomer in the target peptoid sequence, progressing from C-terminus to N-terminus (Compound 2 in Figure 3.15). At the end of each synthesis step, the resin was washed with ample DMF and then DCM to get rid of unreacted reagents. Upon completion of the sequence synthesis, the resin was dried with a nitrogen flow.

3.2.1.3   Cleavage, deprotection, purification, and formation of HCl salt.

The crude peptoid was cleaved from resin in a trifluoroacetic acid (TFA) cleavage cocktail (95 % TFA, 2.5 % triisopropyl silane, 2.5 % water), and shook for 30 mins at room temperature. The Boc-protection group in the peptoid was removed in the presence of TFA, generating the TFA salt form of the peptoid (Compound 3 in Figure 3.15). The cleavage solution was filtered through a polypropylene fritted cartridge and rinsed with DCM (3×6 mL). The collected solutions were dried using a Biotagen V-10 evaporator to afford a pale-yellow gel. The crude peptoids were purified using reverse-phase HPLC. The freshly cleaved peptoids were re-dissolved in acetonitrile (ACN)/isopropyl alcohol (IPA)/water (60/10/30 % v/v) at 20 mg/mL. The peptoid solution was purified using Waters reverse-phase HPLC with a XSelect HSS cyano column (5 μm, 18×150 mm^2). Solvent A is IPA/water/TFA (10/90/0.1 % v/v) and solvent B is IPA/ACN/TFA (10/90/0.1 % v/v). Flow rate was 12 mL/min with a linear gradient at 60-95 % solvent B over 30 min. The HPLC fractions were analyzed by a reverse phase LCMS equipped with an analytical XSelect HSS cyano column (5 µm, 4.6×150 mm column) and a MicroTOF electrospray mass spectrometry using the same solvents (solvent A and B) as in the reverse-phase HPLC. Flow rate applied was 0.4 mL/min with a linear gradient at 60-95 % solvent B over 30 min. A fluffy white powder with > 95 % molecular purity was collected by lyophilizing from acetonitrile/water (1:1, v/v) using Genevac evaporator. To generate the HCl salt form of the peptoid (Compound 4 in Figure 3.15), the peptoid powder was further dissolved in minimal ACN, followed by lyophilizing from 0.1 M aqueous solution of hydrochloric acid (HCl) to the HCl salt form (Compound 4 in Figure 3.15).

3.2.2   Self-assembly of polypeptoid nanofibers

To perform the self-assembly, the polypeptoids were dissolved in a mixture of THF and water (50/50 by volume). The THF was slowly evaporated at 4 °C, leaving self-assembled nanofibers in solution [27, 56].

3.2.3   Cryo-EM imaging and image processing

The TEM imaging was done at 300 keV with a 20 eV energy filter on a Titan Krios G3 (FEI company). To prepare the 9N-Nte$_6$-NBipe$_6\cdot$Cl and 9N-Nte$_6$-NBipe$_6\cdot$I polypeptoid solutions for imaging, first a continuous carbon film was added on top of a C-Flat TEM grid (Electron Microscopy Sciences). These solutions dewet the holey carbon grid and thus the continuous carbon film was used to obtain samples with uniform nanofiber distribution and ice thickness. The continuous carbon film was not needed for the 9N-Nte$_6$-NBipe$_6$ nanofibers. The presence of the continuous carbon film is accounted for in the CTF correction. The aqueous polypeptoid nanofibers were drop cast on the grid and blotted using a Vitrobot before being plunge frozen in liquid ethane. The grids were then transferred to liquid nitrogen as is standard for preparing frozen hydrated samples [9]. Then, the vitrified grids were transferred to

the TEM and a low-dose imaging procedure was employed [21]. The accumulated electron
dose was set to 40 e$^-$/Å^2 and about 3,000 dose fractionated movies were recorded using a
Gatan K2 direct electron detector. The movies were recorded in super resolution mode (0.5
binning) and the pixel size was 0.2826 Å/pixel. The defocus range used was -0.5 to -1.5
μm. The cryo-TEM data was analyzed in Cryosparc [22]. First, the movies were aligned
using full-frame alignment with dose-weighting to produce single images. Then CTF correc-
tion was performed on the single images to account for the aberrations and phase-flipping
from the TEM in the image. Particle picking was done manually to produce a template, then
Cryosparc's fiber tracing program was used to pick particles along the length of the nanofibers
with the template. 2D classification was completed to sort and average the particles into 50
classes, and was repeated multiple times to remove any classes that included the nanosheet
structure. In 2D classification, the parameters "enforce non-negativity" and "clamp-solvent"
were used to remove background noise and produce clear images of the nanofiber's structure.
The parameter "align filament classes vertically" was enabled to produce the final images.

3.3   Results and Discussion

3.3.1   Imaging Condensed Counterions

Diblock copolypeptoids with a hydrophilic (N-2-(2-(2-methoxyethoxy)ethoxy) ethylglycine)
(Nte) monomer and a hydrophobic (N-(2-(4-biphenyl)ethyl)glycine) (NBiPe) monomer were
synthesized via a solid-phase synthesis method [56]. The hydrophobic core of six adjacent
monomers at the C-terminus was engineered to contain a single ionic group. Thus, at the
ninth monomer from the N-terminus, an aniline-containing monomer N-(2-(4-aminophenyl)
ethyl)glycine was introduced. After synthesis, the polypeptoids were treated with hydrochlo-
ric acid to protonate the amine and form the chloride salt. This polypeptoid is referred to as
9N-Nte$_6$-NBipe$_6$·Cl. The chemical structure of this polypeptoid is shown in Figure 3.2(A).
To perform the self-assembly, the polypeptoids were dissolved in a mixture of THF and
water (50/50 by volume). The THF was slowly evaporated at 4 °C, leaving self-assembled
nanofibers in solution [27, 56]. To prepare frozen, hydrated samples, the polypeptoid solu-
tion was drop cast on a TEM grid and plunged into liquid ethane [9, 12, 15]. At this point,
the nanofibers are frozen in amorphous ice in their solvated state. The TEM grid was then
stored in liquid nitrogen before being transferred to a Titan Krios TEM for imaging. The
polypeptoid nanofibers, as with most soft materials, are sensitive to radiation damage [27,
56, 99]. We therefore used low-dose imaging procedures developed by the structural biology
community to image the nanofibers [14, 56, 100]. Thousands of dose-fractionated movies
were collected and processed using Cryosparc (a commercial software) [22]. The movies
were motion corrected and aligned to obtain single images. Then, contrast transfer function
(CTF) correction was performed to account for the aberrations and phase-flipping from the
TEM in the image. One of the images thus obtained is shown in Figure 3.2(B), where the
a and c crystallographic directions of one of the nanofibers are labeled. These nanofibers
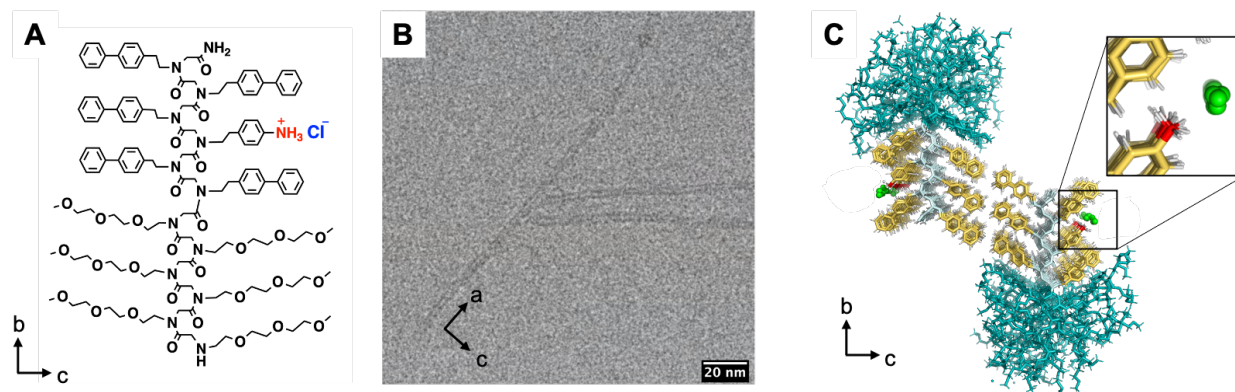
Figure 3.2: Chemical structure of the 9N-Nte$_6$-NBipe$_6$·Cl polypeptoid is shown in panel A. Panel B is a high resolution cryo-EM image of the nanofibers in vitreous ice where the a and c crystallographic directions are labeled. Panel C is a cartoon of the nanofibers. The inset shows an enlarged view of the bound amine and the unbonded chloride counterion. The hydrophilic Nte block (teal) is amorphous and extends into the solvent while the hydrophobic NBipe block (yellow) crystallizes. The yellow color shows the biphenyl side chains and the white is the polypeptoid backbone.

are two polypeptoid molecules wide in the c-direction, one polypeptoid molecule thick in the b-direction, and nearly infinite in the a-direction [56]. Figure 3.2(C) is a cartoon of a nanofiber viewed along the long axis of the nanofiber (the b-c plane). The hydrophobic block crystallizes while the hydrophilic block remains amorphous and extends into the aqueous phase [56]. The unbonded chloride counterions are shown in green near the positively charged amine groups which are part of the polymer chains (Figure 3.2(C)).

One portion of the self-assembled 9N-Nte$_6$-NBipe$_6$·Cl nanofiber solution was treated with sodium bicarbonate. The pH of the solution increased from 5.5 to 7.5, thereby neutralizing the amine groups (for reference, the pKa of 4-methylaniline is 5.2 [101]). The neutral polypeptoid thus obtained is called 9N-Nte$_6$-NBipe$_6$. A second portion of the self-assembled 9N-Nte$_6$-NBipe$_6$·Cl nanofiber solution was treated with 100x excess sodium iodide. This procedure exchanges the counterion from chloride to iodide, and we refer to this polypeptoid as 9N-Nte$_6$-NBipe$_6$·I [102]. The 9N-Nte$_6$-NBipe$_6$·Cl and 9N-Nte$_6$-NBipe$_6$·I polypeptoid solutions dewet the holey carbon grid and thus a continuous carbon film was deposited on the grid to obtain samples with uniform nanofiber distribution and ice thickness. The continuous carbon film was not needed for the 9N-Nte$_6$-NBipe$_6$ solutions. The presence of the continuous carbon film is accounted for in the CTF correction. The 9N-Nte$_6$-NBipe$_6$·Cl solutions were dominated by nanofibers, while the 9N-Nte$_6$-NBipe$_6$ and 9N-Nte$_6$-NBipe$_6$·I solutions contained both nanosheets and nanofibers. The nanosheet morphology is found in a wide variety of amphiphilic block copolypeptoids [10, 30, 56]. In the system studied here, the nanofiber morphology obtained in 9N-Nte$_6$-NBipe$_6$·Cl was stable for several months with no

9N-Nte$_6$ – N4NBiPe$_6$·Cl   9N-Nte$_6$ – N4NBiPe$_6$ 9N-Nte$_6$ – N4NBiPe$_6$·I
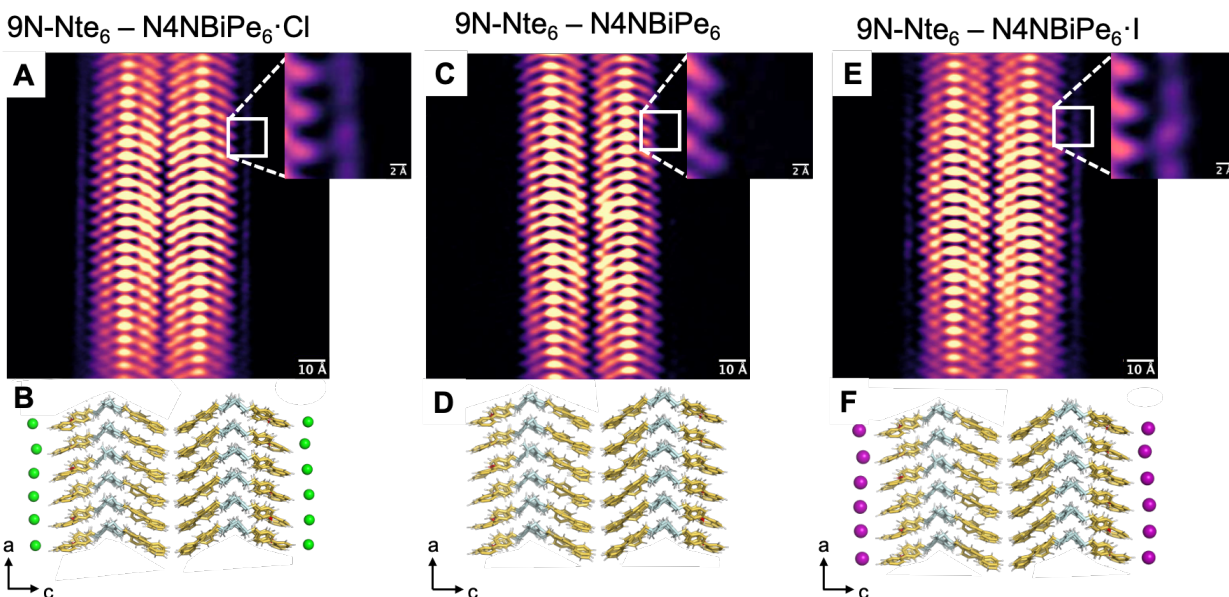
Figure 3.3: Averaged, high resolution cryo-TEM images of the nanofibers. Panel A is the experimental cryo-EM image of the 9N-Nte$_6$-NBipe$_6$·Cl nanofibers and the inset shows an enlarged view of the outside of the nanofiber. Panel B is a cartoon of the 9N-Nte$_6$-NBipe$_6$·Cl nanofibers where the chloride ions, in green, are on the outside of the nanofiber. Panel C is the image of the 9N-Nte$_6$-NBipe$_6$ nanofibers, with the cartoon of the fibers is below it in Panel D. Panel E is the image of the 9N-Nte$_6$-NBipe$_6$·I nanofibers with the corresponding cartoon below it. The iodide counterions are shown in purple in Panel F.

indication of nanosheet formation. The addition of sodium bicarbonate and sodium iodide to these solutions resulted in the conversion of some of the nanofibers into nanosheets within an hour (see Figures 3.13 and 3.12). The structures of the nanosheets formed by the 9N-Nte$_6$-NBipe$_6$ and 9N-Nte$_6$-NBipe$_6$·I polypeptoids are shown in Figure 3.7. High resolution imaging was completed on all three polypeptoid samples. The positions of the nanofibers were identified in the micrographs by Cryosparc [22]. Then boxes were extracted at those positions, aligned, and averaged into 2D classes. Any classes that contained boxes from nanosheets were filtered out. Figures 3.3(A), (C), and (E) show the results of this filtering and classification procedure.

All three images, which show the crystalline nanofiber in the *a-c* plane, contain V-shaped motifs. The brightest spot at the apex of the V represents the glycine backbone while the side chains emanate out to either side. The hydrophobic block of the 9N-Nte$_6$-NBipe$_6$·Cl polypeptoid is asymmetric (Figure 3.2(A)). Asymmetry is also seen when one examines each row in the corresponding image - a band is visible on one side of each row of polypeptoids in Figure 3.3(A). We posit that this band represents the chloride counterions and that the

hydrophilic nature of the $NH_3^+Cl^-$ group drives the ionic side chains toward the aqueous phase. The hydrophobic biphenyl groups without charged groups are driven toward the interior of the nanofiber. Figure 3.3(B) is a cartoon of the polypeptoid nanofiber where the unbound chloride counterions are placed outside the nanofiber. Figure 3.3(C) shows an image of the neutralized $9N$-Nte_6-$NBipe_6$ polypeptoid. This image does not show bands surrounding the nanofiber, confirming the absence of Cl^- counterions. Consistent with this observation, the corresponding cartoon in Figure 3.3(D) contains no counterions. Figure 3.3(E) shows an image of the $9N$-Nte_6-$NBipe_6 \cdot I$ polypeptoid. The bands surrounding the nanofiber confirm the presence of I^- counterions. The electron density within the nanofiber is much higher than that expected from a layer of condensed counterions. Consequently, the images in Figure 3.3 are dominated by the fiber. The insets in Figure 3.3(A), (C), and (E) focus on the edge of the fiber. The finger-like structures emanating from the left side represent the edge of the peptoid side chains that form the fiber. A layer of condensed counterions can clearly be seen in Figures 3.3(A) and (E). While the freezing process does not disrupt the nanofiber, its impact on the location of the counterions remains to be established. Since the importance of coulombic attraction, relative to entropy, increases with decreasing temperature, the counterions may move closer to the nanofiber during the freezing process. In other words, at room temperature the counterions could be further away from the nanofiber than indicated by the TEM images. The cores of all three nanofibers have a similar lattice structure. However, the characteristic distances between atoms are affected by the chemical composition of the polypeptoid. In Figure 3.4(A) we show the micrograph of the $9N$-Nte_6-$NBipe_6 \cdot Cl$ nanofiber and define four distances – three distances related to the polypeptoid crystalline core and one distance related to the location of the ion. The distances obtained from all three nanofibers are listed in Panel B of Figure 3.4 (see SI for calculation details). The distance between adjacent polypeptoid molecules along the nanofiber axis is, to a good approximation, unaffected by differences in chemistry (a-spacing = 4.6 Å ± 0.1 Å). The a¬-spacing of virtually all polypeptoid crystals is between 4.5 and 4.6 Å [3]. The distance between adjacent polypeptoid backbones in the c-direction is similar in the charged and uncharged polypeptoids (c-spacing = 26.4 Å ± 0.5 Å). The term ion distance, d_{ion}, is used to quantify the distance between the center of the positively charged nitrogen atom on the amine group and the center of the negatively charged halogen counterions in solution along the c-direction. The ion distances for $9N$-Nte_6-$NBipe_6 \cdot Cl$ and $9N$-Nte_6-$NBipe_6 \cdot I$ are 4.7 Å and 5.5 Å, respectively.

The distance between fixed charges in our nanofibers, a, is 4.6 Å (a-spacing) which is less than the Bjerrum length of water, $l_B = 7.1$ Å [78]. We therefore expect some fraction of the halide counterions, θ, to be condensed [71, 77]. The Manning theory for condensation of univalent ions gives $\theta = 1 - \frac{a}{l_B}$ [77] which gives $\theta = 0.35$. This theory does not distinguish between chloride and iodide ions. We used the cryo-EM images to obtain an experimental estimate of θ. The image intensity, averaged along the a axis, was computed as a function of position along the c axis. The resulting plot of intensity versus position for the $9N$-Nte_6-$NBipe_6 \cdot Cl$ nanofiber is shown in Figure 3.4(C). The outermost set of peaks in this figure represent the condensed Cl^- counterions while the remainder represents the peptoid

	9N-Nte$_6$ – NBiPe$_6$·Cl	9N-Nte$_6$ – NBiPe$_6$	9N-Nte$_6$ – NBiPe$_6$·I
a-spacing (Å)	4.6	4.5	4.6
c-spacing (Å)	26.7	25.9	26.5
d$_{ion}$ (Å)	4.7	--	5.5
% condensed counterions	83%	--	33%
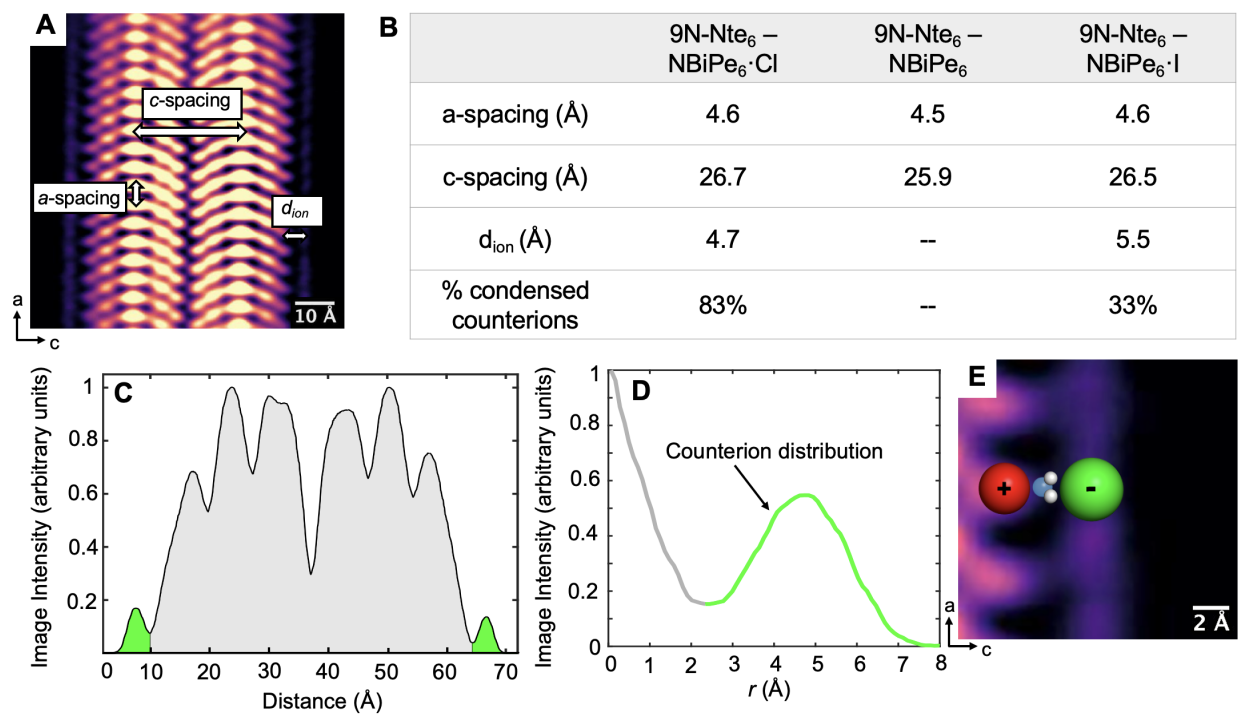
Figure 3.4: Measured quantities from high resolution images. Panel A shows the micrograph of 9N-Nte$_6$-NBipe$_6$·Cl and defines the measured lengths. Panel B is a table of the measured lengths of each nanofiber. The error on all distance measurements is ± 0.2 Å. Panel C is a line profile of the image in Panel A where average intensity is plotted as a function of distance along the c axis. Panel D plots the image intensity versus r where r is the distance in the c direction and $r = 0$ is the position of the positively charged nitrogen bound to the peptoid. Panel E is the inset from Figure 3(A), where the positively charged nitrogen, water molecule, and negatively charged chloride counterion are superimposed over the image. The three species are all drawn to scale.

nanofiber. We define the total area under the condensed counterion peaks on both sides as
A_{Cl-} (green in Figure 3.4(C)). We define the area under the peptoid peaks as $A_{peptoid}$(gray
in Figure 3.4(C)). If all the Cl^- counterions were condensed and the peptoid monomers
were inflexible and in perfect registry, then the ratio $A_{Cl-}/ A_{peptoid}$ would be $17/744 =$
0.023, based on the electron density of the different species. The measured value of $A_{Cl-}/$
$A_{peptoid}$ was 0.019. Dividing the two values, we obtain a crude estimate for the fraction of
condensed counterions, $\theta = 0.83$. While our estimate of θ is based on many simplifying
assumptions, our analysis illustrates that the measured contrast of the condensed counterion
layer is consistent with expectation based on the known electron densities of the nanofibers
and the counterions. In Figure 3.4(D), we plot image intensity as a function of position
along the c-axis, r. We define $r = 0$ as the nominal location of the positively charged
nitrogen (the fixed ion). The measured intensity at $r < 2.5$ Å is dominated by the nanofiber
contributions. The peak between $r = 2.5$ and 8 Å represents the distribution of condensed
counterions. It is perhaps worth noting that at $r = 8$ Å, a distance that is slightly larger
than the Bjerrum length of water, the measured intensity is negligible. We conclude that the
non-condensed chloride counterions diffuse randomly in the neighborhood of the nanofiber
and are thus not detected by cryo-EM. We conducted the same analysis on the 9N-Nte$_6$-
NBipe$_6$·I nanofibers and found results similar to those for chloride in Figure 3.4(C). In this
case the fraction of condensed counterions, θ was 0.33 (see Figures 3.9 and 3.10). It is
reasonable to assume that a quantitative theory of counterion condensation would include
the effect of specific interactions between the counterions and the fixed charges, between
the counterions themselves, and between the ions and water. Because iodide ions are less
electronegative and larger than chloride ions, we expect less counterion condensation in the
9N-Nte$_6$-NBipe$_6$·I nanofibers. Given the uncertainties in our quantitative analysis of the cryo-
EM data, the quantitative agreement between the theoretical value of θ and that obtained
in the 9N-Nte$_6$-NBipe$_6$·I nanofibers may be fortuitous. Nevertheless, the analysis of the
cryo-EM data in terms of θ firmly establishes that the contrast between the counterion layer
and the polypeptoid nanofiber is qualitatively consistent with that expected from condensed
chloride and iodide ions. Most theories of counterion condensation predict that the ion
concentration decays monotonically with increasing r [79, 90, 103, 104]. In other words,
the peak concentration is expected at the surface of the charged nanofiber ($r = 0$). Heyda
and Dzubiella used atomistic simulations to study counterion condensation of cations on
charged peptides [105]. In general, the condensed layer exhibits two peaks, one at $r = 0$ and
the other in the vicinity of $r = 5$ Å. In the particular case of Cs^+, the dominant peak was
at $r = 5$ Å. These results suggest the need to include atomistic details in the modeling of
condensed counterions. In both 9N-Nte$_6$-NBipe$_6$·Cl and 9N-Nte$_6$-NBipe$_6$·I nanofibers, the
distance between the fixed and condensed counterions is in the vicinity of 5 Å. This is similar
to the typical range for the separation between halides and positively charged coordinating
atoms in proteins [106]. For reference, the ionic radius of chloride is 1.75 Å and that of iodide
is 1.98 Å. The hydration shells of dissociated chloride and iodide ions in aqueous media have
been studied by computer simulations. In reference [107], the dominant solvation shells of
chloride ions were shown to contain 5 or 6 water molecules with radii of 4.0 and 4.5 Å,

respectively. In reference [108], the dominant solvation shells of iodide ions were shown to contain 6 or 7 water molecules. The radius of the solvation shell based on the overall pair distribution function was determined to be 5 Å. Based on NMR studies, Fraenkel and Kim concluded that ion pairs involving anilinium cations are separated by water molecules in the presence of both chloride and iodide anions [84]. The distances reported in Figure 3.4(B) indicate that the condensed counterions in $9N\text{-}Nte_6\text{-}NBipe_6\cdot Cl$ and $9N\text{-}Nte_6\text{-}NBipe_6\cdot I$ nanofibers are solvent-separated ion pairs.

3.3.2   3D Reconstruction

In addition to 2-D imaging, a 3-D image reconstruction was performed for the $9N\text{-}Nte_6$-$NBipe_6$ polypeptoid nanofibers. Since the TEM grids for these samples did not have a continuous carbon film, the nanofibers were randomly oriented in the vitreous ice, therefore enabling a reconstruction of the full 3-D structure [9, 99]. The results of this 3-D reconstruction are shown in Figure 3.5. Panel B is the same view through the $a\text{-}c$ plane that is shown in Figure 3.3 (i.e. the front view of the nanofibers). Panel A is the $b\text{-}c$ plane (i.e. end view) and panel C is the $a\text{-}b$ plane (side view). As discussed earlier (see Figure 3.3) the nanofibers adopt a V-shaped conformation when looking down the backbone of the nanofibers, which is defined as the $a\text{-}c$ plane. The end of the nanofibers, the $b\text{-}c$ plane, shows two polypeptoids next to each other. The two brightest lines in this image are the backbones of two polypeptoids and the intensity on either side of those bright lines is the side chains. The spacing between the backbones in the c-direction is 25.9 Å, the same as measured from the projection through the $a\text{-}c$ plane in Figure 3.3(C). As with other polypeptoid nanostructures, these nanofibers are only one molecule thick (i.e. a monolayer) as seen in Figure 3.5(A) [99, 109]. Panel C of Figure 3.5 shows the side view of the nanofibers. The bright lines are the backbones of the polypeptoids viewed down the length of the backbone. The spacing between backbones in the a-direction is 4.5 Å, the same as the quantity measured from the 2D image in Figure 3.3(C). The side chains are not visible in this projection.

3.4   Conclusions

The properties of aqueous solutions of charged macromolecules depend on the arrangement of dissociated and condensed counterions. While there have been numerous theories and simulations that quantify the arrangement of counterions [5, 104, 105], their predictions have not yet been tested against atomic-scale images. Cryogenic electron microscopy is a powerful tool for obtaining atomic-scale images of soft materials. However, most of the images in the literature show atoms connected to each other by covalent bonds [6, 16, 94, 110]. The fact that interatomic distances are well-defined in this case is important because high resolution cryo-EM requires averaging about 10,000 individual images. Since dissociated counterions diffuse randomly, they cannot be imaged using averaging-based cryo-EM. Prior to our work, it was not clear if condensed counterions were detectable via average-based
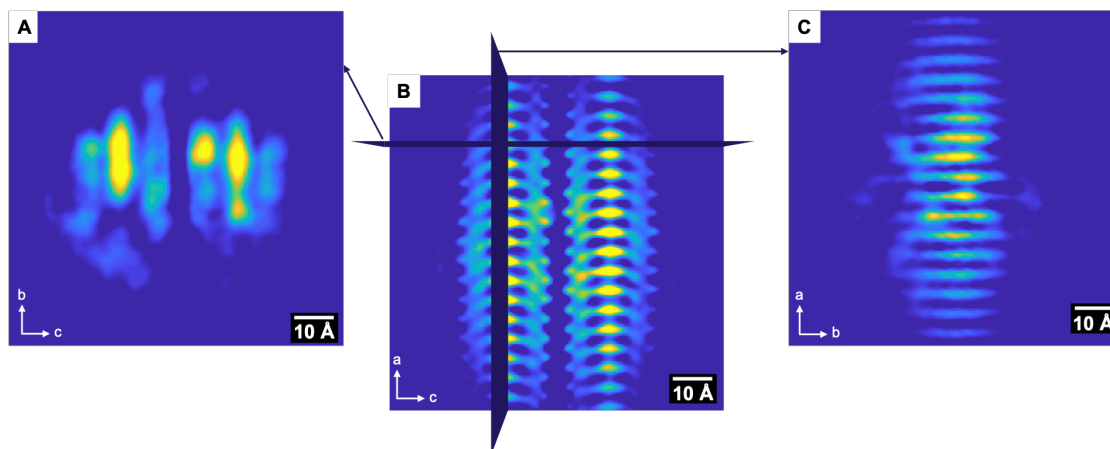
Figure 3.5: 3-D reconstruction of 9N-Nte$_6$-NBipe$_6$ polypeptoid nanofibers. Panel A shows the projection through the b-c plane, panel B is the a-c plane (the same view shown in Figure 3.3), and panel C is the a-b plane.

cryo-EM. We designed a positively charged polypeptoid nanofiber that was ideally suited for imaging condensed counterions. The cross-section of the nanofiber was rectangular and the fixed positive NH_3^+ charges were placed on two opposite sides of the rectangle. Current theories on counterion condensation rarely distinguish between contact ion pairs and solvent-separated ion pairs, and the probability of finding condensed counterions as a function of distance from the fixed charge generally decreases monotonically with increasing distance [104, 111–113]. The distribution of distances in between the fixed and condensed halide counterions (Cl^- and I^-) determined in this study were peaked at distances of 4.7 and 5.5 Å from the fixed charge for chloride and iodide, respectively. This indicates the presence of solvent-separated ion pairs in our system. Based on energetics alone, one expects contact ion pairs as they would reduce the net charge on the nanofiber. However, this would also reduce the entropy of the condensed counterions [80, 114]. It is possible that the formation of solvent-separated ion pairs is due to entropic considerations.

3.5   Acknowledgements

3.6   Supplementary Information

Figure 3.6: STEM-EDS was used to investigate the chemical composition of the 9N-Nte$_6$-NBipe$_6$·Cl and 9N-Nte$_6$-NBipe$_6$·I polypeptoids. Panel A shows the STEM image inset in the EDS spectra for 9N-Nte$_6$-NBipe$_6$·Cl. The peak for chloride at 2.6 keV is clearly visible, confirming the presence of chloride in the polypeptoid sample. Panel B shows the results for 9N-Nte$_6$-NBipe$_6$·I, where the iodide peak is seen at 3.9 keV.

The procedure to analyze the atomic structure of the nanosheets varied slightly from that for the nanofibers. In order to reconstruct the atomic-scale images of the nanosheets, first a crystal unbending procedure implemented in 2dx was used to correct for the contrast transfer function (CTF) and distortions within the lattice and also determine the locations of the unit cell [63]. Next, Relion, a single particle analysis software, was used to extract squares from the CTF-corrected micrograph at the locations of the unit cells [25]. Finally, Relion's 2D reference-free class averaging algorithm was used average the unit cells into classes. The results of this averaging and classification procedure are shown in Figure 3.7. The Fourier transforms of the images are also shown in Figure 3.7.
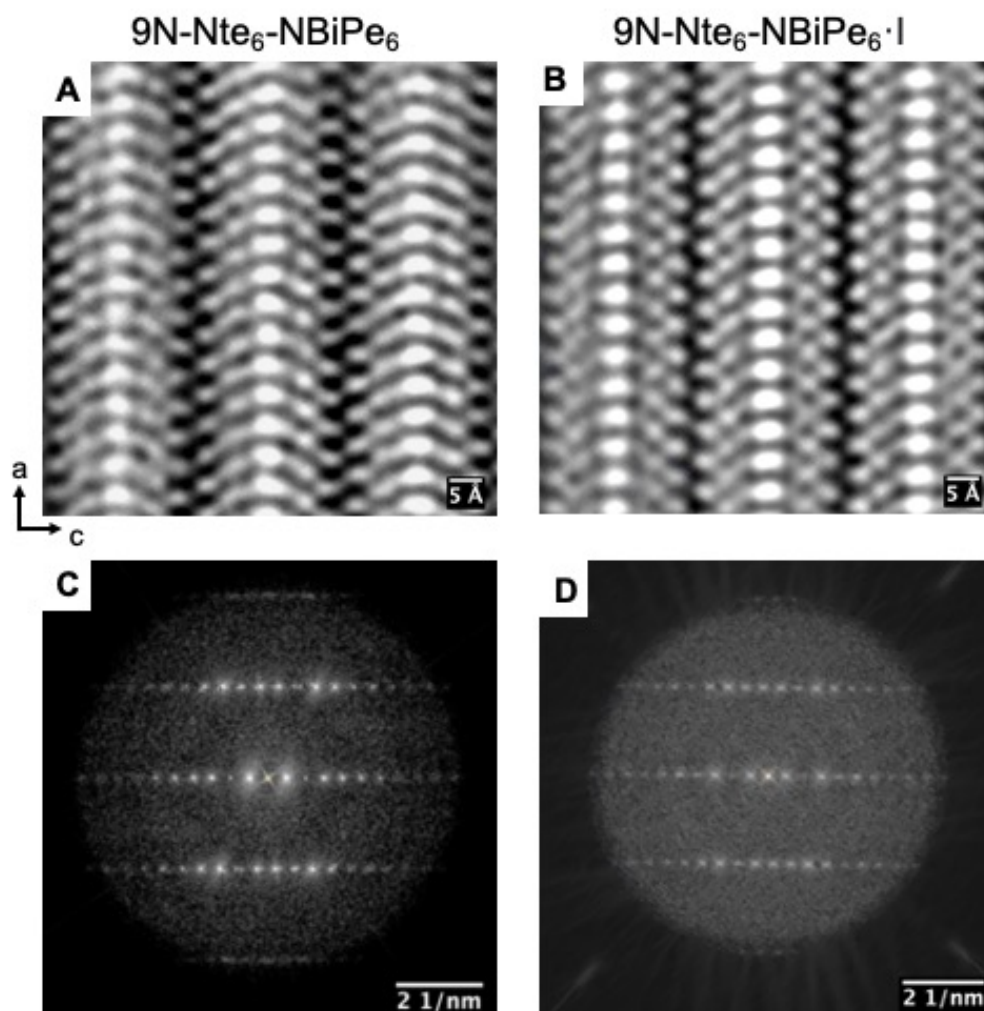
Figure 3.7: Atomic structure of nanosheets formed by 9N-Nte$_6$-NBipe$_6$ and 9N-Nte$_6$-NBipe$_6$·I nanosheets in panels (A) and (B), respectively. The Fourier transforms are shown below in each image in (C) and (D).
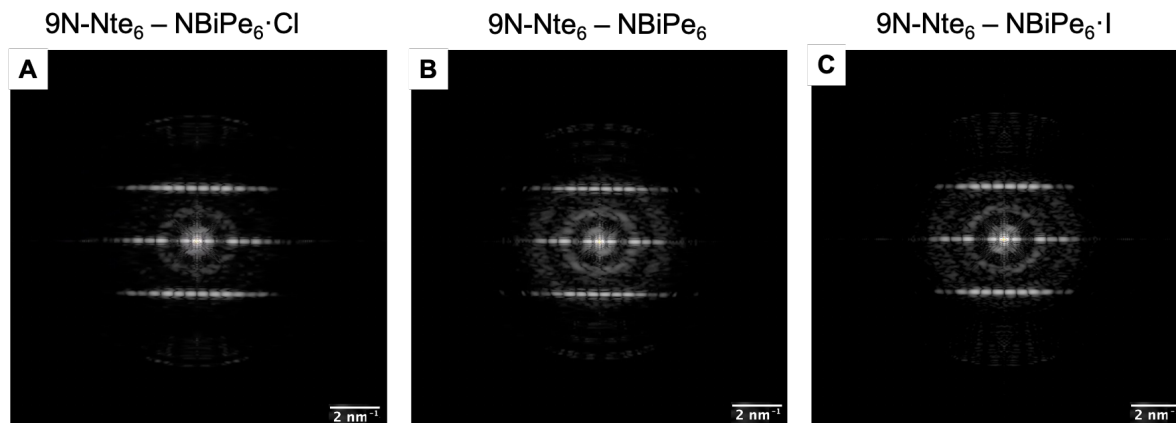
Figure 3.8: Panel A shows the Fourier Transform of the image 9N-Nte$_6$-NBipe$_6$·Cl nanofibers shown in Figure 3.3. Panel B is that for the 9N-Nte$_6$-NBipe$_6$ nanofibers, and panel C for the 9N-Nte$_6$-NBipe$_6$·I nanofibers.
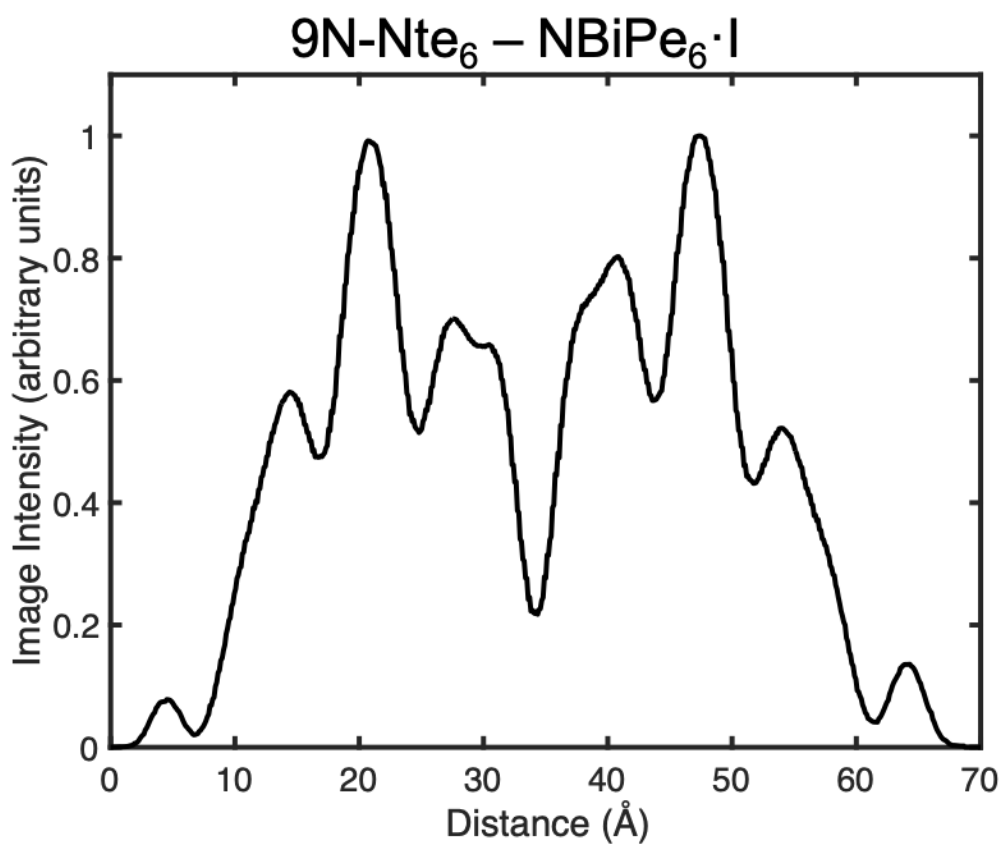
Figure 3.9: Line profile of the image of the 9N-Nte$_6$-NBipe$_6$·I polypeptoid nanofibers shown in Figure 3.3(E).
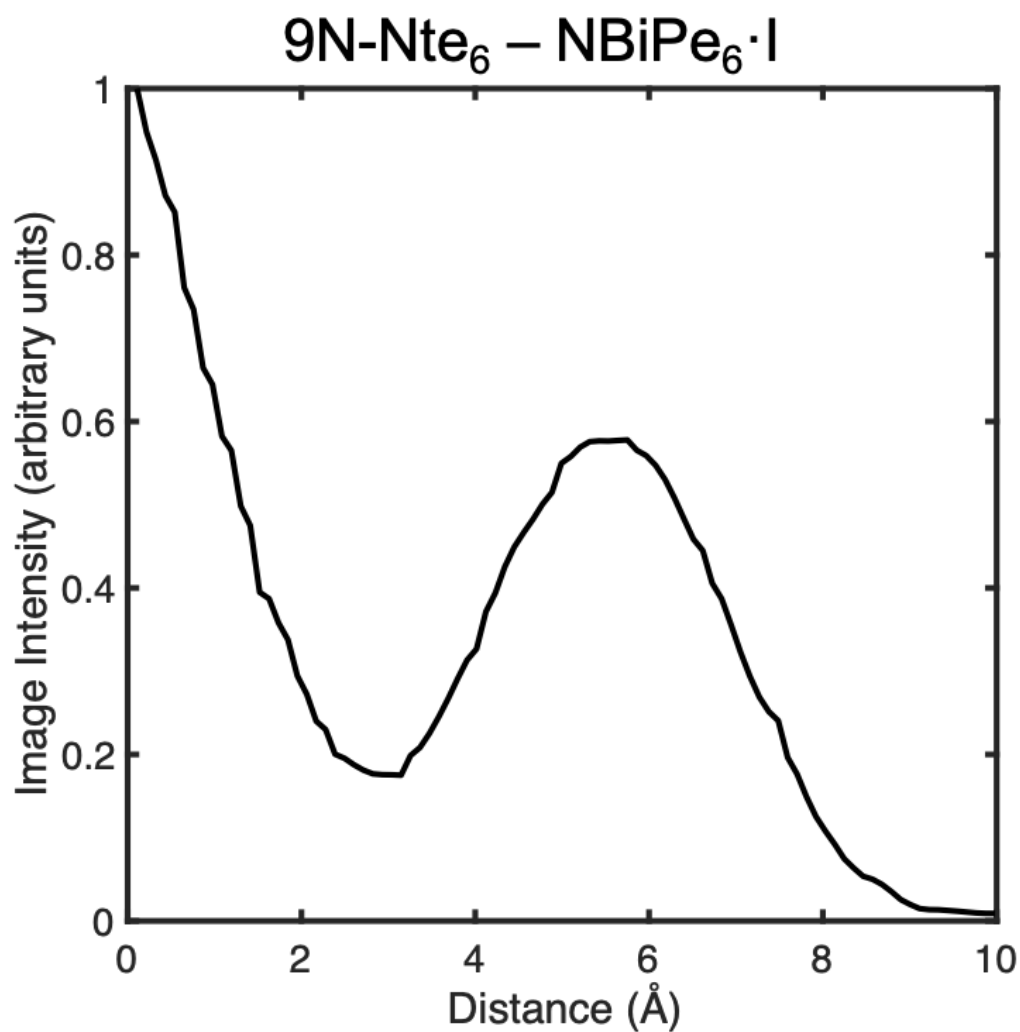
Figure 3.10: Calculated line profile of the image of the 9N-Nte$_6$-NBipe$_6$·I polypeptoid nanofibers shown in Figure 3.3(E), specifically focusing on the position of the counterion. The position of the bound amine is defined as $r=0$ and the distribution is peaked at a distance of 5.5 Å.
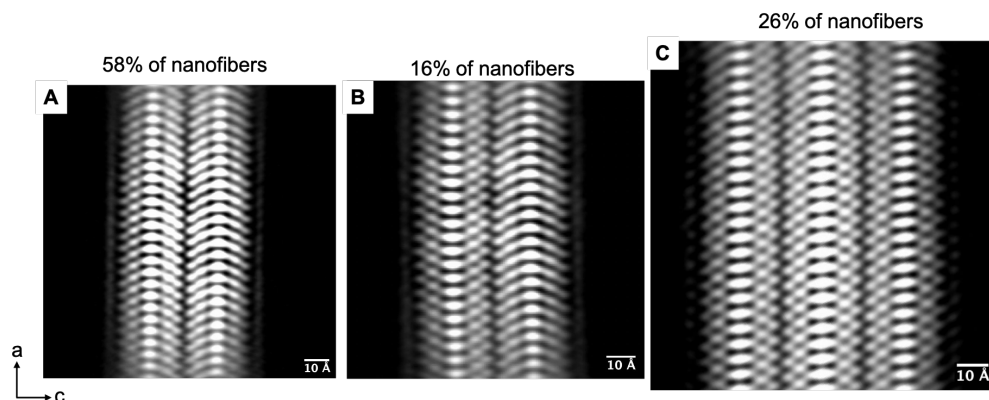
Figure 3.11: The most prevalent structure formed by the 9N-Nte$_6$-NBipe$_6$·Cl polypeptoids, shown in Panel A, is a two row fiber where the polypeptoids adopt a parallel V-shaped formation, meaning the V-shape in the two rows points the same direction. A second, less populous antiparallel V-shape structure is also seen in Panel B. Panel C shows a three row fiber structure which is also a minority of the observed structures.
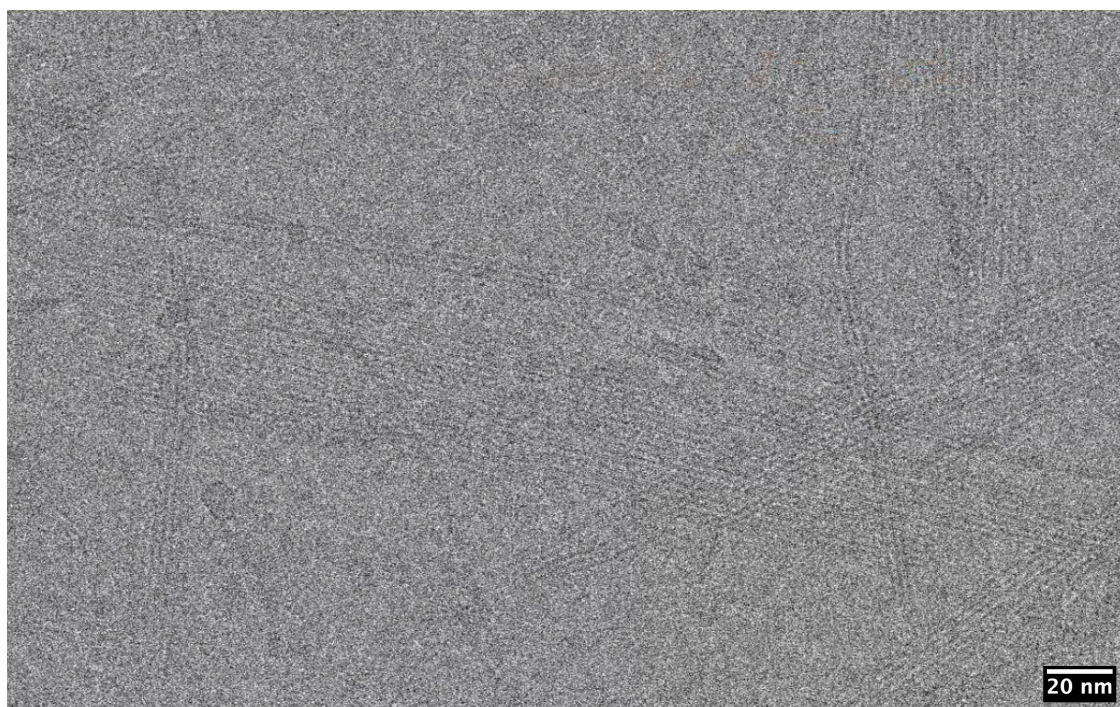
Figure 3.12: Cryo-EM micrograph of 9N-Nte$_6$-NBipe$_6$polypeptoids. Both nanosheets and nanofibers are seen in this micrograph.
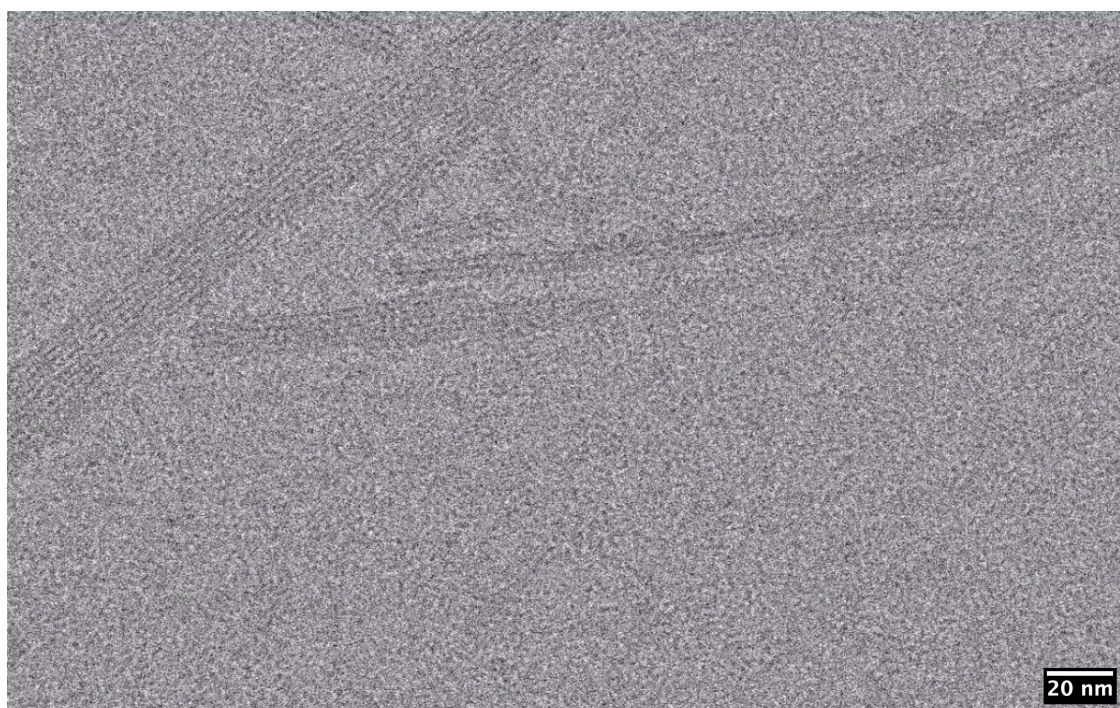
Figure 3.13: Cryo-EM micrograph of 9N-Nte$_6$-NBipe$_6$·I polypeptoids. Both nanosheets and nanofibers are seen in this micrograph.
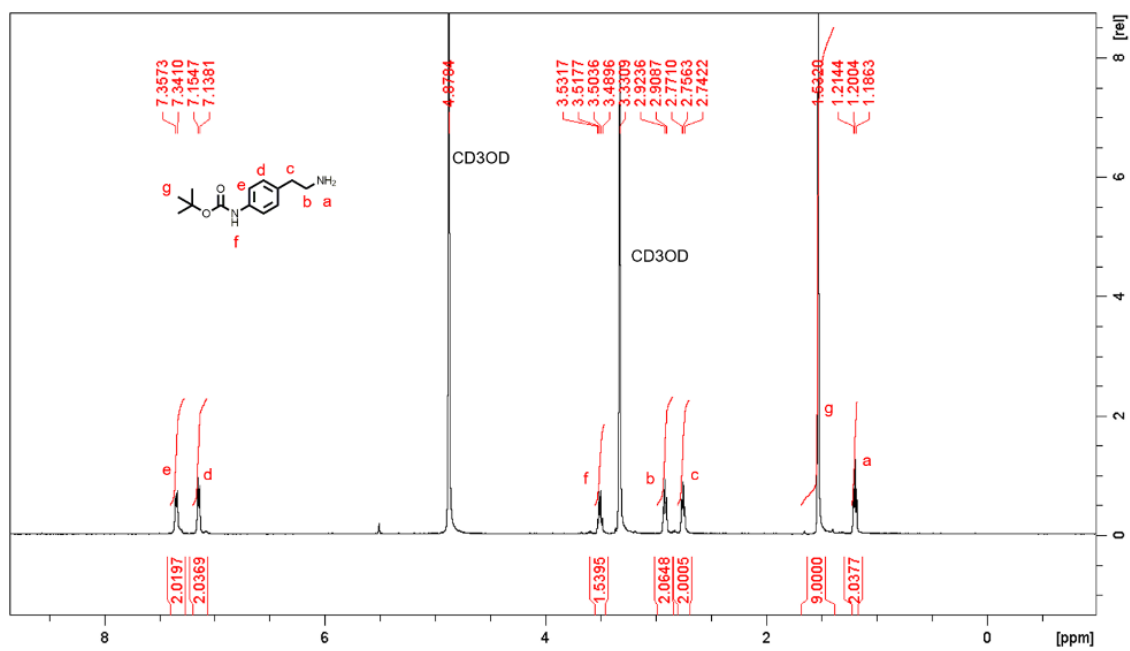
Figure 3.14: ^{1}H NMR of Boc-protected sub-monomer (Compound 1)

A   **Compound 2**
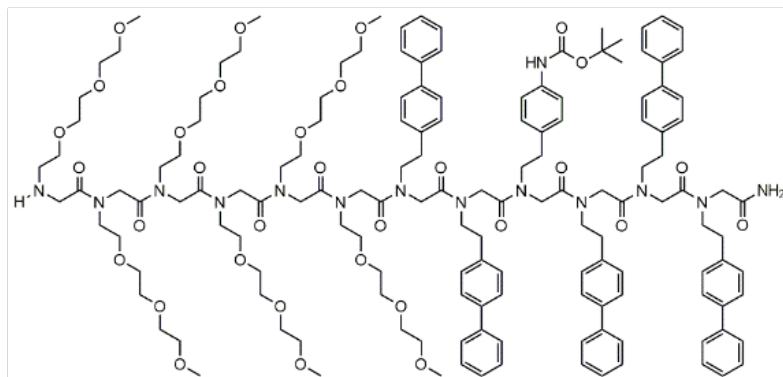
B   **Compound 3**
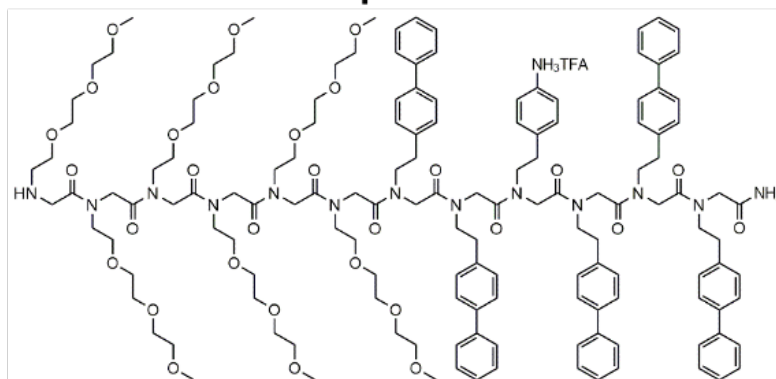
C   **Compound 4**
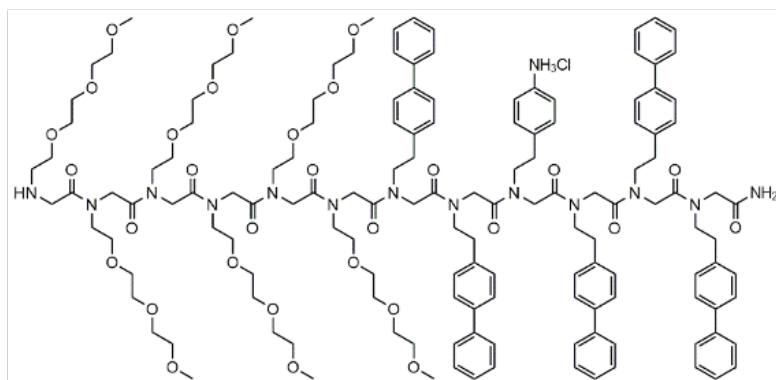
Figure 3.15: Chemical Structure of Intermediate Peptoid Products

Chapter 4

Effect of Charge Density on Polypeptoid Self-Assembly

4.1   Introduction

The de novo design of self assembled nanomaterials relies on an understanding of the relative importance of nonbonded interactions that lead to specific nanostructures [34, 115, 116]. Block copolymers in particular can form a multitude of nanostructures, with various applications from artificial membranes [31] to chemophototherapy treaments [117]. Polypeptoids, or N-substituted glycines, present a great platform to study the atomic-scale interactions that lead to different nanostructures. Polypeptoids are similar to peptides, except the variable side chain is attached to the nitrogen rather than the α-carbon [28, 30, 118]. Therefore, there are no hydrogen bond donors on the backbone of the molecule and interactions between the side chains dominate. In this study, the effect of fixed charges on the self-assembly of diblock polypeptoids is studied directly by atomic-scale cryo-transmission electron microscopy (cryo-TEM).

A series of amphiphilic diblock copolypeptoids have been synthesized that self-assemble into highly ordered nanostructures. The hydrophobic block of the polypeptoids is made up of biphenyl side chains; this block crystallizes to form the core of the self-assembled nanosheet structures. The hydrophilic block remains amorphous and extends into the solvent. Two polypeptoids are investigated in this chapter: one with all biphenyl groups in the hydrophobic block, and another where one of the biphenyls has been changed to an aniline and protonated with a strong acid. The substitution of this one functional group allows for a direct study of the effect of fixed charges on the self-assembly of polypeptoids.

4.2 Experimental

4.2.1 Polypeptoid Synthesis

The polypeptoids employed in this study are amphiphilic diblock copolypeptoids composed of a hydrophobic N-(2-(4-biphenyl)ehthyl)glycine (NBipe) segment and a hydrophilic poly-N-2-(2-(2-methoxyethoxy))ethylglycine (Nte) segment. The synthesis is the same as has been described earlier, see Section 3.2.1 for details.

To perform the self-assembly, the same procedure as described in Section 3.2.2 was used. In brief, the polypeptoids were dissolved in a mixture of THF and water (50/50 by volume). The THF was slowly evaporated at 4 °C, leaving self-assembled nanofibers in solution [27, 56].

4.2.2 Cryo-TEM imaging

The TEM imaging for the Nte_6-$NBipe_6$ and $9N$-Nte_6-$NBipe_6$·TFA polypeptoid nanosheets was done at 300 keV with a 20 eV energy filter on a Titan Krios G2. To prepare the aqueous samples for imaging, they were drop cast on a copper TEM grid with both a holey carbon film and continuous carbon film, then blotted using a Vitrobot, before being plunge frozen in liquid ethane and transferred to liquid nitrogen as is standard for preparing frozen hydrated samples [15].

The data collection and analysis is the same as has been described earlier in Section 2.2.1. An electron dose of 40 $e^-/Å^2$ was used to collect the data sets for the Nte_6-$NBipe_6$ and $9N$-Nte_6-$NBipe_6$·TFA polypeptoids. The full frame movie alignment is done with dose weighting, so later frames in the movies that have a higher accumulated electron dose affect the final image less.

4.3 Results and Discussion

4.3.1 Neutral polypeptoids

As previously mentioned in Chapter 3, diblock copolypeptoids with a hydrophilic (*N*-2-(2-(2-methoxyethoxy)ethoxy) ethylglycine) (Nte) monomer and a hydrophobic (*N*-(2-(4-biphenyl)ethyl)glycine) (NBiPe) monomer were synthesized via a solid-phase synthesis method [56]. The hydrophobic core has 6 NBiPe units and the hydrophilic block contains 6 Nte units. The chemical structure of the Nte_6-$NBipe_6$ polypeptoids is shown in Figure 4.1(A). The proposed structure of the nanosheets is akin to what has previously been described in Figures 2.1 and 3.2. The hydrophilic Nte block, shown in teal in Figure 4.1(B), is amorphous and extends into solution on the top and bottom of the nanosheets. The NBipe block, shown in yellow and white in Figure 4.1(B) crystallizes to form the core of the nanosheets. When
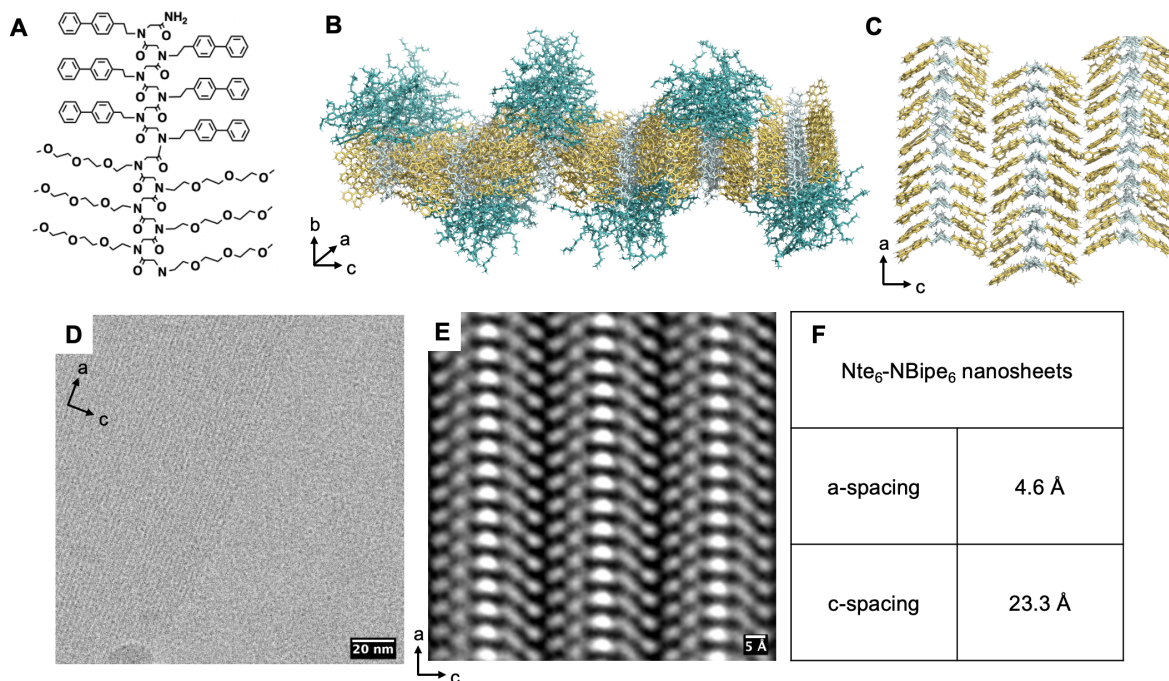
Figure 4.1: The chemical structure of the Nte_6-$NBipe_6$ polypeptoids is shown in Panel A. Panel B shows an atomic model of the nanosheets formed by the Nte_6-$NBipe_6$ polypeptoids. Panel C shows an atomic model of the projection through the a-c plane of the nanosheet. Panel D shows a cryo-TEM image of the nanosheets formed by the polypeptoids, with the a and c crystallographic directions labeled. Panel E is the averaged, high resolution TEM image of the nanosheets. Panel F includes the crystal spacings measured from the TEM image.

viewed through the projection of the a-c plane, the peptoids form a V-shaped crystal structure. The backbone is the apex of the V (shown in white in Figure 4.1(C)), while the side chains emanate out to either side (shown in yellow in Figure 4.1(C)). The Nte block is not shown in the model in Figure 4.1(C) for clarity. A high resolution image of the frozen, hydrated nanosheets is shown in Figure 4.1(D) and the a and c crystallographic directions are labeled. The averaged high resolution image of the Nte_6-$NBipe_6$ polypeptoids is shown in Figure 4.1(E). This image is the projection through the a-c plane of the nanosheet. The brightest white spot at the center of each V-shape is the projection down the end of the glycine backbone, and the biphenyl side chains extend out to either side to make up the arms of the V. The spacing between backbones in the a and c directions were measured from this image and are included in Figure 4.1(F).
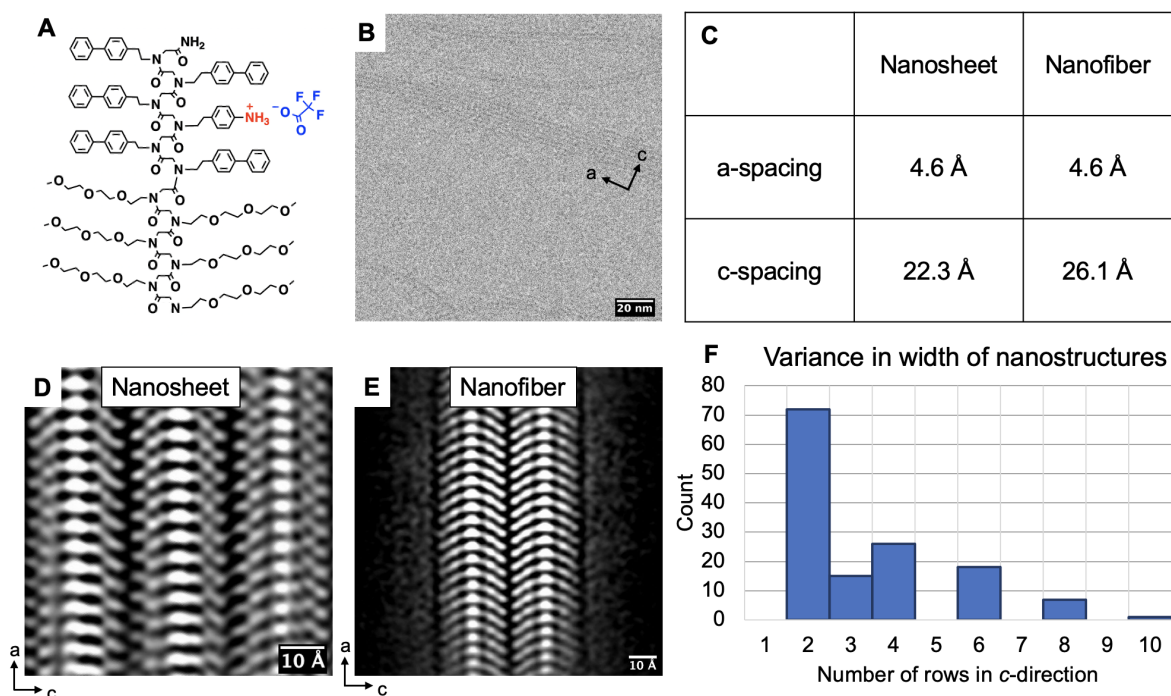
Figure 4.2: The chemical structure of the 9N-Nte$_6$-NBipe$_6$·TFA polypeptoids is shown in
Panel A. Panel B shows a cryo-TEM image of the self-assembled nanostructures, with the
a and c crystallographic directions labeled. Panel C is a table with the measured crystal
spacings from the different structures. Panel D shows the averaged high resolution TEM
image of the nanosheet structures. Panel E is the averaged image of the nanofibers. Panel
F graphs the relative abundance of the different sized nanostructures.

4.3.2   Charged polypeptoids with trifluoroacetate

To investigate the effect of added charges, a similar polypeptoid was synthesized, except one
of the biphenyl groups was replaced with an aniline and protonated with trifluoroacetic acid
(TFA). Thus, there was a fixed positive charge on the nitrogen side chain in the hydrophobic
block of the polypeptoids. This peptoid is referred to as 9N-Nte$_6$-NBipe$_6$·TFA.

Figure 4.2 contains the chemical structure, characterization data, and high resolution im-
ages of the 9N-Nte$_6$-NBipe$_6$·TFA polypeptoids. Figure 4.2(A) shows the chemical structure
with a bound positively charged amine in the hydrophobic NBipe block, an unbound nega-
tively charged TFA counterion, and the hydrophilic Nte block. Panel B of Figure 4.2 shows
a high resolution cryo-TEM image with one 6 row nanosheet and three 2 row nanofibers.
The number of rows refers to the width in the c-direction and is measured by counting the
number of dark lines, which correspond to the polypeptoid backbones. The a and c crystal-
lographic directions are labeled on the nanosheet in Figure 4.2(B). Figure 4.2(C) shows the

measured a and c spacings from the high resolution TEM images of both the nanosheets and nanofibers. The a-spacing is constant at 4.6 Å for both the nanosheet and nanofiber. However, the c-spacing increases from 22.3 Å in the nanosheet to 26.1 Å in the nanofiber. This increase in c-spacing may be due to varying angles between the side chain and backbone that results in pushing the backbones further apart in the two different nanostructures. Figure 4.2(D) shows the high resolution image of the nanosheet formed by the 9N-Nte$_6$-NBipe$_6$·TFA polypeptoids and Figure 4.2(E) shows the high resolution image of the 2 row nanofibers. The data analysis of the nanosheets was done with the same procedure as described in Section 2.2.1 whereas the analysis of the nanofibers was done using a different program, described in detail in Section 3.2.3. It was necessary to use the 2dx electron crystallography program for the analysis of the nanosheets due to its ability to identify the lattice and the position of the unit cells [63]. This functionality is not included in the Cryosparc program that was used for the analysis of the fibers [22]. However, the atomic-scale images that were reconstructed from the two different methods of data analysis still are true representations of the different nanostructures. By analyzing 162 images, the number of nanostructures with each number of rows was counted and the results are included in Figure 4.2(F). The two row nanofiber structure is the most prevalent structure, making up 52% of the observed structures.

4.3.3 S-shaped crystal structure
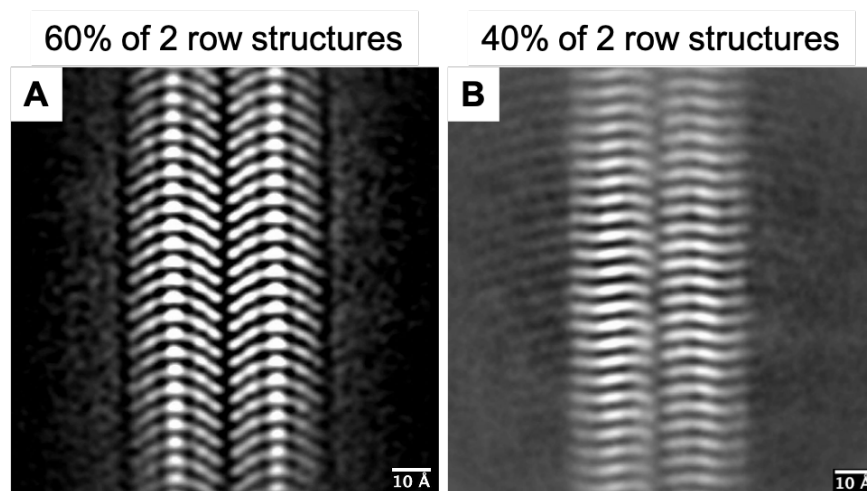
Figure 4.3: There are two distinct crystal structures present in the nanofibers formed by the 9N-Nte$_6$-NBipe$_6$·TFA polypeptoids. The V-shaped structure makes up 60% of all observed nanofibers and the structure is shown in Panel A. Panel B shows the S-shaped crystal structure which makes up 40% of the nanofibers.

Nanostructures of varying width are observed with the 9N-Nte$_6$-NBipe$_6$·TFA polypep-

toids, as detailed in Figure 4.2(F). In addition to the V-shaped crystal structures shown in that figure, a different S-shaped crystal structure has also been observed. This S-shaped structure only forms two row nanofibers; all of the nanosheets had the V-shaped crystal structure. The origins for the two different crystal structure are still under investigation. It is possible that the charged amine groups in the side chains can impact self-assembly in a way that changes some of the backbone angles, resulting in an S-shaped crystal.

4.4 Conclusions

There are a multitude of weak, nonbonded interactions that affect the self-assembly process of polymeric materials. Ionic interactions were systematically studied here, by using an uncharged peptoid as a reference then using various protonating agents to increase the presence of charged polypeptoids. Figure 4.4 illustrates the effect of the fixed charges on the resulting self-assembled nanostructures. These results indicate that covalently bonding fixed charges to polypeptoids can be used to target specific nanostructures. The Nte_6-$NBipe_6$ polypeptoids all form large nanosheet structures (see Figure 4.1). When fixed charges enter the system by protonating amine groups in the hydrophobic core, nanofibers begin to form (see Figure 4.2). It is possible that the nanofiber morphology arises because the fixed charge in the hydrophobic block selectively inhibits growth in the c-direction. When the counterion is Cl^- for the $9N$-Nte_6-$NBipe_6$·Cl, nearly all of the covalently bound amine groups carry a positive charge and therefore nearly all of the polypeptoids are on the edges of nanostructures, either in two or three row nanofibers (see Figure 3.11). Finally, when the counterion is TFA, which has a higher pKa than Cl^-, nanofibers still are the majority structure, indicating that a high proportion of the bound amine groups are positively charged, but nanosheets are also observed. Therefore, to target nanosheets, uncharged polypeptoids must be used but nanofibers can be selectively made by increasing the charge density to block growth in one direction.

4.5 Acknowledgements

Figure 4.4: Nte$_6$-NBipe$_6$ without an ionic charge always assembles into large nanosheets, as shown on the left. 9N-Nte$_6$-NBipe$_6$·Cl polypeptoids have a charged amine on nearly every peptoid molecule, due to the extremely low pKa of Cl$^-$, and form only nanofibers (the right side). When the 9N-Nte$_6$-NBipe$_6$·TFA system uses TFA as the protonating agent, which has pKa is much higher much higher than Cl$^-$, fewer of the amine groups in the polypeptoids are positively charged. This results in a mixture of nanofibers and nanosheets, as shown in the middle.

4.6 Supplementary Information
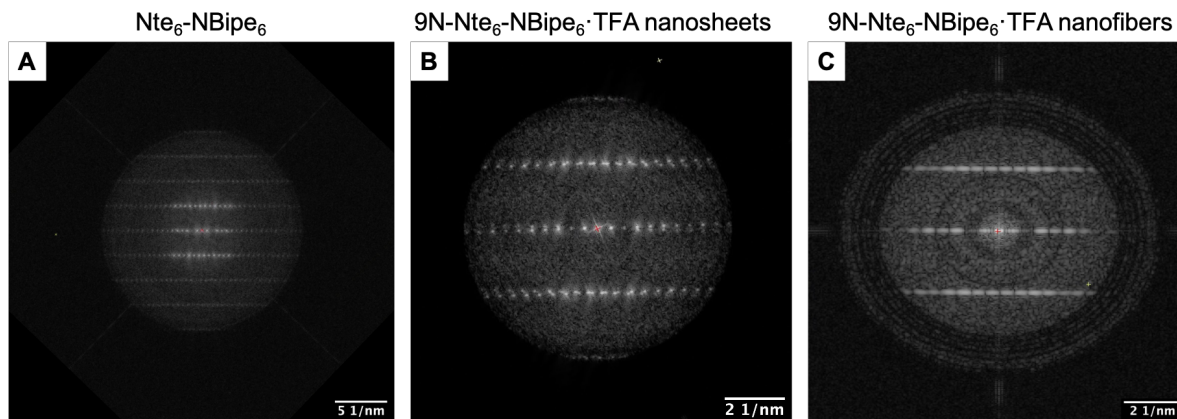
Figure 4.5: Panel A shows the FFT of the image of the Nte_6-$NBipe_6$ nanosheets in Figure 4.1(E). Panel B shows the FFT of the image of the $9N$-Nte_6-$NBipe_6 \cdot TFA$ nanosheets in Figure 4.2(D) and panel C is that for the nanofibers in Figure 4.2(E).

Chapter 5

Imaging Polystyrene-b-Polyethylene Oxide Single Crystals

5.1 Introduction

Polymer electrolytes have been investigated thoroughly for applications in lithium batteries due to their chemical stability against lithium metal and inflammability [119–121]. Poly(ethylene oxide) (PEO) has good ion transport properties and is effective as an electrolyte for lithium batteries [38, 42, 122]. Polystyrene has exceptional mechanical properties and has been shown to effectively inhibit lithium dendrite growth in a lithium symmetric cell [40, 123]. When these two polymers are combined to make a diblock copolymer (PEO-b-PS or SEO), they can be used as both an electrolyte and separator for lithium batteries [36, 39].

The local solvation environment of lithium ions has a significant impact on the transport properties like conductivity, current fraction, and transference number [43, 124, 125]. Neutron scattering has been used previously to glean information about the solvation structure and dynamics in a polymer electrolyte [126]. This work illustrates the necessity for further studies to uncover the relationships between structure at the atomic scale and macroscale transport properties in order to intelligently engineer polymer electrolytes for lithium battery applications.

Pioneering work by Bernard Lotz in the 1960s studied the crystallization of SEO into single crystals [127]. He used electron microscopy to study the morphology and crystal structure of the self-assembled single crystals and showed that the crystal structures matches that of pure PEO. His work agreed with the proposed "sandwich" structure of the single crystals, where the PEO block crystallizes in the middle of the crystal and is "protected" by amorphous PS domains on the top and bottom [127, 128]. Figure 5.1(B) shows a cartoon of this structure, with the crystalline PEO shown in red and the amorphous PS in blue. Additional work by Stephen Cheng [128–130] and Christopher Li [122] have studied the structure of these crystals with TEM, XRD, and AFM. The images produced have elucidated the structure of these crystals at a micron level scale and atomic resolution information has
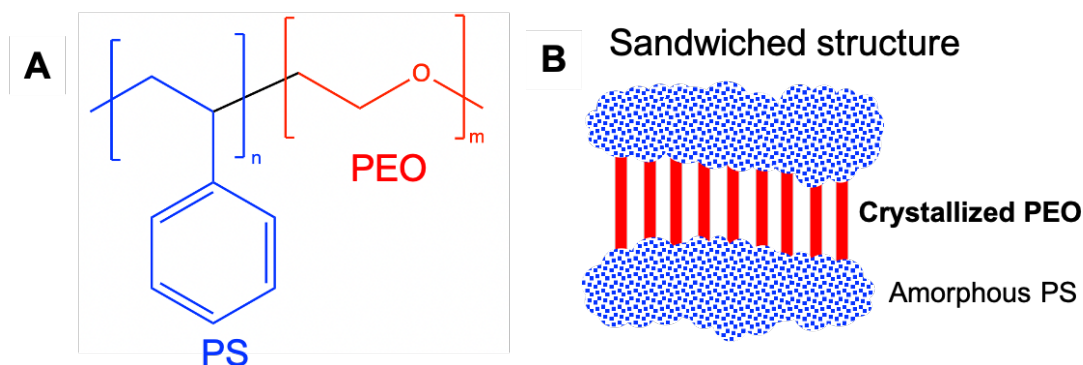
Figure 5.1: Panel A shows the chemical structure of PS-b-PEO. Panel B shows the proposed
"sandwiched" structure of the single crystals, where the PEO crystallizes in the middle of
the crystal and the PS block remains amorphous on the top and bottom.

been gleaned from electron diffraction wide-angle X-ray scattering. However, there is still
a need to study these crystals in high resolution via imaging to get all of the structural
information in position space.

5.2   Experimental

5.2.1   Crystallization

Polystyrene-b-polyethylene oxide (PS-b-PEO) (SEO) block copolymers were previously syn-
thesized via anionic polymerization described in Reference [131]. A block copolymer with
molecular weight of the polystyrene block M_{PS} = 5.1 kg mol^{-1} and polyethylene oxide
block M_{PEO} = 12.8 kg mol^{-1} was chosen for this study. The SEO block copolymer was
dissolved in amyl acetate at a concentration of 0.01 wt % [122] (Note: a 1:1 (vol %) co-
solvent mixture of chlorobenzene and octane can also be used, but chlorobenzene is not
glovebox compatible [128]. Therefore, amyl acetate solvent was used for this study). Neat
crystals (SEO without any lithium salt) as well as crystals with various amounts of lithium
bis(trifluoromethanesulfonyl)imide (LiTFSI) were studied. The salt concentration is ex-
pressed as $r = \frac{[Li^+]}{[EO]}$ where EO = ethylene oxide units in the PEO block. In this study, SEO
polymers with r values between 0.05 and 0.15 were studied. To produce micron-sized, thin
single crystals of the SEO polymers, a self-seeding technique was utilized [127, 128]. First,
the SEO and any LiTFSI was dissolved in amyl acetate by heating to 50 °C and stirring
for two hours (or longer if it was not a homogeneous solution after 2 hours). Then, the
solution was allowed to cool to 25 °C and held there for 48 hours. Next, the solution was
slowly heated up (0.5 °C / min) to 41 °C and held there for 20 minutes. Finally, the polymer

solution was cooled to 25 °C, held there for 48 hours, then transferred to an argon-filled glovebox for storage.

5.2.2   TEM imaging

Polyethylene oxide will absorb water and lose its crystal structure after being exposed to the atmosphere for extended amounts of time. The polystyrene block aids in preventing water absorption and protecting the crystal structure, so the neat SEO single crystals can be handled outside of a glovebox and retain their crystallinity for periods of time (≈ 4 hours) [127]. However, LiTFSI is extremely hydrophilic and will absorb water almost immediately upon exposure to the atmosphere. Therefore, the SEO crystals with LiTFSI were prepared in an argon glovebox and the dilute solution was dropcast on C-Flat TEM grids (Electron Microscopy Sciences) and dried in the glovebox. The dry TEM grids were then sealed between Kapton sheets in a standard holder for small-angle X-ray scattering (SAXS) and removed from the glovebox. Once outside the glovebox, the SAXS holders with the TEM grids inside of them were plunged in a bath of liquid nitrogen. The SAXS holders were opened under liquid nitrogen, the TEM grids were removed and then transferred to standard TEM grid holders. In this way, the SEO crystals could be taken out of a glovebox and stored in liquid nitrogen with zero exposure to the atmosphere.

The low magnification TEM images were taken under cryogenic conditions at 120 keV on a JEOL1400 TEM. The high magnification TEM imaging was done at 300 keV with a 20 eV energy filter on a Titan Krios G2 (FEI company).

The frozen grids were transferred to the Krios TEM and a low-dose imaging procedure was employed [21]. The accumulated electron dose was set to 40 e$^-$/Å^2 and about 3,000 dose fractionated movies were recorded using a Gatan K2 direct electron detector. The movies were recorded in super resolution mode (0.5 binning) and the pixel size was 0.2826 Å/pixel. The defocus range used was -0.5 to -1.5 µm.

5.2.3   Low-dose TEM image analysis

Descriptions of the data analysis for electron crystallography of low-dose images has been described earlier in Section 2.2.1. The same general procedure of movie alignment, CTF correction, and lattice identification and unbending was employed to produce the high resolution images here. However, rather than classifying and averaging unit cells from multiple different images, the high resolution images presented in this chapter come from one single raw image. The main difference in the processing is that the high resolution images in this chapter are produced by indexing all of the reflections present in the FFT of a single image, determining the phase and amplitude of the reflections, then calculating the inverse FFT based on those reflections to present a final, high resolution image [63].

5.2.4 Image Simulation

The mathematics of electron-atom interactions at the atomic scale are well known, and thus these mathematical relations can be used to calculate simulated TEM images from a known crystal structure [132–134]. AbTEM is a Python package that has the functionality to create simulated TEM images from an input structure [135]. An in-house code was written to simulate the effect of defocus, aberrations, and the envelope function.

5.3 Results and Discussion

5.3.1 SEO Single Crystals without Lithium Salt
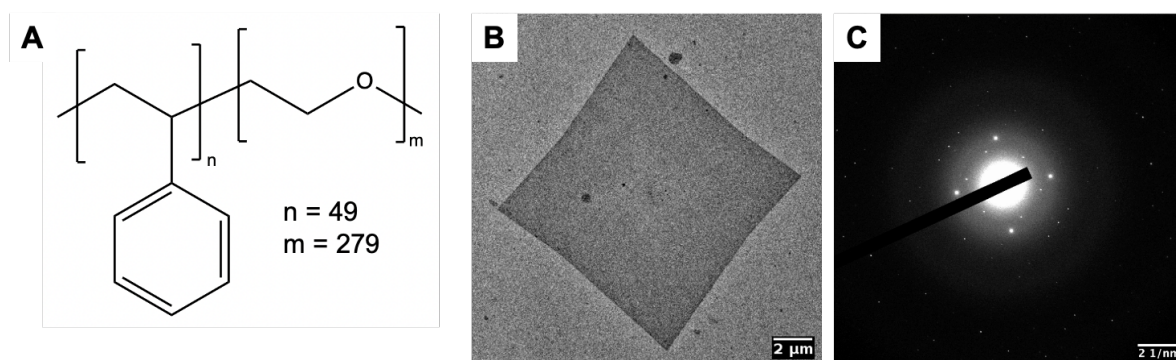
Figure 5.2: The structure of polystyrene-*b*-polyethylene oxide (PS-*b*-PEO) (SEO) is shown in panel A. For the polymer used in this study $n = 49$ and $m = 279$. Panel B shows a TEM image of the SEO single crystal with the diffraction pattern shown next to it in panel C. The 120 diffraction spots are the brightest, square-shaped spots.

After the self-seeding crystallization, the SEO crystals are free-floating in the amyl acetate solvent. For the neat SEO, they were drop cast in a fume hood on a standard TEM grid with a carbon support film and transferred to a JEOL 1400 TEM. The imaging and diffraction were done at cryogenic conditions. As seen in Figure 5.2(B), the resulting crystals adopt a square-shaped morphology with an approximate length and width of 10 μm. The thickness of these crystals were not measured directly in this study, but based on previous studies of SEO single crystals produced in this method, we assume the crystals are about 20 nm thick [128]. The electron diffraction pattern in Figure 5.2(C) shows how extremely well-ordered this crystals are; there are diffraction spots visible out to a spatial frequency of 1.2 Å, which is very small and unique for polymer crystals. An important note is that this diffraction pattern exactly matches the diffraction pattern from bulk PEO that was measured from X-ray diffraction [133]. The brightest spots in a square formation are the (120) diffraction

spots. These spots occur at a *d*-spacing of 4.6 Å, which is exactly the same *d*-spacing as bulk PEO. This confirms that the PEO block in these samples matches the expected crystal structure from a bulk sample and the amorphous PS block does not impact the crystal structure or show up in the diffraction pattern.

5.3.2 SEO Single Crystals with Lithium Salt

Next, a small amount of LiTFSI was added into the self-seeding solution. The resulting crystals also adopt a square morphology (Figure 5.3(B)) and are highly ordered, as seen in the diffraction pattern in Figure5.3(C). However, a significant difference happens in these crystals, as the (120) spots now occur at a *d*-spacing of 5.4 Å rather than 4.6 Å in the neat sample. This indicates that the LiTFSI is inside of the crystal and has some effect at increasing the *d*-spacing between PEO coils. Single crystals of SEO with LiTFSI were previously made by Cheng, et al [122]. However, in their experimental procedure the LiTFSI was confined to the amorphous domain; in order to use the averaging-based TEM techniques described here, the LiTFSI must be in the crystalline domain. Therefore, a new experimental procedure was developed to produce single crystals with the LiTFSI in incorporated in the crystalline PEO and this procedure was described in Section 5.2.1.

Figure 5.3: The structure of SEO and LiTFSI are shown in panel A. The same SEO diblock copolymer is used for this whole study. This figure shows images from a crystal with a nominal salt concentration of r = 0.05. Panel B shows a TEM image of the SEO single crystal with LiTFSI and the diffraction pattern of this crystal is shown next to it in panel C. The 120 diffraction spots are the bright spots arranged in a square near the center of the image.

The amount of LiTFSI salt that was added to the self-seeding solution was increased to r = 0.15. Large, square-shaped crystals were again produced by repeating the self-seeding procedure (see Figure5.4(B)). The cryo-electron diffraction pattern of these crystals again

indicates that they are very highly-ordered. The spacing between the (120) spots in this
pattern has increased to 5.9 Å (compared to 4.6 Å in the neat crystals), indicating that
more LiTFSI has been incorporated in the crystal structure and is pushing the PEO coils
further apart.

Figure 5.4: The structure of SEO and LiTFSI are shown in panel A. The same SEO diblock
copolymer is used for this whole study. This figure shows images from a crystal with a
nominal salt concentration of r = 0.15. Panel B shows a TEM image of the SEO single
crystal with LiTFSI and the diffraction pattern of this crystal is shown next to it in panel C.
Similar to the other structures, the 120 diffraction spots are the brightest ones in a square
shape near the center of the image.

High-resolution TEM imaging was carried out on the crystals with no LiTFSI (neat), a
small amount of LiTFSI (r = 0.05), and a large amount of LiTFSI (r = 0.15). All samples
were imaged at cryogenic conditions on a Titan Krios G2 at 300 kV. The data was collected
as multiframe movies, which were first aligned into single frame images using Cryosparc [22].
These images were then loaded into 2dx, an electron crystallography software [63]. FFTs
(Fast Fourier Transforms) of each image were calculated and the lattice was determined by
indexing the reflections present in each FFT. Then, the images were CTF-corrected and an
unbending procedure was implemented to correct for distortions in the lattice. After these
corrections, the lattice was finalized and an electron density map was created based on the
reflections present in the FFT. The electron density maps of the neat sample (5.5(A)), that
with r = 0.05 (5.5(B)), and that with r = 0.15 (5.5(C)) are shown below in Figure 5.5.
    The primary feature in the neat crystal shown in Figure 5.5(A) is a grid of circles. Based
on the known crystal structure of PEO, these circles are the projection down the end view
of the PEO chain. The crystal with a small amount of LiTFSI, displayed in Figure 5.5(B),
shows a grid of star shapes instead of circles. There is not an existing crystal structure, to my
knowledge, of PEO crystallized with a small amount of LiTFSI. To my best approximation,
the origin of these star shapes is similar to that of the circles in Figure 5.5(A); the difference

is that the TFSI is situated between the PEO helices and shows up as the points of the star. However, further work is needed to better characterize the structure in this image. The primary features in the image with a large amount of LiTFSI in Figure 5.5(C) is a repeating pattern of X's and O's. This pattern is much more complicated than the other two structures, and the next section details work with image simulation to try to understand the features in this image better.
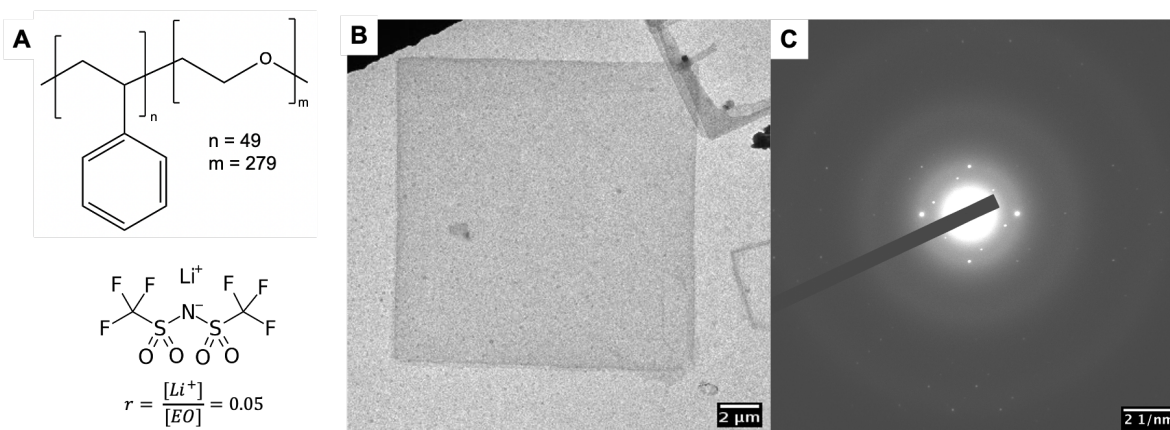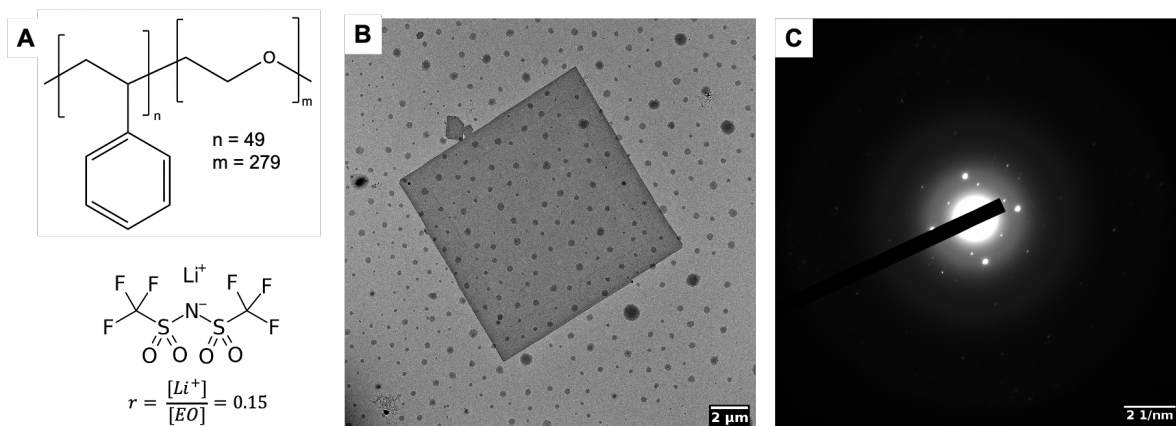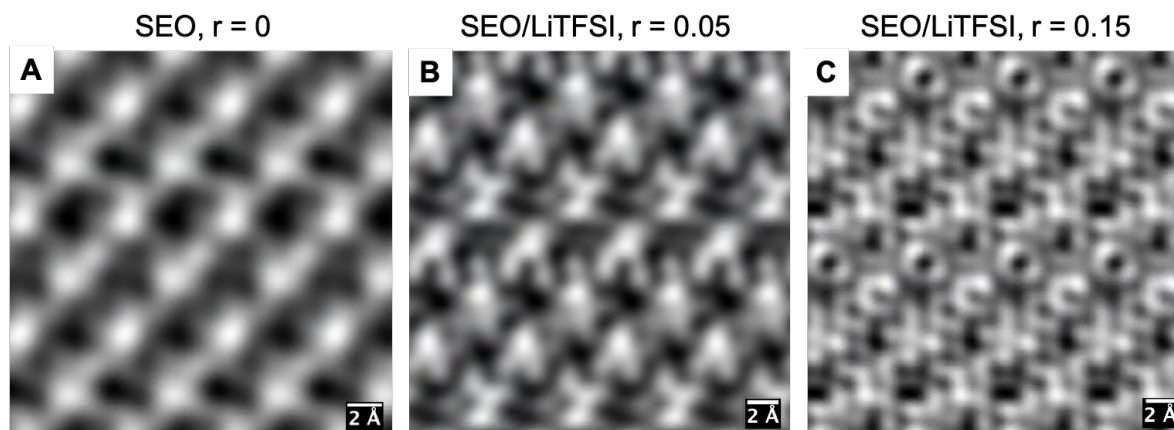

Figure 5.5: The structure of SEO and LiTFSI are shown in panel A. The same SEO diblock copolymer is used for this whole study. This figure shows images from a crystal with a nominal salt concentration of r = 0.15. Panel B shows a TEM image of the SEO single crystal with LiTFSI and the diffraction pattern of this crystal is shown next to it in panel C.

5.3.3 Simulated TEM images of PEO with and without lithium salt

The crystal structure of bulk PEO has been determined previously from X-ray scattering by Takahashi and coworkers [133]. Even though these measurements were done on bulk PEO, the crystal structure of the SEO single crystals prepared here is identical to the bulk crystal structure, as determined via cryo-electron diffraction (see Figure 5.2(C)) [127, 128]. AbTEM was used to create simulated images from this crystal structure [133, 135]. First, the crystal structure from Takahashi, et al. was loaded into AbTEM and rotated into plane that matches the orientation of the experimental image. Then, the electrostatic potential of the sample is calculated by using an independent atomic model to separately calculate the electrostatic potential of each atom and add them together. The electrostatic potential is only calculated from the electron-atom interactions; therefore, in order to create true simulated images the aberrations from the TEM must be included. An in-house code was

written to model the effect of defocus and the envelope function within the image. The result of this code is images that are defocused, CTF-corrected, and low pass filtered to cut off high spatial frequency information. Panel B in Figure 5.6 shows the final results of this image simulation procedure.
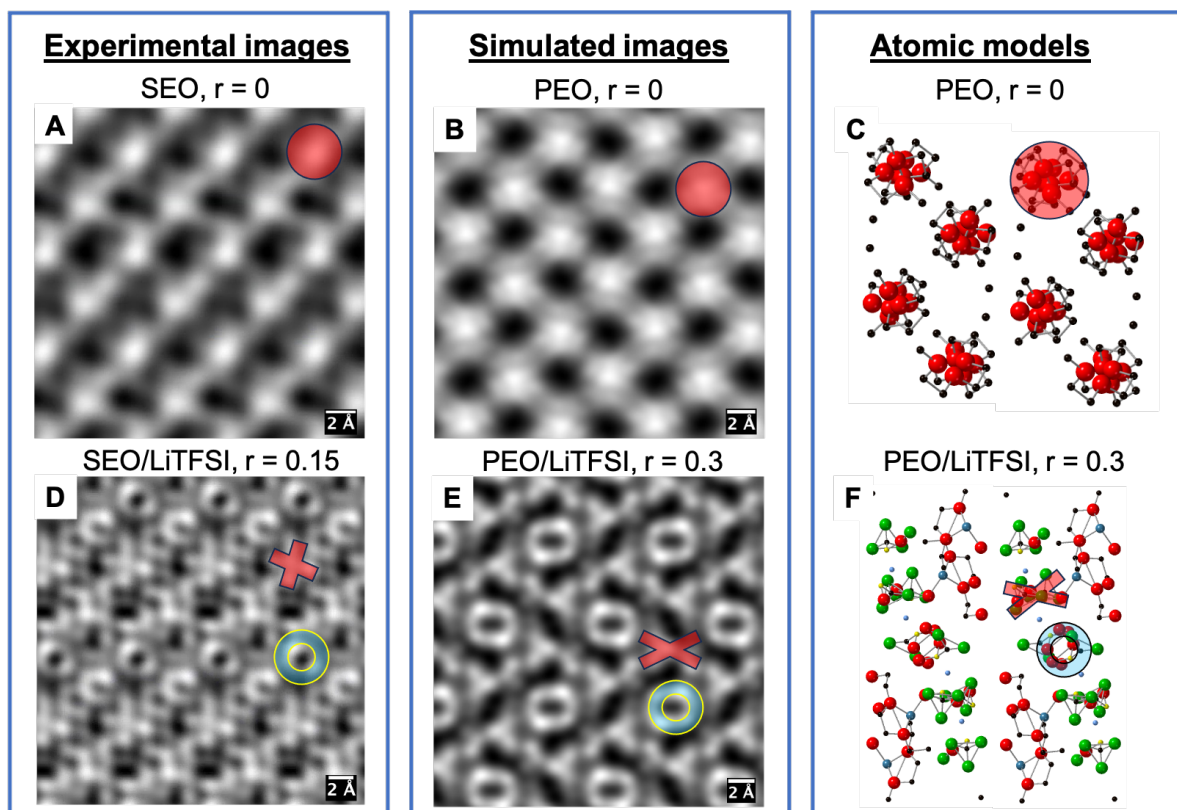
Figure 5.6: The experimental high resolution TEM image of the neat (i.e. no lithium salt) SEO crystal is shown in Panel A (note: this is the same image shown in Figure 5.5 (A)). The simulated image from the crystal structure of PEO, as determined by Takahashi and coworkers [133], is shown in Panel B. The direct atomic model of this crystal structure is shown in Panel C. A red circle is overlaid in Panels A, B, and C, to illustrate the similar circular feature in the model, simulated image, and experimental image. The experimental high resolution TEM image of the SEO single crystal with LiTFSI at a concentration of r = 0.15 is shown in Panel D (likewise, this is the same image from Figure 5.5(C)). The simulated image from the crystal structure of PEO with LiTFSI at a concentration of salt of r = 0.33, as determined by Andreev and coworkers [134], is shown in Panel E. Panel F shows the atomic model of this structure. A blue O and red X are overlaid in Panels D, E, and F to signify the similar features.

In the known crystal structure of PEO, the individual PEO chains adopt a helical struc-

ture and each helix is arranged in a parallelogram shape. In the experimental image, the direction of imaging is down the end of the helix. The atomic model in Figure 5.6(C) is rotated to show the end view of the helices and match the orientation of the experimental image. In this plane, the main feature is a circular shape of the PEO chain arranged in a grid pattern. In Panel C of Figure 5.6, a red circle is overlaid on top of one of the chains to indicate the circular feature. A similar circular feature is seen in both the experimental and simulated images in Panels A and B of Figure 5.6. It is quite remarkable how well the experimental and simulated images agree.

A similar procedure was used to create simulated images of PEO with LiTFSI. The structure of bulk PEO crystals with LiTFSI at a concentration of r = 0.33 has been determined previously by X-ray scattering by Andreev and coworkers [134]. After a thorough literature search, this is the only study that I could find that fully determined the crystal structure of PEO with LiTFSI and provided atomic coordinates. Therefore, since this is the best known structure available for image simulation, it is reasonable to assume that it will not match perfectly with the experimental image due to the significant difference in salt concentration. However, image simulation can still provide clues to understand the contrast and features seen in the experimental image. One notable feature in the experimental image of SEO/LiTFSI at r = 0.15, shown in Figure 5.6(D), is a repeating pattern of X's and O's. In the simulated image from the bulk structure of PEO/LiTFSI at r = 0.33, X's and O's can again be seen (refer to Figure 5.6(E)). The atomic model of this structure, shown in Figure 5.6(F), provides greater insights into the origin of these features. In this atomic model, the O formation comes from two TFSI molecules stacked on top of each other that each adopt a semicircular formation, highlighted by the blue circle in Figure 5.6(F). The X shape can be attributed to a TFSI molecule interacting with a PEO chain, and is highlighted by the red X in Panels D, E, and F, of Figure 5.6. Although the agreement between the experimental image and simulated one is worse than that for the neat sample, this exercise provides some insights into the structure and features that are seen in the experimental image of the SEO with LiTFSI.

5.3.4 4D-STEM

To confirm the crystals produced were true single crystals, 4D-STEM (i.e. scanning nanodiffraction) was used. In 4D-STEM, a converted probe is scanned over a region of real space and a diffraction pattern is recorded at each probe position [136]. Each diffraction pattern is then a 2D image, thus the name 4D-STEM comes from the dimensions of the raw dataset: a 2D array of images within a 2D array of probe positions. One of the original goals of this project was to use high resolution 4D-STEM with reconstruction techniques like ptychography, center of mass imaging, or differential phase contrast to investigate how the information from 4D-STEM techniques would differ from the information in phase contrast bright field imaging [137–140]. However, one of the well known problems with using a converged electron probe is that an extremely clean sample is required because the converged probe encourages hydrocarbon contamination and buildup - a problem that is inconsequen-

tial for bright field imaging with a large, parallel beam[141]. In this study, I was never able to come up with a method for sample preparation that eliminated hydrocarbon buildup, as many of the conventional methods of cleaning the sample (heating, plasma cleaning, and beam showering) would destroy the fragile polymer crystals. Thus, low magnification 4D-STEM was used to scan over the whole area of the crystal, rather than trying to obtain high resolution information from a small area. In the low magnification scans, the beam is spread over a larger area in real space, therefore minimizing the hydrocarbon contamination that occurs from a very concentrated beam. The dataset that is acquired from 4D-STEM has an enormous amount of information in it. Since there is a diffraction pattern recorded at every probe position in real space, so called "virtual images" can be calculated out of the diffraction data. In this calculation, a virtual detector is defined by a region in reciprocal space that mimics the area of a bright field detector, annual dark field (ADF) detector, or even separating individual diffraction spots. A 4D-STEM dataset was collected on the neat SEO crystals at room temperature. Figure 5.7(A) shows the mean diffraction pattern that was calculated by averaging all of the diffraction patterns together. The red circle in this figure illustrates the virtual ADF detector that was used to calculate the virtual image in Figure 5.7(B).
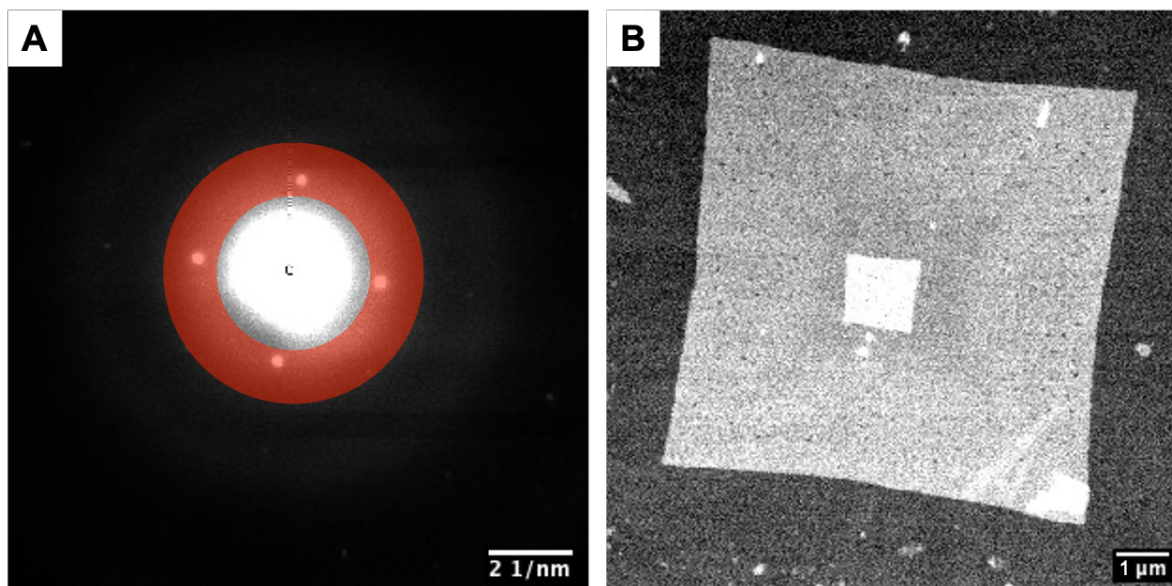
Figure 5.7: Panel A shows the mean diffraction pattern calculated from all of the scan positions in the 4D-STEM data collected from the neat SEO crystals. The red circle illustrates the position of the virtual ADF detector. The image that is calculated from this virtual detector is shown in panel B.

In further analysis of the 4D-STEM data of the neat SEO crystals, virtual detectors were placed around the pairs of 120 diffraction spots. Panel A of Figure 5.8 shows the same mean
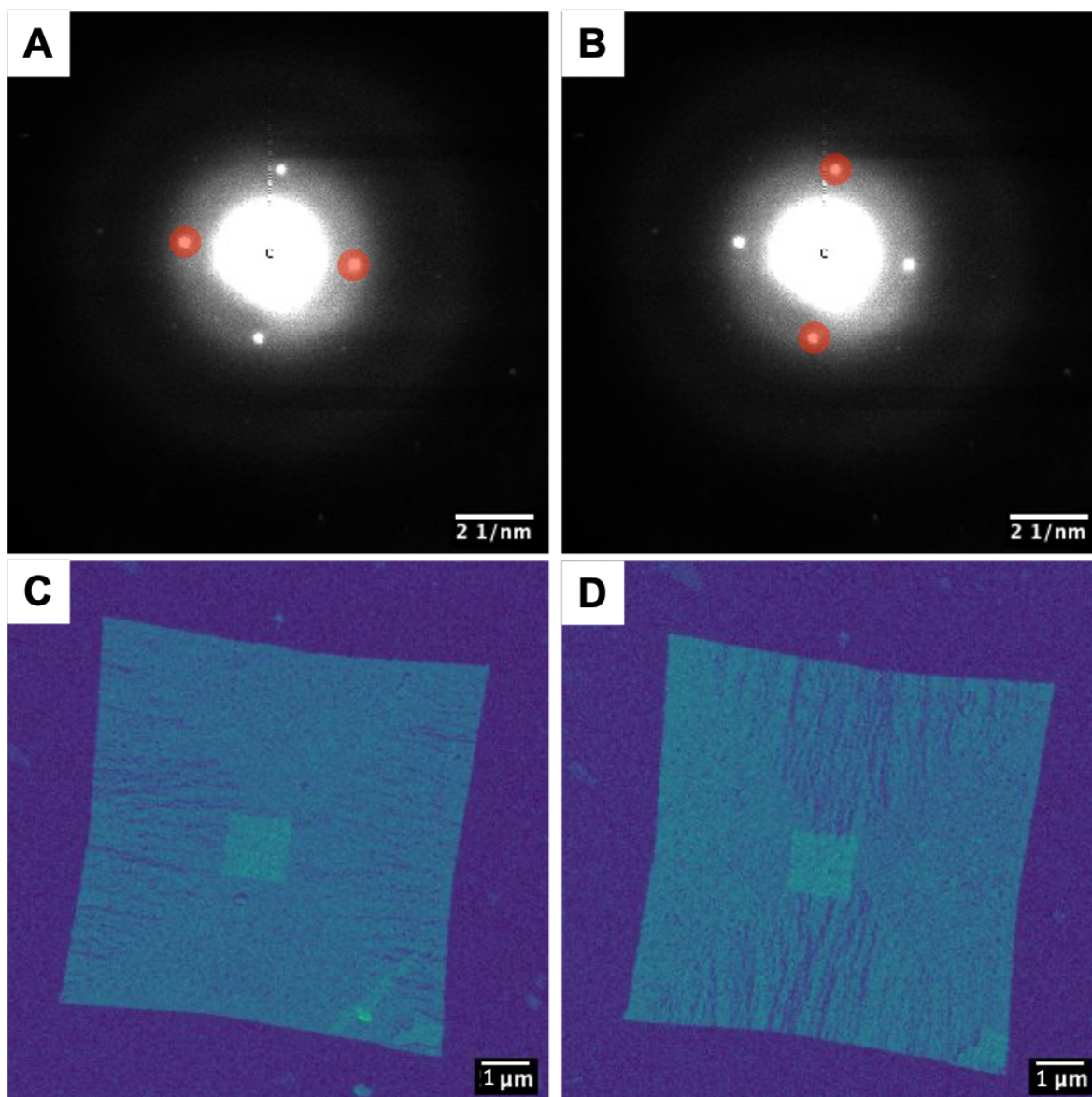
Figure 5.8: Panel A shows the mean diffraction pattern calculated from all of the scan positions in the 4D-STEM data. The two red circles illustrates the position of the virtual detector, and the calculated image is shown in panel C. In panel B, the virtual detector has been moved to the other pair of diffraction spots, and the calculated image through these spots is shown in panel D.

diffraction pattern from Figure 5.7(A) except the virtual detector has been changed to only include the intensity from the indicated pair of 120 spots. The image that is calculated

by this virtual detector is shown in Figure 5.8(C). Likewise, virtual detectors were used to image through the other pair of spots (Figure 5.8(B)) and the calculated image is shown below in Figure 5.8(D). These virtual images in Figure 5.8(C) and (D) show sectorization and crinkling within the single crystal. These phenomena have been observed before by Lotz and coworkers [127], but this is the first time that 4D-STEM has been used to obtain this kind of information.

5.4 Conclusions

The relationships between the polymer chain structure, the local environment of lithium salts, and the macroscale transport properties are important to understand in order to engineer better polymer electrolytes [122, 142, 143]. In this chapter, cryo-TEM was used to produce atomic-scale images of crystalline PEO domains within a single crystal of an SEO diblock copolymer. A new experimental method was developed to incorporate LiTFSI salt into the PEO and still form a crystalline structure. The single crystals with and without lithium salt were imaged using high resolution cryo-TEM to see how the polymer chain and crystal structure change across a range of salt concentrations. The crystal structure of pure PEO has been determined via X-ray scattering and the structure matches that in the single crystals [128, 133]. The structure of PEO with LiTFSI has also been determined previously by X-ray scattering, but only one single salt concentration was reported on [134]. TEM image simulation was used to compare the experimental image to simulated images of the known crystal structures. Further investigations, perhaps using molecular dynamics simulations or X-ray scattering, are needed to more precisely understand the crystal structures shown in the high resolution images. Yet this work still is a valuable first step in developing techniques that are capable of producing direct images of polymer electrolytes with lithium salt at atomic resolution.

5.5 Acknowledgements

5.6   Supplementary Information
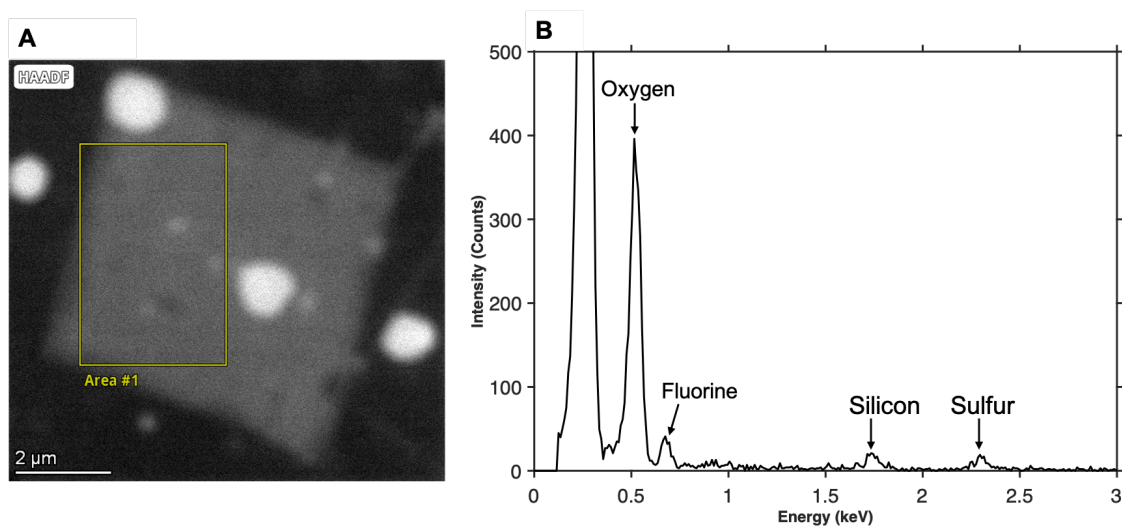
Figure 5.9: Panel A shows the HAADF-STEM image an SEO single crystal with LiTFSI at r = 0.15. The yellow square highlights the region from which EDS was calculated. Panel B shows the EDS spectra. The presence of fluorine and sulfur confirms the incorporation of LiTFSI in the SEO crystal.

Chapter 6

Conclusions

In order to intelligently design materials, a thorough understanding of how the material's structure correlates to its properties is necessary. In polymeric materials, scattering techniques are often used to gain information about the material structure. However, scattering techniques average through the bulk of a material and produce information in reciprocal space, so there may be ambiguities at times to translate that information to position space. Cryo-TEM presents an interesting opportunity to produce direct, atomic-scale images of soft materials, yet it is rarely applied to synthetic polymers due to their inherent disorder and radiation sensitivity. In this dissertation, a variety of synthetic polymers are imaged with atomic resolution by cryo-TEM. This ability to directly determine the atomic structure of synthetic polymers is vital to advancing polymer science and rationally designing functional polymer materials.

In Chapter 2, my coworkers and I synthesized a series of polypeptoids with different halogen substitutents and imaged them in high resolution. By combining the atomic-scale images with atomic-scale molecular dynamics simulations, we concluded that the covalently bonded halogen atoms in the polypeptoids interacted with each other via halogen bonds to change the crystal motifs at the atomic level.

In Chapters 3 and 4, we studied the effect of fixed charges on the self-assembly of the polypeptoids. We synthesized polypeptoids with a bound amine and protonated it with two different strong acids. These polypeptoids self-assembled into either nanofibers or nanosheets depending on the relative abundance of bound positive charges. Additionally, the unbound negatively charged counterions were imaged in atomic resolution and these results are discussed in detail in Chapter 3. The images in Chapter 3 are the first ever images of mobile counterions next to a synthetic polymer and represent a significant advancement in the study of counterion condensation.

Chapter 5 applies the same cryo-TEM techniques to a more conventional polymer in poly(ethylene oxide)-b-polystyrene (SEO). Highly ordered single crystals of SEO were produced with and without a lithium salt. The lithium salt was successfully incorporated into the crystalline PEO domain while still maintaining a high degree of crystallinity. Atomic-scale images were produced of the single crystals to investigate the effect of varying amounts

of lithium salt on the structure of the polymer. The ability to study functional polymers with direct, atomic-scale images is essential to the rational design and engineering of polymers with targeted properties.

Bibliography

1. Williams, D. B. & Carter, C. B. *Transmission Electron Microscopy* ISBN: 978-0-387-76500-6 (Springer US, Boston, MA, 2009).

2. Porcar, L. *et al.* Structural investigation of PAMAM dendrimers in aqueous solutions using small-angle neutron scattering: Effect of generation. *Journal of Physical Chemistry B* **112,** 14772–14778. ISSN: 15206106 (Nov. 2008).

3. Greer, D. R. *et al.* Universal Relationship between Molecular Structure and Crystal Structure in Peptoid Polymers and Prevalence of the cis Backbone Conformation. *Journal of the American Chemical Society* **140,** 827–833. ISSN: 15205126 (Jan. 2018).

4. Zhu, L. *et al.* Initial-stage growth controlled crystal orientations in nanoconfined lamellae of a self-assembled crystalline-amorphous diblock copolymer. *Macromolecules* **34,** 1244–1251. ISSN: 00249297 (2001).

5. Mohanty, U., Ninhamt, B. W. & Oppenheim, I. Dressed polyions, counterion condensation, and adsorption excess in polyelectrolyte solutions. *Proc. Natl. Acad. Sci.* **93,** 4342–4344 (1996).

6. Tian, J. *et al.* High-resolution cryo-electron microscopy structure of block copolymer nanofibres with a crystalline core. *Nature Materials* **22,** 786–792. ISSN: 14764660 (June 2023).

7. Libera, M. R. & Egerton, R. F. Advances in the transmission electron microscopy of polymers. *Polymer Reviews* **50,** 321–339. ISSN: 15583724 (2010).

8. Kuei, B., Aplan, M. P., Litofsky, J. H. & Gomez, E. D. New opportunities in transmission electron microscopy of polymers. *Materials Science and Engineering R: Reports* **139,** 100516. ISSN: 0927796X. https://doi.org/10.1016/j.mser.2019.100516 (2020).

9. Cheng, Y. Single-particle Cryo-EM at crystallographic resolution. *Cell* **161,** 450–457. ISSN: 10974172. http://dx.doi.org/10.1016/j.cell.2015.03.049 (2015).

10. Jiang, X. *et al.* Imaging unstained synthetic polymer crystals and defects on atomic length scales using cryogenic electron microscopy. *Macromolecules* **51,** 7794–7799. ISSN: 15205835 (2018).

11. Lee, Z., Rose, H., Lehtinen, O., Biskupek, J. & Kaiser, U. Electron dose dependence of signal-to-noise ratio, atom contrast and resolution in transmission electron microscope images. *Ultramicroscopy* **145,** 3–12. ISSN: 18792723. `http://dx.doi.org/10.1016/j.ultramic.2014.01.010` (2014).

12. Russo, C. J. & Egerton, R. F. Damage in electron cryomicroscopy: Lessons from biology for materials science. *MRS Bulletin* **44,** 935–941. ISSN: 08837694 (2019).

13. Leijten, Z. J., Keizer, A. D., De With, G. & Friedrich, H. Quantitative Analysis of Electron Beam Damage in Organic Thin Films. *Journal of Physical Chemistry C* **121,** 10552–10561. ISSN: 19327455 (2017).

14. Egerton, R. F. Radiation damage to organic and inorganic specimens in the TEM. *Micron* **119,** 72–87. ISSN: 09684328. `https://doi.org/10.1016/j.micron.2019.01.005` (2019).

15. Cheng, Y., Grigorieff, N., Penczek, P. A. & Walz, T. A primer to single-particle cryo-electron microscopy. *Cell* **161,** 438–449. ISSN: 10974172. `http://dx.doi.org/10.1016/j.cell.2015.03.050` (2015).

16. Park, E., Campbell, E. B. & MacKinnon, R. Structure of a CLC chloride ion channel by cryo-electron microscopy. *Nature* **541,** 500–505. ISSN: 14764687 (2017).

17. Egerton, R. F. Control of radiation damage in the TEM. *Ultramicroscopy* **127,** 100–108. ISSN: 03043991. `http://dx.doi.org/10.1016/j.ultramic.2012.07.006` (2013).

18. Bock, L. V. & Grubmüller, H. Effects of cryo-EM cooling on structural ensembles. *Nature Communications* **13.** ISSN: 20411723 (Dec. 2022).

19. Milne, J. L. *et al.* Cryo-electron microscopy - A primer for the non-microscopist. *FEBS Journal* **280.** ISSN: 1742464X (2013).

20. Zheng, S. Q. *et al.* MotionCor2: Anisotropic correction of beam-induced motion for improved cryo-electron microscopy. *Nature Methods* **14,** 331–332. ISSN: 15487105. `http://dx.doi.org/10.1038/nmeth.4193` (2017).

21. Li, X. *et al.* Electron counting and beam-induced motion correction enable near-atomic-resolution single-particle cryo-EM. *Nature Methods* **10,** 584–590. ISSN: 15487091 (2013).

22. Punjani, A., Rubinstein, J. L., Fleet, D. J. & Brubaker, M. A. CryoSPARC: Algorithms for rapid unsupervised cryo-EM structure determination. *Nature Methods* **14,** 290–296. ISSN: 15487105 (Feb. 2017).

23. Wade, R. A brief look at imaging and contrast transfer. *Ultramicroscopy* **46,** 145–156 (1992).

24. Zhang, K. Gctf: Real-time CTF determination and correction. *Journal of Structural Biology* **193,** 1–12. ISSN: 10958657. `http://dx.doi.org/10.1016/j.jsb.2015.11.003` (2016).

25. Scheres, S. H. *Processing of Structurally Heterogeneous Cryo-EM Data in RELION* 1st ed., 125–157. `http://dx.doi.org/10.1016/bs.mie.2016.04.012` (Elsevier Inc., 2016).

26. Fernandez-Leiro, R. & Scheres, S. H. A pipeline approach to single-particle processing in RELION. *Acta Crystallographica Section D: Structural Biology* **73,** 496–502. ISSN: 20597983 (2017).

27. Jiang, X. *et al.* Effect of processing and end groups on the crystal structure of polypeptoids studied by cryogenic electron microscopy at atomic length scales. *Soft Matter* **15,** 4723–4736. ISSN: 17446848 (2019).

28. Sun, J. & Zuckermann, R. N. Peptoid polymers: A highly designable bioinspired material. *ACS Nano* **7,** 4715–4732. ISSN: 19360851 (2013).

29. Zhang, D., Lahasky, S. H., Guo, L., Lee, C. U. & Lavan, M. Polypeptoid materials: Current status and future perspectives. *Macromolecules* **45,** 5833–5841. ISSN: 00249297 (2012).

30. Kudirka, R. *et al.* Folding of a single-chain, information-rich polypeptoid sequence into a highly ordered nanosheet. *Biopolymers* **96,** 586–595. ISSN: 00063525 (2011).

31. Jiao, F. *et al.* Self-Repair and Patterning of 2D Membrane-Like Peptoid Materials. *Advanced Functional Materials* **26,** 8960–8967. ISSN: 16163028 (2016).

32. Battigelli, A. *et al.* Glycosylated Peptoid Nanosheets as a Multivalent Scaffold for Protein Recognition. *ACS Nano* **12,** 2455–2465. ISSN: 1936086X (2018).

33. Wang, M. *et al.* Peptoid-Based Programmable 2D Nanomaterial Sensor for Selective and Sensitive Detection of H2S in Live Cells. *ACS Applied Bio Materials* **3,** 6039–6048. ISSN: 25766422 (2020).

34. Yang, W. *et al.* Designing sequence-defined peptoids for fibrillar self-assembly and silicification. *Journal of Colloid and Interface Science* **634.** ISSN: 10957103 (2023).

35. Armand, M. Polymer solid electrolytes - an overview. *Solid State Ionics* **9-10,** 745–754. ISSN: 01672738 (Dec. 1983).

36. Hoffman, Z. J., Shah, D. B. & Balsara, N. P. Temperature and concentration dependence of the ionic transport properties of poly(ethylene oxide) electrolytes. *Solid State Ionics* **370,** 115751. ISSN: 0167-2738 (Nov. 2021).

37. Elmore, C. *et al.* Ion transport in solvent-free, crosslinked, single-ion conducting polymer electrolytes for post-lithium ion batteries. *Batteries* **4.** ISSN: 23130105 (2018).

38. Thelen, J. L. *et al.* Correlations between Salt-Induced Crystallization, Morphology, Segmental Dynamics, and Conductivity in Amorphous Block Copolymer Electrolytes. *Macromolecules* **51,** 1733–1740. ISSN: 15205835 (2018).

39. Maslyn, J. A. *et al.* Limiting Current in Nanostructured Block Copolymer Electrolytes. `https://doi.org/10.1021/acs.macromol.1c00425` (2021).

40. Maslyn, J. A., Frenck, L., Loo, W. S., Parkinson, D. Y. & Balsara, N. P. Extended cycling through rigid block copolymer electrolytes enabled by reducing impurities in lithium metal electrodes. *ACS Applied Energy Materials* **2,** 8197–8206. ISSN: 25740962 (2019).

41. Frenck, L., Maslyn, J. A., Loo, W. S., Parkinson, D. Y. & Balsara, N. P. Impact of Salt Concentration on Nonuniform Lithium Electrodeposition through Rigid Block Copolymer Electrolytes. *ACS Applied Materials and Interfaces* **11,** 47878–47885. ISSN: 19448252 (2019).

42. Galluzzo, M. D. *et al.* Measurement of Three Transport Coefficients and the Thermodynamic Factor in Block Copolymer Electrolytes with Different Morphologies. *Journal of Physical Chemistry B* **124,** 921–935. ISSN: 15205207 (2020).

43. Fang, C. *et al.* Ion Solvation Cage Structure in Polymer Electrolytes Determined by Combining X-ray Scattering and Simulations. *ACS Macro Letters* **12,** 1244–1250. ISSN: 2161-1653 (Sept. 2023).

44. Mukherjee, A., Tothadi, S. & Desiraju, G. R. Halogen bonds in crystal engineering: Like hydrogen bonds yet different. *Accounts of Chemical Research* **47,** 2514–2524. ISSN: 15204898 (2014).

45. Hassel, O. Structural aspects of interatomic charge-transfer bonding. *Science* **170,** 497–502. ISSN: 00368075 (1970).

46. Metrangolo, P., Neukirch, H., Pilati, T. & Resnati, G. Halogen bonding based recognition processes: A world parallel to hydrogen bonding. *Accounts of Chemical Research* **38,** 386–395. ISSN: 00014842 (2005).

47. Bishop, K. J., Wilmer, C. E., Soh, S. & Grzybowski, B. A. Nanoscale forces and their uses in self-assembly. *Small* **5,** 1600–1630. ISSN: 16136810 (2009).

48. Gilday, L. C. *et al.* Halogen Bonding in Supramolecular Chemistry. *Chemical Reviews* **115,** 7118–7195. ISSN: 15206890 (2015).

49. Cavallo, G. *et al.* The Halogen Bond. *Chemical Reviews* **116,** 2478–2601. ISSN: 15206890 (2016).

50. Mallada, B. *et al.* Real-space imaging of anisotropic charge of σ-hole by means of Kelvin probe force microscopy. *Science* **374,** 863–867. ISSN: 10959203 (2021).

51. Mukherjee, A. & Desiraju, G. R. Halogen bonds in some dihalogenated phenols: Applications to crystal engineering. *IUCrJ* **1,** 49–60. ISSN: 20522525 (2014).

52. Vaz, P. A., Rocha, J., Silva, A. M. & Guieu, S. Halogen-bonded dimers and ribbons from the self-assembly of 3-halobenzophenones. *CrystEngComm* **19,** 2202–2206. ISSN: 14668033 (2017).

53. Aakeröy, C. B., Sinha, A. S., Chopade, P. D. & Desper, J. Halogen bonding or close packing? Examining the structural landscape in a series of Cu(II)-acac complexes. *Dalton Transactions* **40,** 12160–12168. ISSN: 14779226 (2011).

54.   Xuan, S. & Zuckermann, R. N. Diblock copolypeptoids: A review of phase separation, crystallization, self-assembly and biological applications. *Journal of Materials Chemistry B* **8,** 5380–5394. ISSN: 20507518 (2020).

55.   Robertson, E. J. *et al.* Design, Synthesis, Assembly, and Engineering of Peptoid Nanosheets. *Accounts of Chemical Research* **49,** 379–389. ISSN: 15204898 (2016).

56.   Xuan, S. *et al.* Atomic-level engineering and imaging of polypeptoid crystal lattices. *Proceedings of the National Academy of Sciences of the United States of America* **116,** 22491–22499. ISSN: 10916490 (2019).

57.   Rendine, S., Pieraccini, S., Forni, A. & Sironi, M. Halogen bonding in ligand-receptor systems in the framework of classical force fields. *Physical Chemistry Chemical Physics* **13,** 19508–19516. ISSN: 14639076 (2011).

58.   Gutierrez, I. S. Parametrization of Halogen Bonds in the CHARMM General Force Field. *Biophysical Journal* **108,** 160a–161a (2015).

59.   Ibrahim, M. A. Molecular mechanical perspective on halogen bonding. *Journal of Molecular Modeling* **18,** 4625–4638. ISSN: 16102940 (2012).

60.   Ibrahim, M. A. A. Molecular Mechanical Study of Halogen Bonding in Drug Discovery. *Journal of Computational Chemistry* **32,** 2564–2574 (2011).

61.   Jorgensen, W. L. & Schyman, P. Treatment of halogen bonding in the OPLS-AA force field: Application to potent anti-HIV agents. *Journal of Chemical Theory and Computation* **8,** 3895–3901. ISSN: 15499618 (2012).

62.   Nunes, R., Vila-Viçosa, D., Machuqueiro, M. & Costa, P. J. Biomolecular Simulations of Halogen Bonds with a GROMOS Force Field. *Journal of Chemical Theory and Computation* **14,** 5383–5392. ISSN: 15499626 (2018).

63.   Gipson, B., Zeng, X., Zhang, Z. Y. & Stahlberg, H. 2dx-User-friendly image processing for 2D crystals. *Journal of Structural Biology* **157,** 64–72. ISSN: 10478477 (2007).

64.   Scheres, S. H. RELION: Implementation of a Bayesian approach to cryo-EM structure determination. *Journal of Structural Biology* **180,** 519–530. ISSN: 10478477. `http://dx.doi.org/10.1016/j.jsb.2012.09.006` (2012).

65.   Politzer, P., Murray, J. S. & Clark, T. Halogen bonding: An electrostatically-driven highly directional noncovalent interaction. *Physical Chemistry Chemical Physics* **12,** 7748–7757. ISSN: 14639076 (2010).

66.   Politzer, P., Murray, J. S. & Clark, T. Halogen bonding and other σ-hole interactions: A perspective. *Physical Chemistry Chemical Physics* **15,** 11178–11189. ISSN: 14639076 (2013).

67.   Cavallo, G., Metrangolo, P., Pilati, T., Resnati, G. & Terraneo, G. *Halogen Bond: A Long Overlooked Interaction* 628–635. ISBN: 9783319140568 (2015).

68. Parisini, E., Metrangolo, P., Pilati, T., Resnati, G. & Terraneo, G. Halogen bonding in halocarbon–protein complexes: A structural survey. *Chemical Society Reviews* **40,** 2267–2278. ISSN: 14604744 (2011).

69. Shields, Z. P., Murray, J. S. & Politzer, P. Directional Tendencies of Halogen and Hydrogen Bonds. *International Journal of Quantum Chemistry* **110,** 2823–2832 (2010).

70. Hammons, J. A. *et al.* Early-Stage Aggregation and Crystalline Interactions of Peptoid Nanomembranes. *Journal of Physical Chemistry Letters* **12,** 6126–6133. ISSN: 19487185 (2021).

71. Manning, G. S. Limiting Laws and Counterion Condensation in Polyelectrolyte Solutions I. Colligative Properties. *The Journal of Chemical Physics* **51,** 924–933. `https://doi.org/10.1063/1.1672157` (1969).

72. Muthukumar, M. *Physics of Charged Macromolecules: Synthetic and Biological Systems* (Cambridge University Press, 2023).

73. Marcus, Y. & Hefter, G. Ion pairing. *Chemical Reviews* **106,** 4585–4621. ISSN: 00092665 (Nov. 2006).

74. Anderson, C. F. & Record Jr., M. T. Salt-Nucleic Acid Interactions. *Annu. Rev. Phys. Chem* **46,** 657–700. `www.annualreviews.org` (1995).

75. Collins, K. D. The behavior of ions in water is controlled by their water affinity. *Quarterly reviews of biophysics* **52,** 1–19. ISSN: 14698994 (Nov. 2019).

76. Murthy, V. L. & Rose, G. D. Is counterion delocalization responsible for collapse in RNA folding? *Biochemistry* **39.** ISSN: 00062960 (2000).

77. Manning, G. S. & Ray, J. Counterion condensation revisited. *Journal of Biomolecular Structure and Dynamics* **16,** 461–476. ISSN: 15380254 (1998).

78. Manning, G. S. Limiting Laws and Counterion Condensation in Polyelectrolyte Solutions IV. The Approach to the Limit and the Extraordinary Stability of the Charge Fraction. *Biophysical Chemistry* **7,** 95–102 (1977).

79. Van der Maarel, J. *et al.* On the charge distribution in aqueous poly(styrenesulfonic acid) solutions. A small angle neutron scattering study. *Macromolecules* **26,** 7295–7299. `https://pubs.acs.org/sharingguidelines` (1993).

80. Böhme, U. & Scheler, U. Effective charge of poly(styrenesulfonate) and ionic strength - An electrophoresis NMR investigation. *Colloids and Surfaces A: Physicochemical and Engineering Aspects* **222,** 35–40. ISSN: 09277757 (July 2003).

81. Essafi, W., Lafuma, F. & Williams, C. Structural evidence of charge renormalization in semi-dilute solutions of highly charged polyelectrolytes. *European Physical Journal B* **9,** 261–266 (1999).

82. Van Der Vegt, N. F. *et al.* Water-Mediated Ion Pairing: Occurrence and Relevance. *Chemical Reviews* **116,** 7626–7641. ISSN: 15206890 (July 2016).

83. Yu, B., Pettitt, B. M. & Iwahara, J. Experimental Evidence of Solvent-Separated Ion Pairs as Metastable States in Electrostatic Interactions of Biological Macromolecules. *Journal of Physical Chemistry Letters* **10,** 7937–7941. ISSN: 19487185 (Dec. 2019).

84. Fraenkel, G. & Kim, J. P. Solvation of Anilinium Salts. *Journal of the American Chemical Society* **88,** 4203–4211 (1966).

85. Stanton, R. V., Hartsough, D. S. & Merz, K. M. Calculation of Solvation Free Energies Using a Density Functional/Molecular Dynamics Coupled Potential. *J. Phys. Chem* **97,** 11868–11870. https://pubs.acs.org/sharingguidelines (1993).

86. Buckner, J. K. & Jorgenson, W. L. Energetics and Hydration of the Constituent Ion Pairs of Tetramethylammonium Chloride. *J. Am. Chem. Soc.* **111,** 2507–2516. https://pubs.acs.org/sharingguidelines (1989).

87. Blaul, J., Wittemann, M., Ballauff, M. & Rehahn, M. Osmotic coefficient of a synthetic rodlike polyelectrolyte in salt-free solution as a test of the Poisson - Boltzmann cell model. *Journal of Physical Chemistry B* **104,** 7077–7081. ISSN: 15206106 (Aug. 2000).

88. Wandrey, C., Hunkeler, D., Wendler, U. & Jaeger, W. Counterion activity of highly charged strong polyelectrolytes. *Macromolecules* **33,** 7136–7143. ISSN: 00249297 (Sept. 2000).

89. Ballauff, M. & Jusufi, A. Anomalous small-angle X-ray scattering: Analyzing correlations and fluctuations in polyelectrolytes. *Colloid and Polymer Science* **284,** 1303–1311. ISSN: 0303402X (Aug. 2006).

90. Huber, K. & Scheler, U. New experiments for the quantification of counterion condensation. *Current Opinion in Colloid and Interface Science* **17,** 64–73. ISSN: 13590294 (Apr. 2012).

91. Böhme, U. & Scheler, U. *Counterion mobility and effective charge of polyelectrolytes in solution* in *Macromolecular Symposia* **211** (Apr. 2004), 87–92.

92. Paulino, C., Kalienkova, V., Lam, A. K., Neldner, Y. & Dutzler, R. Activation mechanism of the calcium-activated chloride channel TMEM16A revealed by cryo-EM. *Nature* **552,** 421–425. ISSN: 14764687 (Dec. 2017).

93. Ichael, M., Ckerman, J. A. & Lapham, E. C. Ion Channels — Basic Science and Clinical Disease. *New England Journal of Medicine* **336,** 1575–1586. ISSN: 0028-4793. https://www.nejm.org/doi/full/10.1056/nejm199705293362207 (May 1997).

94. Walter, J. D., Sawicka, M. & Dutzler, R. Cryo-EM structures and functional characterization of murine Slc26a9 reveal mechanism of uncoupled chloride transport. *eLife* **8.** ISSN: 2050-084X. https://elifesciences.org/articles/46986 (July 2019).

95. Deng, Z. *et al.* Cryo-EM structure of a proton-activated chloride channel TMEM206. *Science Advances* **7,** 5983–6007. ISSN: 23752548. https://www.science.org (Feb. 2021).

96. Dang, S. *et al.* Cryo-EM structures of the TMEM16A calcium-activated chloride channel. *Nature* **552,** 426–429 (2017).

97. Chan, B. A. *et al.* Polypeptoid polymers: Synthesis, characterization, and properties. *Biopolymers* **109,** 1–25. ISSN: 10970282 (2018).

98. Wei, T., Jung, J. H. & Scott, T. F. Dynamic Covalent Assembly of Peptoid-Based Ladder Oligomers by Vernier Templating. *Journal of the American Chemical Society* **137,** 16196–16202. ISSN: 15205126 (Dec. 2015).

99. Yu, T. *et al.* Structural Elucidation of a Polypeptoid Chain in a Crystalline Lattice Reveals Key Morphology-Directing Role of the N-Terminus. *ACS Nano* **17,** 4958–4970. ISSN: 1936086X (Mar. 2023).

100. Seidler, M. *et al.* Importance of the Positively Charged σ-Hole in Crystal Engineering of Halogenated Polypeptoids. *The Journal of Physical Chemistry B* **126,** 4152–4159. ISSN: 1520-6106 (June 2022).

101. Gross, K. C. & Seybold, P. G. Substituent effects on the physical properties and pKa of aniline. *International Journal of Quantum Chemistry* **80,** 1107–1115. ISSN: 00207608 (2000).

102. Druchok, M., Malikova, N., Rollet, A. L. & Vlachy, V. Counter-ion binding and mobility in the presence of hydrophobic polyions - Combining molecular dynamics simulations and NMR. *AIP Advances* **6.** ISSN: 21583226 (June 2016).

103. Ruggeri, F. *et al.* Single-molecule electrometry. *Nature Nanotechnology* **12,** 488–495. ISSN: 17483395 (May 2017).

104. O'Shaughnessy, B. & Yang, Q. Manning-Oosawa counterion condensation. *Physical Review Letters* **94.** ISSN: 00319007 (Feb. 2005).

105. Heyda, J. & Dzubiella, J. Ion-specific counterion condensation on charged peptides: Poisson-Boltzmann. *Soft Matter* **8,** 9338–9344. www.rsc.org/softmatter (2012).

106. Skitchenko, R. K., Usoltsev, D., Uspenskaya, M., Kajava, A. V. & Guskov, A. Census of halide-binding sites in protein structures. *Bioinformatics* **36,** 3064–3071. ISSN: 14602059 (May 2020).

107. Bankura, A. *et al.* A systematic study of chloride ion solvation in water using van der Waals inclusive hybrid density functional theory. *Molecular Physics* **113,** 2842–2854. ISSN: 13623028. https://www.tandfonline.com/action/journalInformation?journalCode=tmph20 (Sept. 2015).

108. Heuft, J. M. & Meijer, E. J. Density functional theory based molecular-dynamics study of aqueous iodide solvation. *Journal of Chemical Physics* **123.** ISSN: 00219606 (Sept. 2005).

109. Jiang, X. *et al.* Atomic-Scale Corrugations in Crystalline Polypeptoid Nanosheets Revealed by Three-Dimensional Cryogenic Electron Microscopy. *ACS Macro Letters* **12,** 632–638. ISSN: 2161-1653 (May 2023).

110. Ooe, K. *et al.* Direct imaging of local atomic structures in zeolite using optimum bright-field scanning transmission electron microscopy. *Science Advances* **9.** ISSN: 23752548 (Aug. 2023).

111. Manning, G. S. Counterion condensation on charged spheres, cylinders, and planes. *Journal of Physical Chemistry B* **111,** 8554–8559. ISSN: 15206106. `https://pubs.acs.org/sharingguidelines` (July 2007).

112. Böhme, U., Klenge, A., Hänel, B. & Scheler, U. Counterion condensation and effective charge of PAMAM dendrimers. *Polymers* **3,** 812–819. ISSN: 20734360 (June 2011).

113. Xia, J., Dubin, P. L. & Havel1, H. A. Electrophoretic Light Scattering Study of Counterion Condensation on Polylysine. *Macromolecules* **26,** 6335–6337. `https://pubs.acs.org/sharingguidelines` (1993).

114. Stevens, M. J. Bundle Binding in Polyelectrolyte Solutions. *Physical Review Letters* **82,** 101–104 (1999).

115. Van Rijt, M. M. *et al.* Designing stable, hierarchical peptide fibers from block co-polypeptide sequences. *Chemical Science* **10,** 9001–9008. ISSN: 20416539 (2019).

116. Ogata, A. F. *et al.* Direct Observation of Amorphous Precursor Phases in the Nucleation of Protein-Metal-Organic Frameworks. *Journal of the American Chemical Society* **142,** 1433–1442. ISSN: 15205126 (2020).

117. Cai, X. *et al.* Sequence-Defined Nanotubes Assembled from IR780-Conjugated Peptoids for Chemophototherapy of Malignant Glioma. *Research* **2021,** 1–12. ISSN: 26395274 (2021).

118. Jin, H. *et al.* Highly stable and self-repairing membrane-mimetic 2D nanomaterials assembled from lipid-like peptoids. *Nature Communications* **7,** 1–8. ISSN: 20411723 (2016).

119. Yeo, R. S. Ion Clustering and Proton Transport in Nafion Membranes and Its Applications as Solid Polymer Electrolyte. *Journal of the Electrochemical Society* **130,** 533–538 (1983).

120. Christie, A. M., Lilley, S. J., Staunton, E., Andreev, Y. G. & Bruce, P. G. Increasing the conductivity of crystalline polymer electrolytes. *Nature* **433,** 50–53. ISSN: 00280836 (Jan. 2005).

121. Gadjourova, Z., Andreev, Y. G., Tunstall, D. P. & Bruce, P. G. Ionic conductivity in crystalline polymer electrolytes. *Nature* **412,** 520–523. ISSN: 00280836 (2001).

122. Cheng, S., Li, X., Zheng, Y., Smith, D. M. & Li, C. Y. Anisotropic ion transport in 2D polymer single crystal-based solid polymer electrolytes. *Giant* **2,** 100021. ISSN: 26665425 (2020).

123. Frenck, L. *et al.* Effect of salt concentration profiles on protrusion growth in lithium-polymer-lithium cells. *Solid State Ionics* **358,** 115517. ISSN: 01672738. `https://doi.org/10.1016/j.ssi.2020.115517` (2020).

124. Fang, C., Mistry, A., Srinivasan, V., Balsara, N. P. & Wang, R. Elucidating the Molecular Origins of the Transference Number in Battery Electrolytes Using Computer Simulations. *JACS Au* **3,** 306–315. ISSN: 2691-3704 (Feb. 2023).

125. Mistry, A. *et al.* Toward Bottom-Up Understanding of Transport in Concentrated Battery Electrolytes. *ACS Central Science* **8,** 880–890. ISSN: 2374-7943 (July 2022).

126. Shah, N. J. *et al.* Nanosecond solvation dynamics in a polymer electrolyte for lithium batteries. *Nature Materials* **23,** 664–669. ISSN: 1476-1122 (May 2024).

127. Lotz, B., Kovacs, A. J., Bassett, G. A. & Keller, A. Properties of copolymers composed of one poly-ethylene-oxide and one polystyrene block - II. Morphology of single crystals. *Kolloid-Zeitschrift & Zeitschrift für Polymere* **209,** 115–128. ISSN: 0303402X (1966).

128. Chen, W. Y. *et al.* "Chemically shielded" poly(ethylene oxide) single crystal growth and construction of channel-wire arrays with chemical and geometric recognitions on a submicrometer scale. *Macromolecules* **37,** 5292–5299. ISSN: 00249297 (2004).

129. Hsiao, M. S. *et al.* Crystal orientation change and its origin in one-dimensional nanoconfinement constructed by polystyrene-block-poly(ethylene oxide) single crystal mats. *Macromolecules* **41,** 8114–8123. ISSN: 00249297 (Nov. 2008).

130. Huang, P. *et al.* Confinement size effect on crystal orientation changes of poly(ethylene oxide) blocks in poly(ethylene oxide)-b-polystyrene diblock copolymers. *Macromolecules* **37,** 3689–3698. ISSN: 00249297 (May 2004).

131. Loo, W. S. *et al.* Phase Behavior of Mixtures of Block Copolymers and a Lithium Salt. *Journal of Physical Chemistry B* **122,** 8065–8074. ISSN: 15205207 (2018).

132. Verbeeck, J., Schattschneider, P. & Rosenauer, A. Image simulation of high resolution energy filtered TEM images. *Ultramicroscopy* **109,** 350–360. ISSN: 03043991 (Mar. 2009).

133. Takahashi, Y. & Tadokoro, H. Structural Studies of Polyethers, $(-(CH_2)m-O-)n$. X. Crystal Structure of Poly(ethylene oxide). *Macromolecules* **6,** 672–675. ISSN: 15205835 (1973).

134. Andreev, Y. G., Lightfoot, P. & Bruce, P. G. A General Monte Carlo Approach to Structure Solution from Powder-Diffraction Data: Application to Poly(ethylene oxide)3:LiN(SO2CF3)2. *Journal of Applied Crystallography* **30,** 294–305. ISSN: 00218898 (June 1997).

135. Madsen, J. & Susi, T. abTEM: ab Initio Transmission Electron Microscopy Image Simulation. *Microscopy and Microanalysis* **26,** 448–450. ISSN: 1431-9276 (Aug. 2020).

136. Ophus, C. Four-Dimensional Scanning Transmission Electron Microscopy (4D-STEM): From Scanning Nanodiffraction to Ptychography and Beyond. *Microscopy and Microanalysis* **25,** 563–582. ISSN: 1431-9276 (2019).

137. Chen, Z. *et al.* Electron Ptychography Achieves Atomic-Resolution Limits Set By Lattice Vibrations. *Science* **372,** 826–831 (2021).

138. Chen, Z. *et al.* Mixed-state electron ptychography enables sub-angstrom resolution imaging with picometer precision at low dose. *Nature Communications* **11,** 1–10. ISSN: 20411723. http://dx.doi.org/10.1038/s41467-020-16688-6 (2020).

139. Zhou, L. *et al.* Low-dose phase retrieval of biological specimens using cryo-electron ptychography. *Nature Communications* **11,** 1–9. ISSN: 20411723. http://dx.doi.org/10.1038/s41467-020-16391-6 (2020).

140. Pelz, P. M., Qiu, W. X., Bücker, R., Kassier, G. & Miller, R. J. Low-dose cryo electron ptychography via non-convex Bayesian optimization. *Scientific Reports* **7,** 1–13. ISSN: 20452322 (2017).

141. McGilvery, C. M., Goode, A. E., Shaffer, M. S. & McComb, D. W. Contamination of holey/lacey carbon films in STEM. *Micron* **43,** 450–455. ISSN: 09684328 (Feb. 2012).

142. Stoeva, Z., Martin-Litas, I., Staunton, E., Andreev, Y. G. & Bruce, P. G. Ionic conductivity in the crystalline polymer electrolytes PEO6:LiXF6, X = P, As, Sb. *Journal of the American Chemical Society* **125,** 4619–4626. ISSN: 00027863 (2003).

143. Frech, R., Chintapalli, S., Bruce, P. G. & Vincent, C. A. Structure of an amorphous polymer electrolyte, poly(ethylene oxide) 3 : LiCF 3 SO 3. *Chem. Commun,* 157–158 (1997).